Diss. ETH No. 14262

Locating Implants with respect to the Bone in Diagnostic X-ray Images of the Pelvis

A dissertation submitted to the
SWISS FEDERAL INSTITUTE OF TECHNOLOGY
for the degree of
Doctor of Technical Sciences

presented by
Kathrin Valentine Burckhardt
Diploma in Physics, Ludwig-Maximilians-Universität, Munich
born on August 13, 1969
citizen of Germany

accepted on the recommendation of
Professor Gábor Székely, examiner
Professor Leo Joskowicz, co-examiner
Professor Jürg Hodler, co-examiner

June 2001

Acknowledgements

Abstract

This thesis is about the assessment of the migration of artificial hip sockets in clinical x-ray images. "Migration" means the displacement of the bony implant with respect to the bone in time. It is seen as the most objective indicator for an implant loosening, which is the main problem in hip replacement. The data source are the standard anterior-posterior pelvic radiographs which are usually acquired for the post-operative examination of the replacement. According to the general case, it is assumed that no computer tomograms of the pelvis are available. Due to the lack of 3D information of the bone, only the components of the migration parallel to the plane of the radiographic film can be observed.

It is assumed that a migration of only 0.5 to 1.0 millimeter in the first two postoperative years implies an increased risk of later loosening. This correlation is especially important if a new type of cup or implantation technique is introduced. It means that a precise assessment of migration allows for an early judgement of the fixation properties and for the prevention of the use of implants with a high tendency to loose in many patients. Hence, a useful method for measuring migration should allow for the observation of implant displacements in the sub-millimeter range. The precision of the previously proposed methods for cup migration assessment was analysed theoretically considering the errors entering the measurement. Standard deviations in the range of 0.6 mm to 3.0 mm resulted. Based on the theoretical analysis, a computerized system for a more precise assessment of the migration was designed. In this system, which is named XIMIT, the sensitivity of the measurement towards the variable position and orientation of the pelvis at exposure is minimized. The most relevant of the remaining sources of error is the uncertainty in determining the position of the necessary bony landmarks and of the implant in the image. It is reduced by the use of image analysis tools.

The precise localization of the bony landmarks is achieved by applying a state-of-the-art template matching algorithm. The user roughly determines the position of a landmark in all images of a pelvis and chooses the template, i.e. a region of interest containing the respective bony feature in the first post-operative radiograph. The algorithm finds the exact landmark coordinates in the later radiographs by geometrically fitting the bony structures in these images to the template. The implant is located based on the principle of Analysis-by-Synthesis. Using the CAD model of the artificial hip socket, a synthetic radiograph of the cup depending on its approximate 3D position and orientation in the x-ray system is generated. The exact 3D parameters are recovered by matching the synthetic image to the original one while virtually translating and rotating the cup.

For testing the system, series of x-ray images of a validation unit bearing a bony pelvis phantom were acquired. During the acquisition, the pelvis was tilted and translated, and a migration was simulated. The performance in locating the bony landmarks proved to be strongly dependent on the shape of the matched anatomical structure. The principle of Analysis-by-Synthesis was found to allow for a reliable localization of the cup. The experimental and theoretical error estimation demonstrated that XIMIT allows for a determination of the cup migration with the targeted standard deviation in the sub-millimeter range. The conditions for this precision are that an extreme orientation of the pelvis at exposure is avoided, and that the anatomical structure used as bone reference can be clearly identified in the x-ray image.

Zusammenfassung

In dieser Arbeit geht es um die Bestimmung der Migration von künstlichen Hüftpfannen unter Verwendung von klinischen Röntgenaufnahmen. "Migration" bezeichnet die zeitliche Verschiebung eines Implantats relativ zum Knochen. Sie wird als der objektivste Indikator einer Implantat-Lockerung, das Hauptproblem bei künstlichen Gelenken, betrachtet. Als Datenquelle dienen die anterior-posterior Röntgenbilder des Beckens, die üblicherweise zur Nachuntersuchung der Implantation angefertigt werden. Es wird dabei vom allgemeinen Fall ausgegangen, dass kein Computertomogramm vom Beckenbereich zur Verfügung steht. In Ermangelung von 3D-Daten des Beckenknochens können nur die Migrationskomponenten parallel zur Ebene des Röntgenfilms beobachtet werden.

Es wird angenommen, dass eine Migration von nur 0.5 bis 1.0 Millimeter in den ersten zwei Jahren nach der Implantation auf ein erhöhtes Risiko späterer Lockerung schliessen lässt. Dieser Zusammenhang ist besonders wichtig, wenn ein neuer Pfannen-Typ oder eine neue Implantationstechnik eingeführt wird. Mittels einer genauen Migrationsmessung ist demnach eine frühe Beurteilung der Fixierungseigenschaften möglich, und die Verwendung von Implantaten mit hoher Tendenz zur Lockerung bei vielen Patienten kann verhindert werden. Deshalb sollten mit einer nützlichen Migrationmessungs-Methode Verschiebungen des Implantats im Sub-Millimeter-Bereich beobachtet werden können. Die Genauigkeit der bestehenden Methoden zur Migrationsbestimmung wurde unter Berücksichtigung der Fehler, die in die Messung eingehen, analysiert. Es resultierten Standardabweichungen im Bereich von 0.6 mm bis 3.0 mm. Basierend auf der theoretischen Analyse wurde ein rechnergestütztes System zur genaueren Beobachtung der Pfannenverschiebung entwickelt. Bei diesem System genannt XIMIT ist die Sensibilität der Messung gegenüber der variablen Position und Orientierung des Beckens bei der Aufnahme minimiert. Die Ungenauigkeit der Lokalisierung der benötigten Knochenpunkte und der Pfanne im Bild, die die relevanteste der restlichen Fehlerquellen darstellt, wird durch die Verwendung von Bildanalysetechniken reduziert.

Die genaue Lokalisierung der Knochenpunkte wird durch die Anwendung eines Template-Matching-Verfahrens erreicht. Der Benützer gibt die ungefähre Position eines Punktes in allen Aufnahmen eines Beckens vor und bestimmt das Template, d.h. die Bildregion im ersten post-operativen Röntgenbild, die das jeweilige Knochen-Merkmal enthält. Die genauen Punktkoordinaten in den späteren Aufnahmen werden von dem Verfahren mittels der geometrischen Anpassung der Knochenstrukturen in diesen Bildern an das Template bestimmt. Das Implantat wird mit Hilfe des Prinzips "Analyse-durch-Synthese" lokalisiert.

Unter Verwendung des CAD-Modells wird ein synthetisches Röntgenbild der Pfanne in Abhängigkeit ihrer Position und Orientierung im Röntgensystem generiert. Die genauen 3D-Parameter werden dadurch bestimmt, dass die Pfanne solange virtuell im Röntgensystem verschoben und gedreht wird, bis ihre synthetisierte Abbildung mit der im Originalbild übereinstimmt.

Um das entwickelte System zu testen, wurden Röntgenbild-Serien einer Validierungseinheit mit Beckenknochen und Pfanne angefertigt. Während der Aufnahme der Serien wurde sowohl das Becken gekippt und verschoben als auch eine Migration der Pfanne simuliert. Es konnte beobachtet werden, dass die Eignung des Matching-Algorithmus zur Lokalisierung der Knochenpunkte stark von der Form der verwendeten anatomischen Struktur abhängt. Analyse-durch-Synthese erwies sich als geeignetes Prinzip für die zuverlässige Lokalisierung der Pfanne. Die experimentelle und theoretische Abschätzung des Gesamtfehlers zeigte, dass XIMIT eine Bestimmung der Pfannenverschiebung mit der angestrebten Sub-Millimeter-Genauigkeit ermöglicht. Die Bedingungen dabei sind, dass eine extreme Orientierung des Beckens bei der Röntgenaufnahme vermieden wird, und dass die anatomische Struktur, die als Knochenreferenz verwendet wird, im Röntgenbild klar erkennbar ist.

Contents

1

Introduction

Today, various refined techniques are available for acquiring diagnostic images of the body: computer tomography, magnetic resonance imaging, ultrasound scanning, endoscopy, scintigraphy, etc. Still, most of the medical images are radiographs. Radiography is cost-efficient, because it is hardly time-consuming and it requires a relatively simple machinery. In addition to this it makes an outstanding spatial and intensity resolution possible, an advantage that is sometimes overlooked.

One field where x-ray images are particularly relevant is arthroplasty, a branch of orthopaedics concerned with the surgical substitution of malformed or degenerated joints. They are extensively used especially in total hip replacement (THR), which is the most widespread and most successful orthopaedic intervention. Worldwide, more than half a million people per year suffering from arthrosis get their hip replaced by an endoprosthesis. In most of the THR's, the preoperative planning as well as the postoperative follow-up examination are based on x-ray images. Computer tomographs usually are avoided because they are expensive and imply a high radiation exposure for the patient.

A main concern of the follow-up studies is the detection of a loosening of the cup (the artificial hip socket). The fixation of the cup in the bone depends on various factors, such as the material and shape of the endoprosthesis, or the surgical technique which includes, for example, the use of screws or of bone cement. It is important for the individual patient to promptly and reliably diagnose the loosening, because it can lead to a destruction of the bone cavity holding the implant and evokes pain which has to be relieved by an exchange of the cup. Moreover, the assessment of the fixation is also relevant for a systematic clinical evaluation of specific kinds of cups or implantation techniques. Besides clinical symptoms such as pain, a number of radiographic signs have been reported for the detection of loosening: radiolucent zones at the cement-bone or at the implant-bone interface, radiolucency around the screws, fracture of cement, cortical hypertrophy, etc. [Manaster 1996, Johnston *et al.* 1990, DeLee and Charnley 1976]. They become detectable with the naked eye in advanced stages of loosening only, mostly several years after surgery, and their interpretation is highly observer dependent.

A more objective indicator for the implant fixation is supposed to be the migration, i.e. the displacement of the implant relative to the bone in time. Based on the observation that implants which become instable migrate, it was proposed that loosening should be defined as migration [Mjöberg *et al.* 1985]. This definition has been adopted by seve-

1

ral authors who have judged the fixation properties of a type of cup or an implantation technique by observing the migration [Sutherland *et al.* 1982, Bruijn *et al.* 1995, Mjöberg *et al.* 1986, Stöckl *et al.* 1999]. However, a displacement does not strictly imply the loosening of the implant. Cups can migrate in the first months after implantation before they stabilize [Mjöberg *et al.* 1986, Kärrholm *et al.* 1997, Nilsson and Kärrholm 1996]. Still, a displacement exceeding 0.5–1 mm during the first two postoperative years indicates an increased risk of failure according to [Kärrholm *et al.* 1997, Krismer *et al.* 1996b]. This finding is clinically important, especially when a new type of cup or implantation technique is introduced. If a high tendency of a kind of THR to loose can be detected at an early stage, its use in many patients could be prevented. However, early postoperative examinations require a method for measuring displacements of the cup in the sub-millimeter range. A method with this precision is also necessary for a further investigation of the correlation between loosening and migration. Standard radiographs represent a suitable data source for precise measurements because of their mentioned high resolution. Unfortunately, they have the big drawback of providing only 2D information.

Various more or less refined methods have been proposed for quantifying migration using x-ray images. In one of them the problem of the missing third dimension is overcome by applying a stereo x-ray technique. In the so-called Roentgen Stereophotogrammetic Analysis (RSA) first proposed by [Selvik 1974], two x-ray images are taken from different directions. Additionally, an exposure of a cage for calibrating the radiographic set-up is made. The 3D positions of tantalum balls implanted as markers in the bone and in the cup are determined by ray intersection. RSA is generally accepted for its high precision. The standard deviation is reported to be 0.1 mm for the x-y-components and 0.23 mm for the z-component of the migration [Kärrholm *et al.* 1997, Mjöberg *et al.* 1986, Snorrason and Kärrholm 1990]. However, RSA is "a research tool" [Nilsson and Kärrholm 1996] and not qualified for wide range examinations. The necessary implantation of up to nine markers in the bone and seven in the implant as well as the time-consuming exposure technique prevent its integration in the daily clinical routine.

The other proposals for assessing the migration are based on measuring the position of the cup relative to the bone in the images of the routinely made radiographic follow-up series. This implies that, with one exception, they all allow only for an observation of the implant displacement parallel to the x-ray film. They are here classified into "simple" and "complex" methods. The simple methods are characterized by the use of basic geometry and by the determination of image points in the x-ray film using a pencil or in the digital radiograph by mouse-clicking. The complex ones additionally involve higher level software, image analysis techniques, more complicated geometrical computations, or 3D data of the cup or the pelvis.

In most of the simple methods, the bone reference is defined by the so-called teardrop figures [Nunn *et al.* 1989, Dickob *et al.* 1994, Sutherland *et al.* 1982, Collet *et al.* 1985, Massin *et al.* 1989, Brand *et al.* 1986]. These figures are symmetrical bony structures close to the implant and are shown in Fig. 1.1. Some authors have recommended the use of other anatomical structures such as the ischial tuberosities forming in the x-ray image the lower edge of the pelvis [Manaster 1996], or the almost vertical Köhler line lying
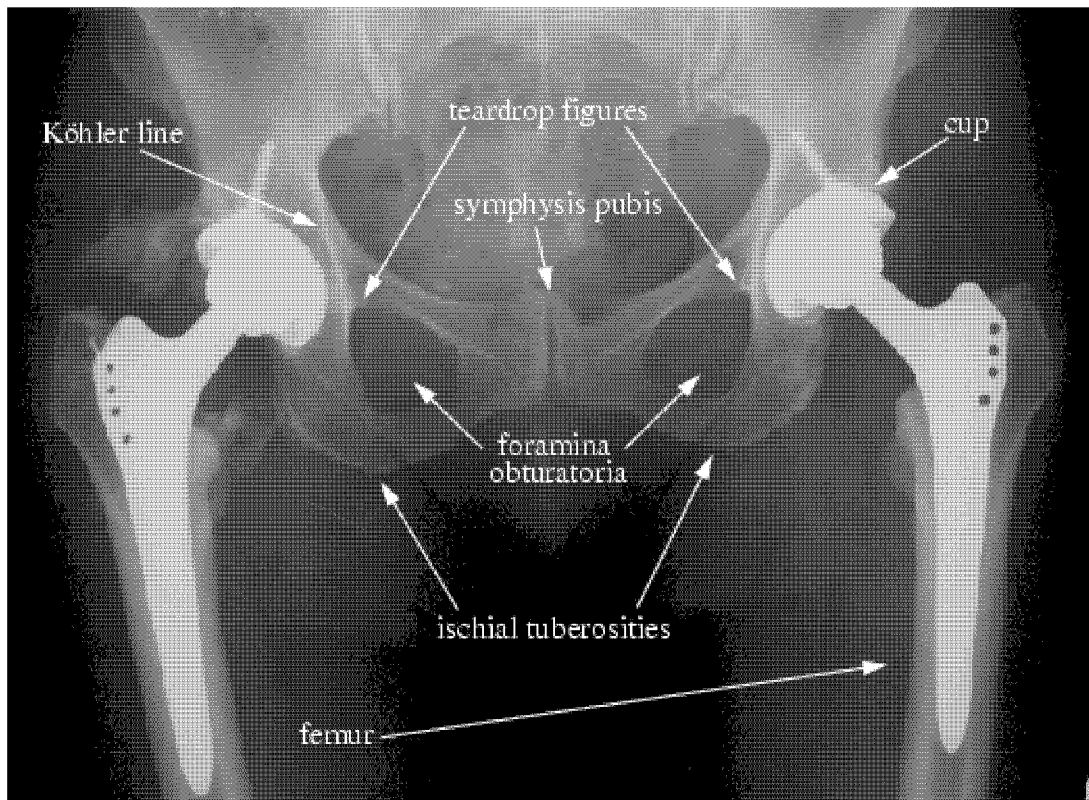
Figure 1.1: *The pelvis radiograph with typical bony reference points.*

medial to the joint [Sutherland *et al.* 1982, Massin *et al.* 1989]. As cup reference point serves the center of the cup's opening plane [Sutherland *et al.* 1982, Dickob *et al.* 1994, Massin *et al.* 1989, Brand *et al.* 1986], the upper or the medial contour of the cup [Collet *et al.* 1985, Massin *et al.* 1989, Manaster 1996], or even the center of the femoral head [Nunn *et al.* 1989]. In the radiographs, a line is drawn connecting the teardrop figures or the ischial tuberosities using a pencil. In case of digital images, evaluated e.g. in [Dickob *et al.* 1994], this line is defined by mouse-clicking on the respective bony structures. The vertical migration is determined by measuring the distance between the line and the cup point using a ruler. For the horizontal displacement, the distance of the cup point to the ipsilateral teardrop figure along this line or, in [Sutherland *et al.* 1982] and [Massin *et al.* 1989], the distance to the Köhler line is determined. The measured cup–bone distances are afterwards mostly corrected for magnification using the known diameter of the cup or of the femoral head and the one in the x-ray image. In [Nunn *et al.* 1989, Dickob *et al.* 1994], an additional correction of the horizontal distance at a changed pelvis orientation is proposed.

The definitions described above of the cup–bone distance have been adopted in some of the complex methods. In the hip evaluation system presented in [Cianci *et al.* 1995], for example, the vertical position of the cup is again represented with respect to the line connecting the teardrop figures and the horizontal one with respect to the Köhler line.

The reference points in the radiographic film are digitized using a graphic tablet. Despite the computerized evaluation the precision of this system is limited because the reference points are still located by the user. The teardrop figure is used as landmark for the vertical displacement also in [Hardinge *et al.* 1991], where a combination of the approaches of migration assessment described in two preceding publications [Brand *et al.* 1986, Jones *et al.* 1989] is proposed. For the horizontal migration another bone reference, the midline of the symphysis pubis, has been chosen. In this approach, the user dependency is reduced by a semi-automated localization of this pubic line and the cup. The pubic line is determined automatically using the graylevel profiles of the left and right edge of the symphysis pubis, after the user has marked its upper and its lower end. As polyethylen implants are evaluated the only visible feature of the artificial socket in the radiograph is a wire on the cup's external surface. The center of the socket is found by using the graylevel profiles of the wire. A fully user-independent approach has been presented in [Redhead *et al.* 1997, Redhead 1997]. The lower ipsilateral part of the pelvis bone, the femur, the femoral prosthesis, and the cup are located in the x-ray image using active shape models for the identification of the object's contours. Although the main goal has been to assess the sinking of the femoral component within the bone, the latter method could also be applied to cup migration measurement. However, the objects identified have a great extension in 3D, which has the consequence that their image contours strongly alter at a change of the pelvis orientation and position at exposure. This would be advantageous for the analysis of the correlation between movement and image shape of the pelvis, but it is a drawback for the precise assessment of the cup–bone distance because of the resulting instability of the pelvic bone reference.

In some of the complex methods also the third dimension is involved. In EBRA (the acronym of Ein-Bild-Röntgen-Analyse, which means single image analysis), the film–focus constellation at exposure is estimated [Krismer *et al.* 1995]. Planes are constructed connecting the focus with bone reference lines in the x-ray image. The latter are user-defined tangents to the foramina obturatoria, which are symmetrical holes in the lower pelvic bone. The horizontal and vertical migration is assessed by observing – only in radiographs with similar pelvis orientation – the distances between the planes and the 3D cup center reconstructed using the known size of the femoral head. A complete semi-automated 3D analysis is achieved in the approach proposed in [LaRose *et al.* 2000] by recovering the position and orientation of the cup as well as of the pelvis at exposure. The 3D parameters of the artificial hip socket are gained by means of a contour image of the cup generated using its CAD model. The parameters are estimated by fitting the implant's synthetic contour to its real one in the radiograph. The position and orientation of the pelvis is found by directly minimizing the difference between the bone's original radiographic projection and an x-ray image synthesized using the preoperative pelvic CT volume.

This last method may be the best approach for measuring the cup displacement using single pelvis x-ray images. It even makes the assessment of the rotation between cup and bone possible. However, it is only useful in the rather rare cases where CT's are acquired. None of the other methods represent an optimal solution for assessing the relative cup position in the sub-millimeter range. The majority of them is based on the use of pencil

and ruler or on mouse-clicking in digital radiographs and hence lacks of a user independent and precise localization of the cup and of the bony references. What is additionally missing is a reasonable consideration of the projective nature of the radiographic imaging system. Being aware of the problem of the variable object orientation in the x-ray unit, several authors have studied the individual effect of pelvis tilt with respect to the vertical or the horizontal axis on the bone–cup distance. However, none of the approaches is based on a complete analysis of the overall influence of all variables of the imaging system.

The initial question of this work was if the radiographic imaging system principally allows for sub-millimeter position measurements of the artificial hip socket. The condition has been that no CT data are available, this means that the exact 3D shape of the pelvis is unknown. While investigating this question a new useable method has arisen for assessing cup migration using the radiographs of the THR's follow-up study. Despite a generic approach, it has been necessary to focus on one certain type of implant, which is an uncemented cup with a polyethylen liner and a titanium shell. The problem has been approached from two different sides: first, the geometrical analysis and optimization of the previous methods, and second the improvement in defining the bone reference and in locating the implant in the radiograph. The former has been realized as described in the Chapters 2 and 3, by formulating the observed bone–implant distance as an analytical function depending on the variable imaging parameters. Through the application of the principle of error propagation to this function the variance of the distance could be estimated and reduced by appropriately choosing its geometrical definition. The latter has been pursued by using image analysis techniques. As described in Chapter 4, an existing template matching algorithm has been applied to anatomical radiographic structures in order to precisely define the bone reference. An automated determination of the cup position, which is presented in Chapter 5, has been achieved by the use of the principle of Analysis-by-Synthesis: The artificial socket is virtually rotated and translated in the x-ray system, until the difference between the original x-ray projection of the cup and the one synthesized using its CAD model is minimal. The developed method for assessing the cup migration was validated experimentally as described in Chapter 6 based on X-ray images of a pelvic phantom. These images were acquired under simulation of the cup migration and of the variable orientation and position of the pelvis in the x-ray system. The theoretical and the experimental error of the migration measurement were determined and its performance on real clinical radiographs was tested, which yielded the results presented in Chapter 7.

2

Error analysis of previous methods of migration assessment

Several studies were published concerning the precision in the assessment of cup migration using standard radiographs. In the majority of them, the error was estimated through phantom experiments. The cup position with respect to the bone was observed varying the orientation of the pelvis with respect to the medio-lateral and the cranio-caudal axis [Dickob *et al.* 1994, Wetherell *et al.* 1989, Sutherland and Bresina 1992, Ilchmann *et al.* 1997]. The variable pelvis position relative to the focus was not considered. Although the experimental conditions were similar in these studies, the reported results strongly differ. For example, for the method proposed by [Nunn *et al.* 1989] using conventional x-ray images, [Ilchmann *et al.* 1997] found a standard deviation of the cup's y-position of 3.5 mm at a rotation of the pelvis around the cranio-caudal axis in the range of $\pm 10°$. Testing this method using x-ray films as well as digitized radiographs, [Dickob *et al.* 1994] estimated this error, however, to lie between 0.1 mm and 1.1 mm without observing a difference between manual and digital evaluation.

Another way of empirically estimating the error of migration assessment was chosen in [Malchau *et al.* 1995, Ilchmann *et al.* 1992a, Ilchmann *et al.* 1992b]. The results of applying different methods have been compared with the ground truth assumed to be given by RSA [Selvik 1990], which is the most precise measurement tool according to the general opinion. Also using this approach, the reported errors change from author to author. Examining again the method of [Nunn *et al.* 1989], the accuracy, defined as mean deviation from ground truth plus two standard deviations, was determined in [Malchau *et al.* 1995] to be 6.5 mm for the medio-lateral and 6.3 mm for the cranio-caudal migration of one of the three types of cup investigated. However, in [Ilchmann *et al.* 1992b] the corresponding values are 2.0 mm and 2.2 mm. The conditions in these two studies slightly differ, because the cup models are probably different and the correction for magnification is omitted in the former and considered in the latter. Nevertheless, this can hardly explain the great variation. The reason for the great errors in [Malchau *et al.* 1995] could be the deviation of the bony reference system in the image, which defines the direction of the migration measured in the radiograph, from the three-dimensional coordinate system where the ground truth is represented in.

The contradictory results indicate that an empirical estimation of the error in assessing the cup displacement is generally problematic. Using experimental radiographs where the clinical conditions are imitated depends on the pelvic phantom, and the simulation of all errors simultaneously entering the measurement is not possible. Using real data requires the ground truth which is difficult to obtain. Moreover, in both cases a great amount of data is necessary and the investigator has an influence which can hardly be eleminated.

In order to improve the analysis of the various methods, a scheme was developed for estimating their precision more objectively. The precision is defined by the standard deviation of the measured cup position relative to the bone. This position is expressed by the components d_{ml} and d_{cc} of the bone–cup distance in medio-lateral and in cranio-caudal direction. The standard deviation of $\mathbf{d} = (d_{\mathrm{ml}}, d_{\mathrm{cc}})$ is estimated statistically considering the main entering errors. In the projective radiographic system, they arise from: the variability of the extrinsic parameters (the pelvis position and orientation at exposure), the variability of the intrinsic parameters (the position of the film relative to the focus), and the error in locating the required image points, which are the cup reference point and bony landmarks. The 2D bone–cup distance is formulated as a function subject to random variables representing these sources of error. Applying the principle of error propagation to this function yields an expression for the standard deviation of $\mathbf{d}$ which depends on the individual magnitudes of the entering errors. Instead of assessing the overall error of the measurement at once, it is thus traced back to its sources where the error magnitudes can be estimated more easily. The resulting expression for the standard deviation of the bone–cup distance contains coefficients which are the partial derivatives of $\mathbf{d}$ with respect to the random variables. These coefficients give additional information about the sensitivity of the measured distance towards the individual sources of error. The greater the partial derivative is, the more the corresponding entering error affects the precision.

Working out the scheme two compromises had to be made:

- As the scheme is based on a statistical approach, only knowledge about the random error or the precision of the migration measurement can be gained whereas its bias or accuracy is disregarded.

- The image structures in the radiograph arise from the superposition of bony structures along the rays. As the bony landmarks have a greater or smaller extension in z-direction, the 3D structures forming their projection alter at a change of the bone's orientation or position. However, it is very difficult to generally model this alteration. Therefore, the approximation is made that all points located in the radiograph are the projections of true 3D points having a constant position in the bone. Still, there is the possibility to consider the error originating from the change of the 3D structure projected by including it in the error in locating the bony landmarks in the image.

The scheme has been applied to four prominent methods for measuring cup migration, which previously had been tested experimentally: to the methods recommended by [Nunn et al. 1989], by [Dickob et al. 1994], by [Sutherland et al. 1982], and to EBRA (Ein-Bild-Röntgen-Analyse), a method proposed by [Krismer et al. 1995]. They are described

in detail in Sect. 2.2, subsequently to the definition of the x-ray coordinate system which is valid for all chapters of the thesis. In Sect. 2.3, the used notation is introduced. It is required for Sect. 2.4, where the analytical formulation of the bone–cup distances measured in the four methods is derived. The standard deviations of the resulting functions are approximated by propagating the standard deviations of the entering error variables. The underlying principle is shortly recapitulated in Sect. 2.5. In Sect. 2.6, the dimensions of the pelvis assumed are described, the magnitude of the entering errors is estimated, and the resulting expressions for the standard deviations of the measured bone–cup distances are presented.

2.1   Definition of the x-ray coordinate system

The radiographic imaging system is described by the x-ray coordinate system and the x-ray film plane (Fig. 2.1). The x- and the y-axis of this coordinate system, which has its origin at the x-ray source or focus, lie parallel to the vertical and the horizontal axis, respectively, of the film. The z-axis is directed towards the film having the distance f to the focus. At the standard x-y-position of the film, the principal point, i.e. the intersection of the z-axis with the film-plane, is assumed to coincide with the film center. The 3D pelvis points as well as the image points are represented in the x-ray coordinate system. In case of the latter, the z-coordinate is set to f.
The directions along the body axes are indicated by anatomical terms: "medio-lateral" means from the left to the right, "cranio-caudal" from the head to the feet, "ventral-dorsal" or "anterior-posterior" from the belly to the back. It is assumed that the medio-lateral, the cranio-caudal, and the ventral-dorsal direction is parallel to the x-, the y-, and the z-axis, respectively, if the patient lies on the x-ray table and the pelvis has its standard orientation. Thus, medio-lateral is used as a synonym for x-, cranio-caudal for y-, and ventral-dorsal for z-axis, -direction, or -distance.
For the sake of clarity, the terms "position" and "orientation" as well as "translation" and "rotation" are strictly distinguished. The vector $\mathbf{T} = (T_x, T_y, T_z)^\mathrm{T}$ represents the position of the pelvis in the x-ray system. The orientation is expressed by the Euler angles α, β, γ with respect to the axes of this system (Fig. 2.1). For the 3D rotation of the pelvis between two radiographs, the anatomical expressions "flexion–extension", "lateral–medial rotation", and "abduction–adduction" are avoided. Instead the geometrical terms (rotation around the x- or medio-lateral axis, around the y- or cranio-caudal axis, and around the z- or ventral-dorsal axis) are used. The change of the pelvis orientation with respect to the x- or to the y-axis is also termed "out-of-plane rotation".

2.2   Analysed methods for assessing migration

The four analysed methods well represent migration assessment in x-ray images, because they cover the traditional image evaluation [Nunn *et al.* 1989, Sutherland *et al.* 1982], the
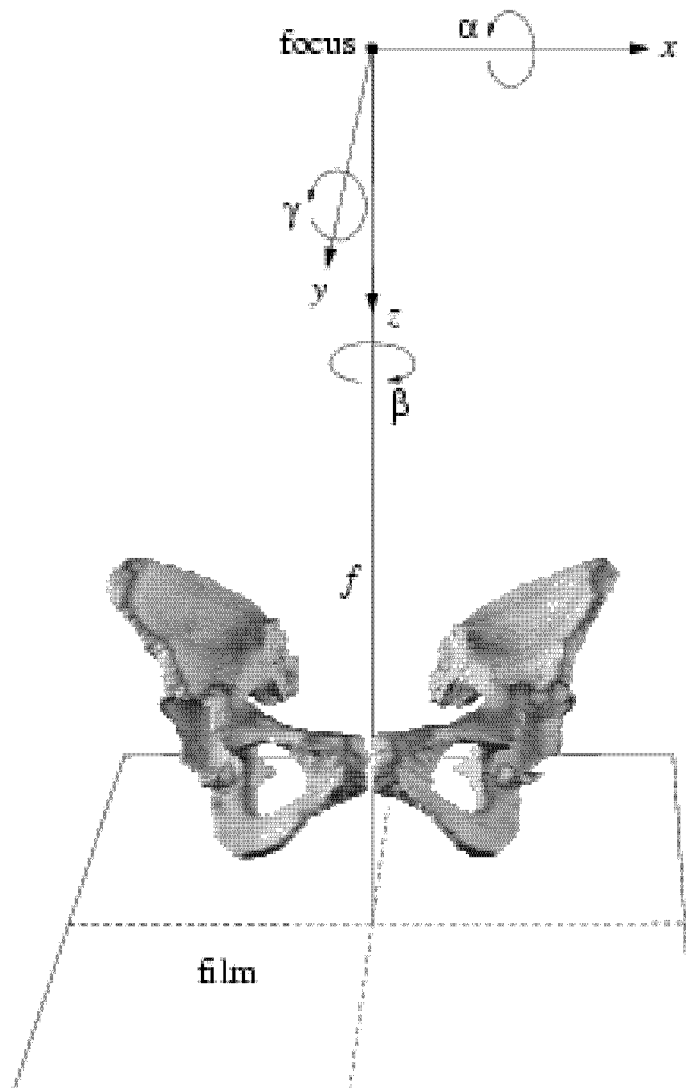
Figure 2.1: *The x-ray coordinate system.*
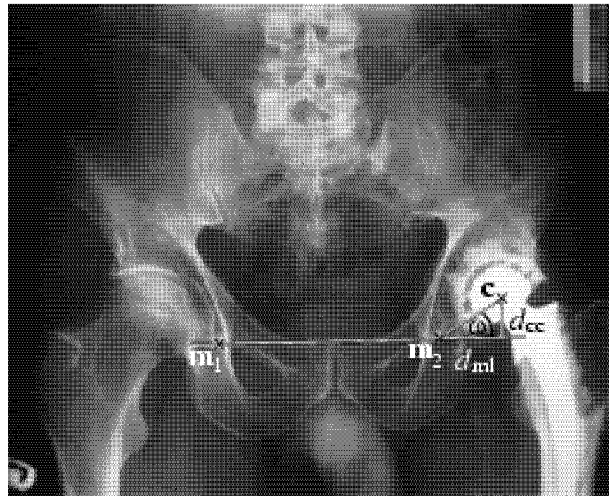
Figure 2.2: *The bone–cup distance in [Nunn et al. 1989] and [Dickob et al. 1994].*

use of digital radiographs [Dickob *et al.* 1994], and the more complex engineering approach [Krismer *et al.* 1995]. In the figures illustrating the methods some notation is used which is explained in the text.

2.2.1   Nunn *et al.* and Dickob *et al.*

In [Nunn *et al.* 1989], the left and the right teardrop figure, which are the projections of bony structures partly belonging to the hip socket, are used as bony landmarks. They are in most of the cases still visible after a total hip replacement (THR). The recommended film–focus distance is 900 mm. In the x-ray film, a reference line connecting the most caudal points of the teardrop figures (m_1 and m_2 in Fig. 2.2) is drawn using a pencil. The implant reference point (c) is the center of the projection of the femoral head (with the assumption of a polyethylene cup). It is found by overlaying the head's contour with a transparent sheet showing concentric circles. The medio-lateral distance corresponds to the distance along the reference line between the most caudal point of the teardrop figure next to the prosthesis and the implant reference point. The measured cranio-caudal distance corresponds to the distance perpendicular to the reference line between the just mentioned points.

The distances are corrected for magnification through multiplication by $\frac{r}{b}$, where r is the true radius of the femoral head and b the radius of its projection measured in the radiograph. In addition to the head position relative to the bone, the distance between the most caudal points of the teardrop figures (in the following the inter-teardrop distance) is determined in all radiographs of the patient's follow-up study. After correction for magnification, d_{ml} is multiplied by the quotient between the largest inter-teardrop distance and the one in the radiograph under study to correct for rotation of the pelvis around the cranio-caudal axis. For d_{cc}, no correction for rotation is considered.
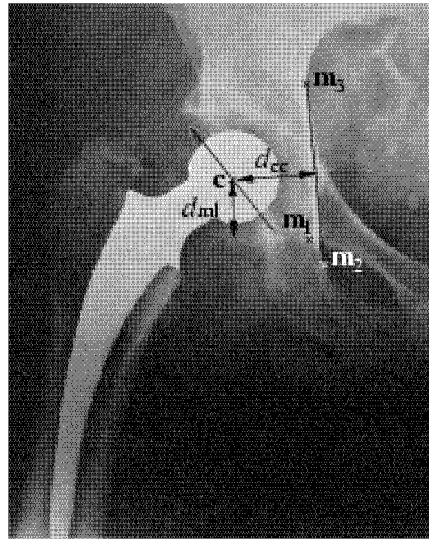
Figure 2.3: *The bone–cup distance according to [Sutherland et al. 1982].*

The procedure recommended in [Dickob *et al.* 1994] is very similar to the one just described. The only differences are the use of digitized instead of conventional radiographs and the choice of a different implant reference point. The latter is chosen to be the center of the metal ring at the cup's rim (see Fig. 2.3) in case of polyethylene cups. If a metal cup is implanted, the center of the cup's equatorial plane is used instead. The teardrop figure points and two points on the cup's contour are marked by mouse-clicking. The radius of the femoral head is determined by fitting a sphere to its circumference also using the mouse.

2.2.2 Sutherland *et al.*

In [Sutherland *et al.* 1982], the teardrop figure next to the prosthesis (m_1) and the Köhler line (the line in Fig. 2.3 connecting m_2 and m_3) are used as bony landmarks. The reference point of the implant (c) is the center of the metal ring at the cup's rim. The reference points and lines are marked in the image probably like in [Nunn *et al.* 1989] using a pencil. The medio-lateral distance corresponds to the distance between the cup reference point and the Köhler line. The definition of the cranio-caudal distance does not become completely clear in [Sutherland *et al.* 1982]. Maybe it is determined using the perpendicular to an additional horizontal line mentioned in this publication. As this is not stated explicitly, however, the straight-forward approach is assumed and d_{cc} is supposed to just correspond to the vertical image distance between the cup reference point and the most caudal point of the teardrop. The correction for magnification is the same as in [Nunn *et al.* 1989] and in [Dickob *et al.* 1994], whereas a correction for rotation is not considered.
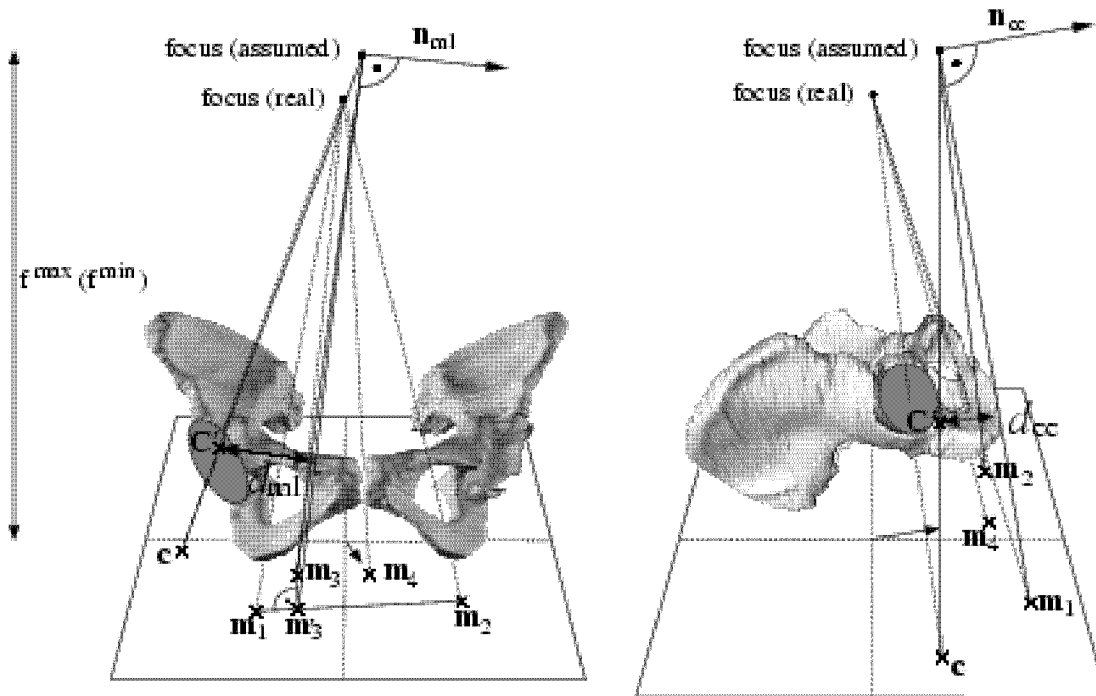
Figure 2.4: *The bone–cup distance according to [Krismer et al. 1995].*

2.2.3   EBRA

EBRA is available in two versions, the original one where the x-ray films are evaluated using a digitizer tablet and the more recent one based on digital radiographs. Their only difference is the data source used. Points on the contours of the foramina obturatoria (m_1, m_2, and m_3 in Fig. 2.4) are used as bony landmarks. In the assumed digital version of EBRA, which may be nowadays used more often, these points are defined by mouse-clicking. Like in [Dickob *et al.* 1994], the cup reference point (**c**) is chosen to be the center of either the cup's equatorial plane or the metal ring at the cup's rim. Several points of the visible cup contour are marked and a least squares estimation is applied to precisely determine the position of the cup. The image coordinates of the bony landmarks and of the cup reference point are represented relative to the assumed principal point. This point is estimated to be the midpoint of the line connecting the film center and the cranial end of the symphysis pubis in the image (m_4). The bone–cup distance is defined as the distance (averaged as described below) of the reconstructed 3D cup reference point (**C'**) to a medio-lateral and to a cranio-caudal reference plane. In Fig. 2.4, the normals to these planes are shown (n_{ml} and n_{cc}).

In order to get an idea of the spatial situation at exposure, the general extremal values of the distance between implant and film plane were determined experimentally [Russe 1988, Krismer *et al.* 1995]. Using these values, the known real radius of the femoral head, and the radius of the femoral head in the image a maximal and a minimal value for the film–

focus distance (f^{min}, f^{max}) are calculated for each radiograph. If the resulting minimal value falls short of 900 mm or the maximal value exceeds 1300 mm, $f^{\mathrm{min}} = 900$ mm or $f^{\mathrm{max}} = 1300$ mm is set.

The 3D cup reference point and the reference planes are computed inserting once the minimal and once the maximal implant–film distance and the dependent focus position given by f^{min} or f^{max} and the principal point. The 3D reference point of the cup is obtained by reprojection of **c**. The reference planes are constructed using a medio-lateral and a cranio-caudal tangent to the foramina obturatoria in the image. The medio-lateral tangent is the line connecting the most caudal image points $\mathbf{m}_1$ and $\mathbf{m}_2$ of the foramina obturatoria. The cranio-caudal tangent is the line which is perpendicular to the medio-lateral one and intersects the most medial image point of the foramen obturatum next to the prosthesis. In Fig. 2.4, the cranio-caudal tangent is the line connecting $\mathbf{m}_3$ and $\mathbf{m}_3'$. For the distance of the 3D cup reference point to the medio-lateral or cranio-caudal plane two values result, according to the two values for the implant–film distance inserted. As final bone–cup distance ($d_{\mathrm{ml}}, d_{\mathrm{cc}}$) in an individual radiograph the mean of the resulting plane–cup distances is taken.

After the determination of the bone–cup distance a comparability algorithm is applied to reduce the influence of pelvis rotation between two exposures: A comparability limit is defined using additional image distances between certain bony structures strongly affected by rotation. The radiographs of the follow-up study are subdivided into pairs of comparable radiographs. These are radiographs between which the additional image distances do not differ more than a certain amount, the "comparability limit", which is usually 2 mm or 3 mm. Thus, the rotation between the comparable radiographs is implicitly limited. The migration at a certain time is defined as the mean change of d_{ml} and d_{cc} in all pairs of comparable radiographs whose first exposure was made before and whose second exposure was made after the time point.

2.3 Parameters and variables of the bone–cup distance

The components of the bone–cup distance can be represented as the function $\mathbf{d} = \mathbf{d}(v_i, p_j) = (d_{\mathrm{ml}}(v_i, p_j), d_{\mathrm{cc}}(v_i, p_j))^{\mathrm{T}}$ depending on random variables v_i ($i = 1, ..., l$) and on parameters p_j ($j = 1, ..., m$). The random variables can change from radiograph to radiograph and describe sources of error of the imaging system. The predetermined parameters are supposed to remain constant during the acquisition of the follow-up series of the THR. They mainly describe anatomical points of the pelvis at its mean orientation and position, where the position vector **T** and the orientation angles α, β, γ (see 2.1) are defined to be zero.

The random variables v_i are the following:

- The variables describing the variability of the extrinsic parameters, i.e. the deviation of the pelvis' orientation and position at exposure relative to its mean orientation and position. The deviating orientation is described by the angles $\delta\alpha$, $\delta\beta$, and $\delta\gamma$ of

the pelvis' rotation around the x-, y-, and z-axis, respectively. The deviating position is expressed by the translation vector $\delta \mathbf{T} = (\delta T_x, \delta T_y, \delta T_z)^{\mathrm{T}}$.

- The variables describing the variability of the intrinsic parameters. These are the deviations δf and $\delta \mathbf{t} = (\delta t_x, \delta t_y)^{\mathrm{T}}$ of the intrinsic parameters at exposure from their mean values. The mean values are given by the average film–focus distance f and the expected principal point assumed to be the film center.

- The variables describing the error of measurements in the x-ray image. These variables are represented by $\delta \mathbf{c}$, $\delta \mathbf{m}_1$,..., $\delta \mathbf{m}_n$ and δb, which correspond to the deviations from the expected value of respectively: the measured image coordinates of the cup reference point, those of the bony landmarks, and the measured radius of the femoral head in the image.

The parameters p_j of the function $\mathbf{d}$ are

- the 3D coordinates $\mathbf{C}_0$ of the reference point of the cup.

- the n ($n = 2$–4) 3D coordinates $\mathbf{M}_{10}, ..., \mathbf{M}_{n0}$ of the bony structures; their projections are the landmarks defining the bone reference points, lines or planes.

- the 3D coordinates $\mathbf{Z}$ of the center of rotation of the pelvis.

- the known radius of the femoral head, r.

- the assumed mean [Dickob *et al.* 1994, Sutherland *et al.* 1982, Krismer *et al.* 1995] or the given nominal [Nunn *et al.* 1989] value f of the film–focus distance.

- concerning EBRA, the predetermined extremal values $h^{\mathrm{min}} = 180\,\mathrm{mm}$ and $h^{\mathrm{max}} = 270\,\mathrm{mm}$ of the distance between 3D implant reference point and film, and the predefined limits $900\,\mathrm{mm}$ and $1300\,\mathrm{mm}$ for the estimated extremal values of the film–focus distance [Russe 1988, Krismer *et al.* 1995].

2.4 Analytical representation of the measured bone–cup distance

This section is based on the notation introduced previously and on the description of the analysed methods in Sect. 2.2. The bone–cup distance as determined in [Nunn *et al.* 1989, Dickob *et al.* 1994, Sutherland *et al.* 1982] can be expressed by relatively simple functions because these methods mainly consist of the measurement of image distances. On the other hand, the function representing the bone–cup distance determined in [Krismer *et al.* 1995] is quite complicated.

The measured image coordinates of the cup reference point and of the bony landmarks can be expressed for all four methods in the same way. The random 3D positions $\mathbf{C}$ and

$\mathbf{M}_k$ of the pelvic points depend on their mean positions and on the pelvis orientation and position in an individual radiograph:

$$\mathbf{C}(\delta\alpha, \delta\beta, \delta\gamma, \delta\mathbf{T}) = \mathbf{Z} + \mathbf{R} \cdot (\mathbf{C}_0 - \mathbf{Z}) + \delta\mathbf{T}$$
$$\mathbf{M}_k(\delta\alpha, \delta\beta, \delta\gamma, \delta\mathbf{T}) = \mathbf{Z} + \mathbf{R} \cdot (\mathbf{M}_{k0} - \mathbf{Z}) + \delta\mathbf{T}$$

The orientation of the pelvis relative to the mean orientation is represented by the rotation matrix $\mathbf{R}$:

$$\mathbf{R} = \begin{pmatrix} \cos\delta\beta \cos\delta\gamma & \sin\delta\alpha \sin\delta\beta \cos\delta\gamma - \cos\delta\alpha \sin\delta\gamma & \cos\delta\alpha \sin\delta\beta \cos\delta\gamma + \sin\delta\alpha \sin\delta\gamma \\ \cos\delta\beta \sin\delta\gamma & \sin\delta\alpha \sin\delta\beta \sin\delta\gamma + \cos\delta\alpha \cos\delta\gamma & \cos\delta\alpha \sin\delta\beta \sin\delta\gamma - \sin\delta\alpha \cos\delta\gamma \\ -\sin\delta\beta & \sin\delta\alpha \cos\delta\beta & \cos\delta\alpha \cos\delta\beta \end{pmatrix} \quad (2.1)$$

The imaging system is modeled by a pinhole camera (see Fig. 2.5). The x-ray source corresponds to the optical center and the radiographic film to the retinal plane. In comparison to a standard camera, the system has the peculiarity that the z-distance between object and film plane is constant, as the vertical distance between examination table and film cassette is fixed. This means that an alteration of the film–focus distance δf leads to the same change of the z-distance of an anatomical point to the focus.
The projections of $\mathbf{C}$ and $\mathbf{M}_k$ on the film plane are given by

$$(f + \delta f) \cdot \left(\frac{C_x}{C_z + \delta f}, \frac{C_y}{C_z + \delta f} \right)^{\mathrm{T}} \quad \text{and} \quad (f + \delta f) \cdot \left(\frac{M_{kx}}{M_{kz} + \delta f}, \frac{M_{ky}}{M_{kz} + \delta f} \right)^{\mathrm{T}}.$$

For [Krismer *et al.* 1995, Sutherland *et al.* 1982, Dickob *et al.* 1994] f=110 cm was assumed, for [Nunn *et al.* 1989] the proposed nominal value f=90 cm was taken. Considering the variability of the principal point and the error in locating the bony landmarks and the cup reference point in the image, the image coordinates used to determine the bone–cup distance are (see Fig. 2.5)

$$\mathbf{c}(\delta\alpha, \delta\beta, \delta\gamma, \delta\mathbf{T}, \delta f, \delta\mathbf{t}, \delta\mathbf{c}) = (f + \delta f) \begin{pmatrix} \frac{C_x}{C_z + \delta f} \\ \frac{C_y}{C_z + \delta f} \end{pmatrix} + \delta\mathbf{t} + \delta\mathbf{c}, \quad (2.2)$$

$$\mathbf{m}_k(\delta\alpha, \delta\beta, \delta\gamma, \delta\mathbf{T}, \delta f, \delta\mathbf{t}, \delta\mathbf{m}_k) = (f + \delta f) \begin{pmatrix} \frac{M_{kx}}{M_{kz} + \delta f} \\ \frac{M_{ky}}{M_{kz} + \delta f} \end{pmatrix} + \delta\mathbf{t} + \delta\mathbf{m}_k. \quad (2.3)$$

For the analytical representation of the correction for magnification, the dependence of the femoral head's contour in the image from C_z is additionally required. The projection of the spherical femoral head is in fact an ellipse. The difference between the long and the short axis of this ellipse lies at about 0.2mm [Russe 1988] and is neglected here. The measured radius of the femoral head's contour is equated to the ellipse's short axis. The formula of the short axis was deduced by [Russe 1988] and is

$$b(\delta\alpha, \delta\beta, \delta\gamma, \delta T_z, \delta f) = \frac{f + \delta f}{\sqrt{\left(\frac{C_z + \delta f}{r} \right)^2 - 1}}, \quad (2.4)$$
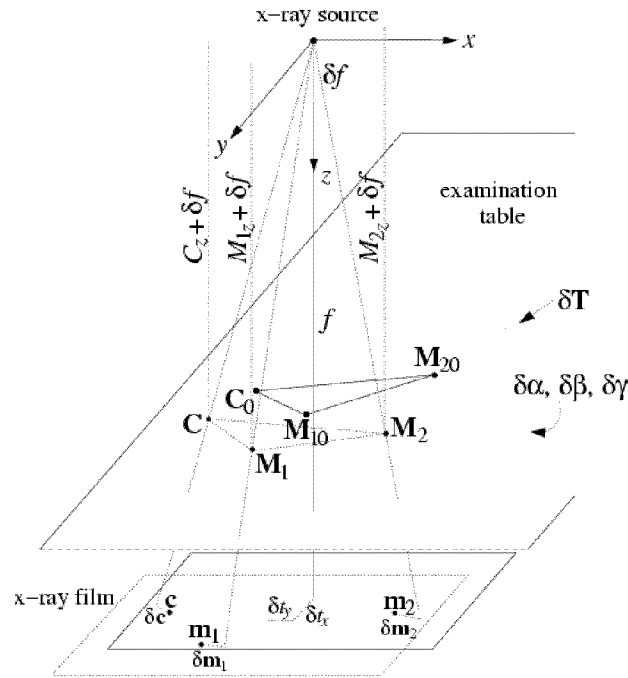
Figure 2.5: *The projection of anatomical points on the film. Dotted lines indicate the sources of error.*

where f is replaced by $f + \delta f$ and C_z by $C_z + \delta f$, to take the variability of the film–focus distance at exposure into account. For r the real radius of the femoral head is inserted, which is usually $r = 14\,\mathrm{mm}$.

2.4.1   Formula for the distance in Nunn *et al.* and Dickob *et al.*

As can be seen in Fig. 2.2, the components of the image distance between cup and reference line are given by $\cos\omega \cdot |\mathbf{c} - \mathbf{m_2}|$ and $\sin\omega \cdot |\mathbf{c} - \mathbf{m_2}|$. For the deduction of the final measured bone–cup distance $\mathbf{d}$, the correction of both components for magnification and of d_{ml} for rotation need to be considered. The correction for magnification corresponds to the multiplication by $\frac{r}{b+\delta b}$. In this quotient, b is replaced $b + \delta b$ to take into account the variability in determining the radius of the femoral head in the image.

The correction for rotation corresponds to the multiplication of the medio-lateral component by the quotient between the maximum inter-teardrop distance of the series and the inter-teardrop distance $|\mathbf{m_2} - \mathbf{m_1}|$ in a random radiograph. In this context, the maximum inter-teardrop distance has the role of a constant coefficient and hence has a negligible influence on the variability of the final bone–cup distance. For simplicity, it is set to the

mean distance between the teardrop figures. It is indicated with $|\mathbf{m}_{20} - \mathbf{m}_{10}|$ and calculated setting to zero all random variables in the expression (2.3):

$$|\mathbf{m}_{20} - \mathbf{m}_{10}| = f \left| \left(\frac{M_{20x}}{M_{20z}}, \frac{M_{20y}}{M_{20z}} \right)^{\mathrm{T}} - \left(\frac{M_{10x}}{M_{10z}}, \frac{M_{10y}}{M_{10z}} \right)^{\mathrm{T}} \right|$$

Considering the correction for magnification and the one for rotation, the bone–cup distance is

$$\mathbf{d} = \frac{r}{b + \delta b} \left(\begin{array}{c} \cos \omega \cdot |\mathbf{c} - \mathbf{m_2}| \cdot \frac{|\mathbf{m}_{20} - \mathbf{m}_{10}|}{|\mathbf{m_2} - \mathbf{m_1}|} \\ \sin \omega \cdot |\mathbf{c} - \mathbf{m_2}| \end{array} \right) .$$

The term $\cos \omega \cdot |\mathbf{c} - \mathbf{m_2}|$ is the dot product of $(\mathbf{c} - \mathbf{m_2})$ and $(\mathbf{m_2} - \mathbf{m_1})$ divided by $|\mathbf{m_2} - \mathbf{m_1}|$. The cranio-caudal component can be derived using the dot product between $(\mathbf{c} - \mathbf{m_2})$ and the perpendicular of $(\mathbf{m_2} - \mathbf{m_1})$, which is $\left(-(m_{2_y} - m_{1_y}), (m_{2_x} - m_{1_x}) \right)^{\mathrm{T}}$. Hence, the final result for the distance vector is:

$$\mathbf{d} = \frac{r}{b + \delta b} \left(\begin{array}{c} \left((c_x - m_{2x})(m_{2x} - m_{1x}) + (c_y - m_{2y})(m_{2y} - m_{1y}) \right) \cdot \frac{|\mathbf{m}_{20} - \mathbf{m}_{10}|}{|\mathbf{m_2} - \mathbf{m_1}|^2} \\ \left((c_y - m_{2y})(m_{2x} - m_{1x}) - (c_x - m_{2x})(m_{2y} - m_{1y}) \right) \cdot \frac{1}{|\mathbf{m_2} - \mathbf{m_1}|} \end{array} \right) \quad (2.5)$$

2.4.2 Formula for the distance in Sutherland *et al.*

The medio-lateral component of the bone–cup distance in [Sutherland *et al.* 1982] is given by distance of the cup reference point $\mathbf{c}$ to the Köhler line reaching from $\mathbf{m_2}$ to $\mathbf{m_3}$ in Fig. 2.3. Analogously to the cranio-caudal component in [Nunn *et al.* 1989], it can be derived by the dot product between $\mathbf{c} - \mathbf{m_2}$ and the perpendicular to $\mathbf{m_3} - \mathbf{m_2}$. The cranio-caudal distance is assumed to be simply the difference of the y-coordinates of $\mathbf{c}$ and $\mathbf{m_1}$, and the correction for the magnification is the same as in [Nunn *et al.* 1989] and [Dickob *et al.* 1994]. Thus, the distance vector is:

$$\mathbf{d} = \frac{r}{b + \delta b} \left(\begin{array}{c} \left((c_y - m_{2y})(m_{3x} - m_{2x}) - (c_x - m_{2x})(m_{3y} - m_{2y}) \right) \cdot \frac{1}{|\mathbf{m_3} - \mathbf{m_2}|} \\ m_{1y} - c_y \end{array} \right) \quad (2.6)$$

2.4.3 Formula for the distance in EBRA

As in Sect. 2.2.3 described, the distance of the reconstructed 3D cup reference point $\mathbf{C'}$ to a medio-lateral and to a cranio-caudal reference-plane with the normals $\mathbf{n}_{ml}$ and $\mathbf{n}_{cc}$ is measured. The two components are given by

$$d_{\mathrm{ml}} = \mathbf{n}_{ml}^{\mathrm{T}} \cdot \mathbf{C'} \quad \text{and} \quad d_{\mathrm{cc}} = \mathbf{n}_{cc}^{\mathrm{T}} \cdot \mathbf{C'} \ . \quad (2.7)$$

In order to calculate $\mathbf{C'}$, $\mathbf{n}_{ml}$, and $\mathbf{n}_{cc}$ an estimate of the film–focus constellation is required. The x-y-position of the film relative to the focus is defined by the principal point. This point is given by $\frac{1}{2}\mathbf{m_4}$ as it is estimated to be the midpoint between the symphysis pubis'

cranial end $\mathbf{m}_4$ and the film center. A minimal and a maximal value for the z-position of the film are calculated inserting r, b as expressed by (2.4), and the extremal values for the film–implant distance $h^{\mathrm{min,max}}$ in the equation

$$f^{\mathrm{min,max}} = (b + \delta b) \cdot \left(\arcsin \left(\frac{r}{\sqrt{(b + \delta b)^2 + (h^{\mathrm{min,max}})^2}} \right) + \arctan \left(\frac{h^{\mathrm{min,max}}}{b + \delta b} \right) \right) \; . \quad (2.8)$$

Into the original formula [Krismer *et al.* 1995, page 1228], $b + \delta b$ is inserted instead of b to take the variability of measuring the radius of the femoral head into account. If f^{min} is smaller than 900 mm or f^{max} is greater than 1300 mm, the film–focus distance is set to 900 mm or 1300 mm, respectively.

The z-coordinate of the 3D cup reference point $\mathbf{C}'$ is $f^{\mathrm{min,max}} - h^{\mathrm{min,max}}$. The x-y-coordinates are obtained by re-projecting $\mathbf{c}$ considering the x-y-position of the film:

$$C'^{\mathrm{min,max}}_{x,y} = \left(f^{\mathrm{min,max}} - h^{\mathrm{min,max}} \right) \cdot \left(\frac{c_{x,y} - \frac{1}{2} m_{4x,y}}{f^{\mathrm{min,max}}} \right) \; .$$

The normal of the reference-plane $\mathbf{n}_{cc}$ is the normalized cross product of the rays reaching from the focus to $\mathbf{m}_1$ and to $\mathbf{m}_2$ (see Fig. 2.4):

$$\mathbf{n}_{cc} = \frac{\begin{pmatrix} m_{1x} - \frac{m_{4x}}{2} \\ m_{1y} - \frac{m_{4y}}{2} \\ f^{\mathrm{min,max}} \end{pmatrix} \times \begin{pmatrix} m_{2x} - \frac{m_{4x}}{2} \\ m_{2y} - \frac{m_{4y}}{2} \\ f^{\mathrm{min,max}} \end{pmatrix}}{\left| \begin{pmatrix} m_{1x} - \frac{m_{4x}}{2} \\ m_{1y} - \frac{m_{4y}}{2} \\ f^{\mathrm{min,max}} \end{pmatrix} \times \begin{pmatrix} m_{2x} - \frac{m_{4x}}{2} \\ m_{2y} - \frac{m_{4y}}{2} \\ f^{\mathrm{min,max}} \end{pmatrix} \right|} \quad (2.9)$$

The medio-lateral reference-plane is defined by $\mathbf{m}_3$ and $\mathbf{m}'_3$, which is the projection of $\mathbf{m}_3$ on the vector $\mathbf{m}_1 - \mathbf{m}_2$:

$$\mathbf{m}'_3 = \mathbf{m}_1 + \frac{(\mathbf{m}_3 - \mathbf{m}_1)^{\mathrm{T}} \cdot (\mathbf{m}_2 - \mathbf{m}_1)}{|\mathbf{m}_2 - \mathbf{m}_1|^2} (\mathbf{m}_2 - \mathbf{m}_1)$$

Replacing $\mathbf{m}_1$ with $\mathbf{m}'_3$ and $\mathbf{m}_2$ with $\mathbf{m}_3$ in equation (2.9), $\mathbf{n}_{ml}$ is constructed analogously to $\mathbf{n}_{cc}$. Now, with the formulas for $f^{\mathrm{min,max}}$, $\mathbf{C}'$, $\mathbf{n}_{cc}$, and $\mathbf{n}_{ml}$, the bone–cup distance can be calculated using the equations (2.7). The result is:

$$d_{\mathrm{ml}}^{\mathrm{min,max}} = \left(f^{\mathrm{min,max}} - h^{\mathrm{min,max}} \right) \cdot$$

$$\frac{\left(\left(\begin{pmatrix} m_{1x} + \frac{(\mathbf{m}_3 - \mathbf{m}_1)^{\mathrm{T}} \cdot (\mathbf{m}_2 - \mathbf{m}_1)}{|\mathbf{m}_2 - \mathbf{m}_1|^2}(m_{2x} - m_{1x}) - \frac{m_{4x}}{2} \\ m_{1y} + \frac{(\mathbf{m}_3 - \mathbf{m}_1)^{\mathrm{T}} \cdot (\mathbf{m}_2 - \mathbf{m}_1)}{|\mathbf{m}_2 - \mathbf{m}_1|^2}(m_{2y} - m_{1y}) - \frac{m_{4y}}{2} \\ f^{\mathrm{min,max}} \end{pmatrix} \times \begin{pmatrix} m_{3x} - \frac{m_{4x}}{2} \\ m_{3y} - \frac{m_{4y}}{2} \\ f^{\mathrm{min,max}} \end{pmatrix} \right)^{\mathrm{T}} \cdot \begin{pmatrix} c_x - \frac{m_{4x}}{2} \\ \overline{f^{\mathrm{min,max}}} \\ c_y - \frac{m_{4y}}{2} \\ \overline{f^{\mathrm{min,max}}} \\ 1 \end{pmatrix} \right)}{\left| \begin{pmatrix} m_{1x} + \frac{(\mathbf{m}_3 - \mathbf{m}_1)^{\mathrm{T}} \cdot (\mathbf{m}_2 - \mathbf{m}_1)}{|\mathbf{m}_2 - \mathbf{m}_1|^2}(m_{2x} - m_{1x}) - \frac{m_{4x}}{2} \\ m_{1y} + \frac{(\mathbf{m}_3 - \mathbf{m}_1)^{\mathrm{T}} \cdot (\mathbf{m}_2 - \mathbf{m}_1)}{|\mathbf{m}_2 - \mathbf{m}_1|^2}(m_{2y} - m_{1y}) - \frac{m_{4y}}{2} \\ f^{\mathrm{min,max}} \end{pmatrix} \times \begin{pmatrix} m_{3x} - \frac{m_{4x}}{2} \\ m_{3y} - \frac{m_{4y}}{2} \\ f^{\mathrm{min,max}} \end{pmatrix} \right|}$$

$$d_{\mathrm{cc}}^{\mathrm{min,max}} = \left(f^{\mathrm{min,max}} - h^{\mathrm{min,max}}\right) \cdot$$

$$\frac{\left(\left(\begin{pmatrix} m_{1x}-\frac{m_{4x}}{2} \\ m_{1y}-\frac{m_{4y}}{2} \\ f^{\mathrm{min,max}} \end{pmatrix} \times \begin{pmatrix} m_{2x}-\frac{m_{4x}}{2} \\ m_{2y}-\frac{m_{4y}}{2} \\ f^{\mathrm{min,max}} \end{pmatrix}\right)\right)^{\mathrm{T}} \cdot \begin{pmatrix} c_x-\frac{m_{4x}}{2} \\ f^{\mathrm{min,max}} \\ c_y-\frac{m_{4y}}{2} \\ f^{\mathrm{min,max}} \\ 1 \end{pmatrix}}{\left| \begin{pmatrix} m_{1x}-\frac{m_{4x}}{2} \\ m_{1y}-\frac{m_{4y}}{2} \\ f^{\mathrm{min,max}} \end{pmatrix} \times \begin{pmatrix} m_{2x}-\frac{m_{4x}}{2} \\ m_{2y}-\frac{m_{4y}}{2} \\ f^{\mathrm{min,max}} \end{pmatrix} \right|}$$

$$(2.10)$$

For the sake of clarity, the insertion of the expression (2.8) for $f^{\mathrm{min,max}}$ was omitted. The final components of the bone–cup distance are given by the mean of $d_{\mathrm{ml}}^{\mathrm{min}}$, $d_{\mathrm{ml}}^{\mathrm{max}}$ and of $d_{\mathrm{cc}}^{\mathrm{min}}$, $d_{\mathrm{cc}}^{\mathrm{max}}$.

2.5 Derivation of the standard deviation

Assuming that the random variables v_i are uncorrelated, the covariance matrix of the random vector $\mathbf{v} = (v_1, ..., v_l)^{\mathrm{T}} = (\delta\alpha,\ \delta\beta,\ \delta\gamma,\ \delta T_x,\ \delta T_y,\ \delta T_z,\ \delta c_x,\ \delta c_y,\ \delta m_{1x},...,\delta m_{nx}, \delta m_{1y},...,\delta m_{ny},\ \delta b,\ \delta f,\ \delta t_x,\ \delta t_y)^{\mathrm{T}}$ is diagonal and has the following form:

$$\mathbf{\Sigma_{vv}} = \begin{pmatrix} \sigma_{v_1}^2 & 0 & . & . & . & 0 \\ 0 & \sigma_{v_2}^2 & & & & . \\ . & & . & & & . \\ . & & & . & & . \\ . & & & & . & 0 \\ 0 & . & & . & 0 & \sigma_{v_l}^2 \end{pmatrix},$$

where $\sigma_{v_i}^2$ are the variances of the variables v_i.

The covariance matrix $\mathbf{\Sigma_{dd}}$ of the distance vector is approximated by application of the principle of propagation of variances (see [Mikhail 1976], e.g.) and by linearization of $\mathbf{d}(v_i, p_j)$ in terms of $\mathbf{v}$. Neglecting the second and higher-order terms, this matrix is

$$\mathbf{\Sigma_{dd}} = \mathbf{J}\mathbf{\Sigma_{vv}}\mathbf{J}^{\mathrm{T}} = \begin{pmatrix} \sum_i \sigma_{v_i}^2 \cdot \left(\left.\frac{\partial d_{\mathrm{ml}}}{\partial v_i}\right|_{v_i=\bar{v}_i}\right)^2 & \sum_i \sigma_{v_i}^2 \cdot \left.\frac{\partial d_{\mathrm{ml}}}{\partial v_i}\frac{\partial d_{\mathrm{cc}}}{\partial v_i}\right|_{v_i=\bar{v}_i} \\ \sum_i \sigma_{v_i}^2 \cdot \left.\frac{\partial d_{\mathrm{ml}}}{\partial v_i}\frac{\partial d_{\mathrm{cc}}}{\partial v_i}\right|_{v_i=\bar{v}_i} & \sum_i \sigma_{v_i}^2 \cdot \left(\left.\frac{\partial d_{\mathrm{cc}}}{\partial v_i}\right|_{v_i=\bar{v}_i}\right)^2 \end{pmatrix},$$

where $\mathbf{J}$ is the Jacobian. It is given by the partial derivatives of $\mathbf{d}$ with respect to the variables v_i at the mean value $\bar{\mathbf{v}} = (0, 0, ..., 0)^{\mathrm{T}}$ of $\mathbf{v}$.

The square roots of covariance matrix' diagonal elements are the standard deviations looked for:

$$\sigma_{d_{\mathrm{ml}}} = \sqrt{\sum_i \left(\sigma_{v_i} \cdot \left.\frac{\partial d_{\mathrm{ml}}}{\partial v_i}\right|_{v_i=\bar{v}_i}\right)^2}, \qquad \sigma_{d_{\mathrm{cc}}} = \sqrt{\sum_i \left(\sigma_{v_i} \cdot \left.\frac{\partial d_{\mathrm{cc}}}{\partial v_i}\right|_{v_i=\bar{v}_i}\right)^2} \qquad (2.11)$$

2.6   Results of the error analysis

The functions for the bone–cup distance (2.5), (2.6), and (2.10) were entered in Mathematica [Wolfram 1996]. In doing so the expressions for $\mathbf{c}$, $\mathbf{m}_k$, and b as given by (2.2), (2.3), and (2.4) were inserted in each function. Thus, the resulting expressions for $\mathbf{d}$ were depending only on the random variables v_i and on the parameters f, r, $h^{\text{min,max}}$ (used only in EBRA), $\mathbf{C}_0$, $\mathbf{M}_{k0}$, and $\mathbf{Z}$. The values for the parameters were inserted, and the partial derivatives $\frac{\partial d_{\text{ml/cc}}}{\partial v_i}$ at $\mathbf{v} = \bar{\mathbf{v}}$ were calculated. In the following subsection, the anatomical points defining $\mathbf{C}_0$, $\mathbf{M}_{k0}$, and $\mathbf{Z}$ are described. Their coordinates are listed in Tab. 2.1. Afterwards, in Sect. 2.6.2, the assumed standard deviations σ_{v_i} of the random variables corresponding to the magnitudes of the entering errors are listed. The resulting expressions for $\sigma_{d_{\text{ml}}}$ and $\sigma_{d_{\text{cc}}}$ for each of the analysed methods are presented in the Sections 2.6.3 to 2.6.5. These sums of error components contain the partial derivatives (not listed if they are smaller than 10^{-5}), which are the measures for the influence of the sources of error. The overall standard devation of the measured bone–cup distance is calculated at the end of each of these subsections by inserting the values of the σ_{v_i}.

In [Nunn *et al.* 1989, Dickob *et al.* 1994, Sutherland *et al.* 1982], neither a sorting of the radiographs according to the pelvis orientation nor an a posteriori analysis of the measured cup displacement considering all images of a follow-up series is described. Hence, the simplest case is assumed of observing the difference of the bone–cup distance in two random radiographs. The application of the principle of error propagation to this difference yields the final standard deviation $\sqrt{2} \cdot (\sigma_{d_{\text{ml}}}, \sigma_{d_{\text{cc}}})$ of the migration (under the assumption that the error in measuring the bone–cup distance is constant). In order to determine the standard deviation of the migration in EBRA, the effect of the comparability algorithm is taken into account as described in Sect. 2.6.5.

2.6.1   3D-position of the cup and of the bony landmarks

Calculating the partial derivatives of the bone–cup distances requires the 3D coordinates of the following points: the most caudal points of the teardrop figures [Nunn *et al.* 1989, Dickob *et al.* 1994, Sutherland *et al.* 1982], the 3D points defining the Köhler line [Sutherland *et al.* 1982], the most caudal and the most medial points of the foramina obturatoria and the symphysis pubis' cranial end [Krismer *et al.* 1995], the cup reference point, and the pelvic rotational center. The 3D coordinates of these points were estimated using the data of the Visible Human Female [National Library of Medicine 2001]. These data were visualized in 3D with a resolution of 1.5 pixel per millimeter through a computer program developed at our institute [Székely *et al.* 1998].

The 3D coordinates $\mathbf{C}_0$, $\mathbf{M}_{k0}$, and $\mathbf{Z}$ give the positions of the points at the mean pelvis orientation and position in the x-ray system. The mean orientation is taken to be identical to the orientation of the pelvis of the Visible Human Female. The mean pelvis x-y-position is defined by the expected intersection of the ray along the z-axis with the pelvis. According to the clinical practice, it is assumed that this intersection lies at the cranial-ventral end of the symphysis pubis. The mean pelvis z-position depends on the film–focus distance f

point of the pelvis	$x[\mathrm{mm}]$	$y[\mathrm{mm}]$	$f - z[\mathrm{mm}]$
center of femoral head $\mathbf{C}_0$	98.0	−18.3	230.0
caudal points of teardrop figures ($\mathbf{M}_{10}, \mathbf{M}_{20}$)	±64.7	−4.2	227.7
lateral point of border of ilium ($\mathbf{M}_{30}$)	72.0	−66.0	224.7
lateral point of foramen obturatorium ($\mathbf{M}_{20}$)	63.0	7.3	219.0
caudal points of foramina obturatoria ($\mathbf{M}_{10}, \mathbf{M}_{20}$)	±55.7	22.3	212.3
medial point of foramen obturatorium ($\mathbf{M}_{30}$)	33.0	12.0	237.3
middle cranial end of symphysis pubis ($\mathbf{M}_{40}$)	0.0	0.0	270.0
rotational center $\mathbf{Z}$	0.0	−60.3	111.3

Table 2.1: *Anatomical points in the pelvis of the Visible Human Female.*

and on the distance between film plane and the mattress lying on the examination table, which is assumed to be 100 mm. In Tab. 2.1, the averaged values of the points' coordinates measured on the left and on the right side of the pelvis are listed. The z-positions of the points are represented independently from f as heights above the film plane. These heights were obtained by adding the distance between film plane and mattress to the measured z-distances between the anatomical points and the table of the Visible Human Female. The center of the femoral head was taken as 3D cup reference point. The height of the teardrop figures in Tab. 2.1 is the mean height of the acetabular notch forming the caudal part of the teardrop figures in the radiograph [Kölbel and Golzo 1977, Peic 1971]. According to the definition in [Hubbard 1969] and the figures in [Hubbard 1969] and [Sutherland *et al.* 1982], the Köhler line is assumed to be defined by the most lateral point of the ipsilateral linea arcuata and of the ipsilateral foramen obturatum. The rotational center was supposed to lie in the body's median plane and hence its x-coordinate was assumed to be zero. Its y- and its z-coordinate were assumed to be defined by the y-z-position of the most dorsal points (left and right side) of the sacrum.

2.6.2   Magnitudes of the entering errors

The determination of the overall error of the bone–cup distance requires the standard deviations of the variables describing the sources of error. These quantities were set as far as possible to previously published estimates of the magnitudes of the entering errors. However, for some sources of error no data could be found in the literature and the related standard deviations had to be estimated intuitively.

- In [Sutherland *et al.* 1982], a mean change of pelvis orientation of 7.8° with respect to the x-axis and of 4.5° with respect to the y-axis is stated. According to [Krismer *et al.* 1995], the rotation around these two axes in EBRA is limited by the comparability algorithm to 1.0° and to 2.5°, respectively (choosing a comparability limit of 2 mm). Taking the reported angles as 66% confidence intervals, the corresponding standard deviations are $\sigma_{\delta\alpha} = 3.9°$ and $\sigma_{\delta\beta} = 2.3°$ if no comparability algorithm is applied. In case of comparable radiographs they are $\sigma_{\delta\alpha} = 0.5°$ and $\sigma_{\delta\beta} = 1.25°$.

The pelvis orientation with respect to the z-axis has not been considered in the literature up to the present. Its standard deviation is estimated to be $\sigma_{\delta\gamma} = 3.0°$.

- The pelvis translation also has not been investigated in the past. The standard deviation of the x-y-position corresponds to the error in directing the central beam towards the symphysis pubis. As the patient's legs give a hint where the median plane of the body is, the medio-lateral position of the symphysis is easier to find than the cranio-caudal one. Hence, the x-component of this error is estimated to be smaller than the y-component: $\sigma_{\delta T_x} = 20$mm and $\sigma_{\delta T_y} = 30$mm.

  The z-position of the pelvis changes at an alteration of the patient's corpulence and at a rotation. A part of the vertical displacement is absorbed by the mattress on the x-ray table. The remaining rotational z-translation could have been integrated in the analytical formulation of the bone–cup distance, but has been left out to limit the complexity. The error components resulting from the variable corpulence and the pelvis rotation are estimated to be 15 mm and 25 mm, respectively. Combining them yields a total standard deviation of the z-position of $\sigma_{\delta T_z} = \sqrt{15^2 + 25^2}$ mm $= 29$ mm.

- Under the assumption that the film–focus distance set at exposure is unknown, the extremal values 900 mm and 1300 of this distance reported in [Russe 1988, Krismer *et al.* 1995] are adopted. Taking these values as limits of a 95% interval, a standard devation of $\sigma_{\delta f} = \frac{200}{2}$mm $= 100$ mm results.

- The rather irrelevant standard devitation of the x-y-position of the film is estimated to be $\sigma_{\delta t_x} = \sigma_{\delta t_y} = 5$ mm.

- The error in locating the cup reference point was estimated to be 0.5 mm in [Nunn *et al.* 1989] as well as in [Sutherland *et al.* 1982]. Hence, for these manual methods $\sigma_{\delta c_x} = \sigma_{\delta c_y} = 0.5$mm is assumed. For the digital methods no statements concerning this error have been found. The only number found which defines the precision of the cup coordinates in [Dickob *et al.* 1994] is the pixel size at the digitisation of 0.2 mm. In EBRA, the pixel size plays a minor role because the cup reference point is determined by applying a least squares estimation. However, in the latter method the geometrical resolution is only 75 dpi according to personal communication, which corresponds to a pixel size of 0.34 mm. Supposing that the least squares estimation compensates for the lower resolution, the error of $\sigma_{\delta c_x} = \sigma_{\delta c_y} = 0.2$mm is assumed for both the digital methods.

- The reproducibility in measuring the distance between the teardrop figures is estimated to be 1.41 mm in [Nunn *et al.* 1989]. It is assumed that the x- and the y-coordinate have the same error to get an estimate of the precision in locating a single teardrop figure. Then, $\sigma_{\delta m_{k\,x,y}}$ can be obtained by division of the above value by $\sqrt{2}$. Another number is stated in [Sutherland *et al.* 1982]. There, the error in locating the teardrop figure as well as the Köhler line was found to be only 0.5 mm. Averaging the published errors yields $\sigma_{\delta m_{k\,x,y}} = \frac{(1.41\,\text{mm}/\sqrt{2} + 0.5\,\text{mm})}{2} = 0.75$ mm for

the manual methods [Nunn *et al.* 1989, Sutherland *et al.* 1982]. In [Dickob *et al.* 1994], the distance between the teardrop figures could be determined more precisely. An error of only 0.5 mm is stated. Division by $\sqrt{2}$ yields a standard deviation of $\sigma_{\delta m_{k\,x,y}} = 0.35$ mm for this digital method. The bony structures used in [Krismer *et al.* 1995], the foramina obturatoria, have sharper contours than the teardrop figures. As they are just defined by mouse-clicking, the pixel size now limits the precision and is taken as standard deviation in EBRA: $\sigma_{\delta m_{kx}} = \sigma_{\delta m_{ky}} = 0.34$ mm.

- For the standard deviation in measuring the diameter of the femoral head a value of 0.53 mm is given in [Nunn *et al.* 1989], which yields a standard deviation for the radius of 0.27 mm. In [Sutherland *et al.* 1982, page 973], "an error of ±0.25 millimeter in measurements of the femoral head" is stated. Supposing that the radius is measured in [Sutherland *et al.* 1982], the errors in the two publications are similar, and $\sigma_{\delta b} = 0.26$ mm is assumed for the traditional methods. Concerning [Dickob *et al.* 1994] and [Krismer *et al.* 1995], the above considerations for the cup reference point are adopted and $\sigma_{\delta b} = 0.20$ mm is taken. This is probably the lower limit of the error of b, because only the difference between the long and the short axis of the elliptic projection of the femoral head amounts already to 0.2 mm (see Sect. 2.4).

2.6.3 Error in Nunn *et al.* and in Dickob *et al.*

The standard deviation of the bone–cup distance is:

$$
\begin{aligned}
\sigma_{d_{\mathrm{ml}}}^2 &= (0.07218\sigma_{\delta\alpha})^2 + (0.01070\sigma_{\delta\beta})^2 + (-0.00360\sigma_{\delta\gamma})^2 + \\
&\quad (0.00342\sigma_{\delta T_x})^2 + (0.04954\sigma_{\delta T_z})^2 + (0.01230\sigma_{\delta f})^2 + \\
&\quad (0.74428\sigma_{\delta c_x})^2 + (-0.93775\sigma_{\delta m_{1x}})^2 + (-0.08146\sigma_{\delta m_{1y}})^2 + \\
&\quad (0.19347\sigma_{\delta m_{2x}})^2 + (0.08146\sigma_{\delta m_{2y}})^2 + (-1.78171\sigma_{\delta b})^2 \\
\sigma_{d_{\mathrm{cc}}}^2 &= (-0.04556\sigma_{\delta\alpha})^2 + (-0.00002\sigma_{\delta\beta})^2 + (-0.00342\sigma_{\delta T_y})^2 + \\
&\quad (-0.00001\sigma_{\delta T_z})^2 + (-0.00001\sigma_{\delta f})^2 + (-0.74428\sigma_{\delta c_y})^2 + \\
&\quad (0.93775\sigma_{\delta m_{1y}})^2 + (-0.19347\sigma_{\delta m_{2y}})^2 + (-0.75020\sigma_{\delta b})^2
\end{aligned}
$$

$$(2.12)$$

For both components the significance of pelvis rotations is rather small because of the short 3D distance between implant reference point and bony landmarks. Also translations along the x- and the y-axis have a little effect because $\mathbf{C}_{0_z}$ and $\mathbf{M}_{10_z}$ only differ slightly.

In contrast to the general expectations, the correction of the x-distance for rotation around the cranio-caudal axis deteriorates the measurement. The correction is a multiplication of the measured medio-lateral distance by the quotient $\frac{|\mathbf{m}_{20}-\mathbf{m}_{10}|}{|\mathbf{m}_2-\mathbf{m}_1|}$, where the numerator is constant. This quotient is supposed to reflect the cosine of the rotation angle $\delta\beta$ or the proportional change of d_{ml} at a rotation around the y-axis. That would be the case for parallel projections (great film–focus distance). In a standard x-ray system with $f = 900$ mm, however, the inter-teardrop distance is not proportional to $\cos(\delta\beta)$, but the projection of

the teardrop figures is also influenced by their z-coordinates changed by the rotation. Therefore, even if the pelvis rotation around the cranio-caudal axis was the only source of error, the correction for rotation would rather lead to a biased measurement than neutralize the influence of $\delta\beta$. Apart from that, the inter-teardrop distance $|\mathbf{m_2} - \mathbf{m_1}|$ depends on $\delta\alpha$, on δT_z, and on δf, because all these variables affect the z-position of the teardrop figures. Thus, omitting the correction for rotation would yield the partial derivatives $\frac{\partial d_{ml}}{\partial\delta\alpha} = 0.02337$ and $\frac{\partial d_{ml}}{\partial\delta T_z} = \frac{\partial d_{ml}}{\partial\delta f} = -0.00030$, which are much smaller then the coefficients in (2.12).

The increase of the variance by the correction for rotation becomes also clear by comparing the two components of the overall error of the migration measurement. After insertion of the values for σ_{v_i} in (2.12), computation of the root, and multiplication by $\sqrt{2}$, the standard deviation results to be 3.01 mm in medio-lateral and 1.21 mm in cranio-caudal direction if the migration is determined as recommended by [Nunn *et al.* 1989]. In [Dickob *et al.* 1994], it is reduced to $\sqrt{2} \cdot \sigma_{d_{ml}} = 2.80$ mm and $\sqrt{2} \cdot \sigma_{d_{cc}} = 0.63$ mm. The reason for the higher precision is that the error in locating the cup and the bony landmarks is smaller according to the findings in [Dickob *et al.* 1994].

2.6.4 Error in Sutherland *et al.*

Here, the most relevant error source is the rotation around the z-axis strongly affecting $\sigma_{d_{cc}}$:

$$
\begin{aligned}
\sigma_{d_{ml}}^2 &= (0.01579\sigma_{\delta\alpha})^2 + (-0.12875\sigma_{\delta\beta})^2 + (-0.01030\sigma_{\delta\gamma})^2 + \\
&\quad (0.00979\sigma_{\delta T_x})^2 + (0.00126\sigma_{\delta T_y})^2 + (-0.00070\sigma_{\delta T_z})^2 + \\
&\quad (-0.00070\sigma_{\delta f})^2 + (0.78436\sigma_{\delta c_x})^2 + (0.10073\sigma_{\delta c_y})^2 + \\
&\quad (-0.46531\sigma_{\delta m_{2x}})^2 + (-0.05976\sigma_{\delta m_{2y}})^2 + (-0.31910\sigma_{\delta m_{3x}})^2 + \\
&\quad (-0.04097\sigma_{\delta m_{3y}})^2 + (-1.82120\sigma_{\delta b})^2 \\
\sigma_{d_{cc}}^2 &= (-0.04432\sigma_{\delta\alpha})^2 + (0.00281\sigma_{\delta\beta})^2 + (-0.58410\sigma_{\delta\gamma})^2 + \\
&\quad (-0.00263\sigma_{\delta T_y})^2 + (-0.00001\sigma_{\delta T_z})^2 + (-0.00001\sigma_{\delta f})^2 + \\
&\quad (-0.79081\sigma_{\delta c_y})^2 + (0.79081\sigma_{\delta m_{1y}})^2 + (-0.79698\sigma_{\delta b})^2
\end{aligned}
\tag{2.13}
$$

The great value for $\frac{\partial d_{cc}}{\partial\delta\gamma}$ results from the fact that d_{cc} — as far as the description in [Sutherland *et al.* 1982] could be understood — is just given by the coordinate difference $c_y - m_{1y}$, and the rotation of the pelvis around the z-axis is neglected. According to the coefficients in (2.13), x-y-translations and out-of-plane rotations have little effect on d_{cc} as well as on d_{ml} because of the short z-distance of the cup reference point to the teardrop figure or to the anatomical points assumed to define the Köhler line. However, their real influence on d_{ml} may be greater, because the Köhler line is in fact the projection of a large cortical area parallel to the x-rays. At a orientation or position change of the pelvis, the region projected alters. This has an influence on the measured distance that is not predicted by the partial derivatives.

Supposing that this effect is included in the estimated error of 0.75 mm in locating the Köhler line, the final standard deviation of the migration in medio-lateral direction can be calculated inserting the σ_{v_i}. It results to be $\sqrt{2} \cdot \sigma_{d_{\mathrm{ml}}} = 1.20$ mm. The final standard deviation of the cranio-caudal component has the quite high value of $\sqrt{2} \cdot \sigma_{d_{\mathrm{cc}}} = 2.71$ mm because of the great influence of the rotation around the z-axis.

2.6.5 Error in EBRA

In [Krismer *et al.* 1995], the x-y- as well as the z-distances between the 3D cup reference point and the bone reference structures are greater than in the other methods. Therefore, the migration is more sensitive towards the rotation of the pelvis. Now also the y-translation plays a role because of the great z-distance between cup center and the caudal edges of the foramina obturatoria:

$$
\begin{aligned}
\sigma_{d_{\mathrm{ml}}}^2 &= (-0.00656\sigma_{\delta\alpha})^2 + (-0.24317\sigma_{\delta\beta})^2 + (-0.01057\sigma_{\delta\gamma})^2 + \\
&\quad (0.01004\sigma_{\delta T_x})^2 + (0.03701\sigma_{\delta T_z})^2 + (-0.00747\sigma_{\delta f})^2 + \\
&\quad (0.00126\sigma_{\delta t_x})^2 + (-0.79479\sigma_{\delta c_x})^2 + (0.22159\sigma_{\delta m_{1y}})^2 + \\
&\quad (-0.22159\sigma_{\delta m_{2y}})^2 + (0.79731\sigma_{\delta m_{3x}})^2 + (-0.00126\sigma_{\delta m_{4x}})^2 + \\
&\quad (1.83256\sigma_{\delta b})^2 \\
\sigma_{d_{\mathrm{cc}}}^2 &= (-0.38049\sigma_{\delta\alpha})^2 + (-0.03987\sigma_{\delta\beta})^2 + (-0.02064\sigma_{\delta T_y})^2 + \\
&\quad (-0.02277\sigma_{\delta T_z})^2 + (-0.00436\sigma_{\delta f})^2 + (-0.00051\sigma_{\delta t_y})^2 + \\
&\quad (-0.79516\sigma_{\delta c_y})^2 + (1.11081\sigma_{\delta m_{1y}})^2 + (-0.31668\sigma_{\delta m_{2y}})^2 + \\
&\quad (-0.00051\sigma_{\delta m_{4y}})^2 + (-1.13476\sigma_{\delta b})^2
\end{aligned}
$$

$$(2.14)$$

As the calculated value for the minimal film–focus distance fell short of the predefined limit, the fixed value $f^{\min} = 900$ mm had to be inserted in the formulas for $d_{\mathrm{ml}}^{\min}$ and $d_{\mathrm{cc}}^{\min}$ (see Sections 2.2.3 and 2.4.3). This corresponds to setting the ratio between film–focus and implant–focus distance to a constant independent from the radiograph. It is responsible for the high sensitivity of the measurement towards pelvis translation in z-direction and towards the variability of the film–focus distance. If both $f^{\max}$ and $f^{\min}$ were set to the values calculated using equation (2.8) and reflecting the actual magnification, δT_z and δf had the negligible partial derivatives of $\frac{\partial d_{\mathrm{ml}}}{\partial \delta T_z} = -0.00085$, $\frac{\partial d_{\mathrm{ml}}}{\partial \delta f} = -0.00045$, $\frac{\partial d_{\mathrm{cc}}}{\partial \delta T_z} = 0.00061$, and $\frac{\partial d_{\mathrm{cc}}}{\partial \delta f} = 0.00053$.

Moreover, this implicite assumption of a constant magnification still increases the high sensitivity towards the variable pelvis orientation. The partial derivatives with respect to the rotation angles would be (mainly) reduced to $\frac{\partial d_{\mathrm{ml}}}{\partial \delta\alpha} = -0.02105$, $\frac{\partial d_{\mathrm{ml}}}{\partial \delta\beta} = -0.17759$, $\frac{\partial d_{\mathrm{cc}}}{\partial \delta\alpha} = -0.36131$, and $\frac{\partial d_{\mathrm{cc}}}{\partial \delta\beta} = -0.00010$, if $f^{\max}$ as well as $f^{\min}$ were chosen according to the actual magnification. This effect can also be seen in [Nunn *et al.* 1989, Dickob *et al.* 1994], where the correction for magnification also decreases these derivatives. On the other hand, setting the ratio between film–focus and

implant–focus distance to a constant makes the measurement less sensitive towards the error in determining the radius of the femoral head. The partial derivative with respect to δb, which generally is approximately proportional to the size of the measured distance, is reduced by a factor 2. While in the other methods $\frac{\partial d_{\mathrm{ml,cc}}}{\partial \delta b}/d_{\mathrm{ml,cc}}$ is about $1/17$, here it is only about $1/34$.

The migration assessment proposed by [Krismer *et al.* 1995] is much more sensitive towards the rotation and translation of the pelvis than the one recommended by [Nunn *et al.* 1989, Dickob *et al.* 1994] or the method described in [Sutherland *et al.* 1982]. However, this sensitivity is for the most part compensated by sorting the radiographs according to the pelvis orientation and by the higher precision in locating the bony landmarks and the cup. Insertion of the entering errors in (2.14) yields for the standard deviation of the bone–cup distance $\sigma_{d_{\mathrm{ml}}} = 1.44\,\mathrm{mm}$ and $\sigma_{d_{\mathrm{cc}}} = 1.13\,\mathrm{mm}$. The final error of the migration assessed depends on the number, the exposure dates and the comparability of the follow-up studies' radiographs and is derived as described in the following.

The final error considering the comparability algorithm

In order to estimate the effect of the comparability algorithm, a follow-up study of four radiographs acquired at the times t_0, t_1, t_2, and t_3 after implantation was assumed. According to [Krismer *et al.* 1995], this is the minimum number to determine migration using EBRA. Additionally, it was assumed that the series contains two pairs of comparable radiographs, and that the time interval lying between the exposure dates of one pair overlaps with the time interval of the other one (see Fig. 2.6). Usually, the exposures are taken with growing time intervals. Based on the exposure dates in a migration study using EBRA [Krismer *et al.* 1996a], $t_0 = 1.5$ months, $t_1 = 3$ months, $t_2 = 12$ months, and $t_3 = 24$ months was chosen. [1]

In the following paragraphs, $\mathbf{d}_i = (d_{\mathrm{ml}_i}, d_{\mathrm{cc}_i})$ $(i = 0, ..., 3)$ denotes the bone–cup distance measured using the radiograph acquired at the time t_i. For all $\mathbf{d}_i$, $\sigma_{d_{\mathrm{ml}}}$ and $\sigma_{d_{\mathrm{cc}}}$ are assumed to be the same. Three cases of determining the migration are distinguished: a) only one pair of comparable radiographs is available; b) the migration during the time where the intervals of two pairs overlap supposed to be measured (here the time between t_1 and t_2); c) finding out the total migration of the follow-up series is intended.

In case a), the migration is simply the difference between the 2D distances in two radiographs, and its standard deviation is $\sqrt{2} \cdot (\sigma_{d_{\mathrm{ml}}}, \sigma_{d_{\mathrm{cc}}}) = (2.04\,\mathrm{mm}, 1.60\,\mathrm{mm})$. In case b), two values for the migration are measured using two pairs of comparable radiographs, and the mean is calculated. The mean migration $\overline{\mathbf{d}_2 - \mathbf{d}_1}$ between t_1 and t_2 is

$$\overline{\mathbf{d}_2 - \mathbf{d}_1} = \frac{1}{2}\left(\tfrac{t_2 - t_1}{t_2 - t_0}\left(\mathbf{d}_2 - \mathbf{d}_0\right) + \tfrac{t_2 - t_1}{t_3 - t_1}\left(\mathbf{d}_3 - \mathbf{d}_1\right) \right).$$

Applying the principle of error propagation to the above equation, the standard deviation of the migration between t_1 and t_2 is $\frac{1}{2}\sqrt{2 \cdot 0.86^2 + 2 \cdot 0.43^2} \cdot (\sigma_{d_{\mathrm{ml}}}, \sigma_{d_{\mathrm{cc}}}) = (0.98\,\mathrm{mm}, 0.77\,\mathrm{mm})$.

---

[1] The first radiograph made 3 days after implantation was neglected, as it often shows the pelvis in an extreme orientation because of pain. Thus, comparability with the other radiographs of the series usually can not be expected.
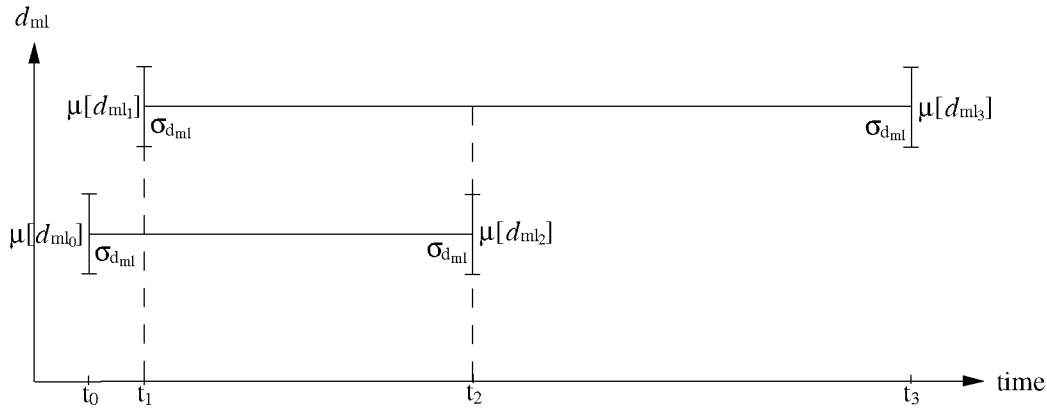
Figure 2.6: *Illustration of the comparability algorithm. Possible expectation values $\mu\,[d_{ml_i}]$ ($i = 0, ..., 3$) and the standard deviations $\sigma_{d_{ml}}$ of the medio-lateral distance in two comparable pairs of radiographs are shown. It is assumed that no migration has been occurred.*

In case c), the migration is determined by adding portions of the migration of the two comparable pairs. The migration $\mathbf{d}_3 - \mathbf{d}_0$ between t_0 and t_3 could be given by the following equation, for example:

$$\mathbf{d}_3 - \mathbf{d}_0 = \frac{0.5(t_2+t_1)-t_0}{t_2-t_0}\,(\mathbf{d}_2 - \mathbf{d}_0) + \frac{t_3-0.5(t_2+t_1)}{t_3-t_1}\,(\mathbf{d}_3 - \mathbf{d}_1)$$

Again applying the principle of error propagation, the standard deviation of the overall migration during the follow-up study is $\sqrt{2 \cdot 0.57^2 + 2 \cdot 0.79^2} \cdot (\sigma_{d_{ml}}, \sigma_{d_{cc}}) = (1.98\,\mathrm{mm}, 1.55\,\mathrm{mm})$.

2.7 Conclusions of the error analysis

According to the found standard deviations, the analysed methods of assessing cup displacement should be used only very carefully as a diagnostic tool after THR. A definition of loosening as total migration of greater than 1 mm within 2 years measured using EBRA [Stöckl *et al.* 1999], for example, does not seem to be reasonable regarding the just presented standard deviations of 1.98mm and 1.55mm for the cup displacement between the first exposure and the one after 24 months. However, the small error of 0.63 mm for the cranio-caudal displacement measured using the method of [Dickob *et al.* 1994] gives hope that in principle a precise migration assessment using standard radiographs is possible. The conditions for achieving optimal precision can be well defined on the results of the theoretical error analysis. They concern on the one hand the reduction of the sensitivity of the observed bone–cup distance towards the sources of errors and on the other the direct reduction of the magnitude of the entering errors. In the next paragraphs it is summarized how the former can be achieved. After having reduced the influence of the sources of error, the entering errors which still need to be taken into account are out-of-plane rotations of the pelvis and the error in locating the bone reference points and the cup.

Considering the significance of the variable orientation and position of the pelvis in the x-ray unit, in an improved method a bone reference with a short distance to the cup should be chosen. Especially the ventral-dorsal component of this 3D distance is relevant. Using a bone reference close to the implant strongly decreases the influence of out-of-plane rotations and of the variable horizontal position of the pelvis. On the other hand, a correction for these rotations by just comparing the varying distances between anatomical structures in the x-ray images should be avoided. An influence on the measurement of the rotation around the ventral-dorsal axis can be excluded using an image coordinate system defined by a line connecting two bony landmarks.

The bone–cup distance should be corrected for magnification estimating the ratio between film–focus and implant–focus distance in each radiograph. If predetermined values for this ratio are avoided the correction for magnification makes the measurement independent from the varying film–focus and pelvis–focus distance. Second, it can also decrease the sensitivity of the measured migration towards the variable orientation of the pelvis. As in the case of an adapted correction for magnification none of the intrinsic parameters affects the measured migration, a reconstruction of the spatial situation at exposure to minimize the influence of the variable film position is not necessary.

3

System developed for measuring the cup position in the bone

The goal is the observation of the displacement of the artificial hip socket with respect to the bone with a precision in the sub-millimeter range. The data sources given are 2–10 standard anterior-posterior x-ray images of the pelvis containing the cup and the CAD-model of the implant. The exact position of the radiographic film relative to the x-ray source, i.e. the intrinsic parameters, as well as the position and orientation of the pelvis bone and of the cup, i.e. the extrinsic parameters, are unknown. The orientation of the implant has to be considered seperately from the one of the bone, because the cup can not only migrate but also rotate within the bone. The model of the cup and its projection in the radiograph give information about the implant's 3D position and orientation at each exposure. For locating the bone, however, only 2D data are available (the premise is that no computer tomographs are acquired).

The first idea was to estimate the 3D translation and rotation of the pelvis bone between two x-ray images using the so-called 8-point algorithm first described in [Longuet-Higgins 1981]. This algorithm is based on an equation which connects points of an arbitrary object in a reference image with the projections of these points in a comparison image made by a moving camera. It can be applied to radiographs by assuming that the object or the patient moves, instead of the camera or the film–focus system. The necessary intrinsic parameters could be gained by a seperate calibration of the x-ray system. By formulating the basic equation for at least 8 landmarks an equation system is defined, which can be solved with respect to the translational and rotational parameters. This approach theoretically provides a solution of the problem of finding the bone's 3D motion parameters having only 2D data. However, the 8-point algorithm is very sensitive towards errors in the coordinates of the image points.

This is especially true in evaluating anterior-posterior pelvis radiographs, because the extrinsic parameters only change little, and the focus–object distance is long which implies small angles between the rays reaching from the focus to the image points. Experiments were made solving the equation system using 16 landmarks of all the different pelvis bone parts and slightly perturbing the coordinates of each point in the comparison image one after the other. The result was that the precision in locating the coordinates must be in

the order of magnitude of $\pm 0.01\,\text{mm}$ to obtain a deviation of the estimated translation parameters of less than $\pm 1\,mm$. It is not clear if there are at all stable 3D points in the bone, as the shape of the pelvis may change in time. Apart from that, the identification of real 3D points in x-ray images is very difficult, as the image structures are formed by superposition of all object points along the rays. Therefore, finding 16 natural landmarks which can be located with a precision of $0.01\,\text{mm}$ was not possible. A standard deviation of the translation parameters in the sub-millimeter range was found in leave-one-out experiments only if using as landmarks 20 iron balls which were implanted all over the pelvis. As the implantation of markers spread over the whole pelvis is surgically not realizable, the precise estimation of the 3D parameters of the bone can not be performed under clinically feasible conditions.

Due to the lack of a truly three-dimensional solution we concentrated on the development of a precise 2D measurement method. Like in the methods described in the introduction, the migration of the artificial hip socket was defined as the change of the cup position relative to the bone observed in the radiographs of the THR's follow-up study. One of these radiographs, generally an early postoperative one, is chosen to be the reference image, while the remaining ones are the comparison images. The measurement of the bone–cup distance representing the relative cup position was optimized by taking into account the findings of the error analysis (Chapter 2). The bone–cup distance was defined by reducing the influence of the entering errors as far as possible. At the same time, the reference points were chosen under consideration of their stability at pelvis movements. Apart from this geometrical optimization, methods were developed for precisely determining the image positions of these points. The variability in locating the bony landmarks was reduced by applying a semi-automated template matching algorithm: The user defines the template, which is an area in the reference image containing a bony feature. He gives an initial estimate by marking the landmark, i.e. a certain point of the feature, in the reference and in the comparison radiograph. Then, he starts the matching algorithm, which estimates precisely the relative landmark position, that means the 2D translation of the bony feature between the two images. Concerning the implant, a full 3D analysis of each radiograph was achieved by implementing the principle of Analysis-by-Synthesis: A synthetic x-ray projection of the cup is generated using its CAD-model, an initial estimate of its absolute position and orientation defined by the user, and the approximate intrinsic parameters. The exact 3D parameters of the cup are found automatically by matching its synthetic projection to the original one in the reference or in the comparison radiograph.

Thus, the XIMIT (X-ray evaluation using Implant Models and Image Templates) system for the assessment of cup displacement was worked out. A comparability algorithm, such as the one in EBRA, has not yet been considered, because it requires clinical experience in applying the system. In the following section, it is described how the bone–cup distance is defined. In the subsequent section, the user interface of the system is presented, which has been written using the IDL programming environment [Fanning 1999]. The algorithms for locating the bony landmarks and the cup are described in the Chapters 4 and 5, respectively.

3.1 Geometrical definition of the bone–cup distance

To reasonably define the measured bone–cup distance, the following points based on the theoretical error analysis in the previous chapter have been considered:

1. The distance is represented in a 2D coordinate system fixed to pelvic points in the image to exclude the impact of a pelvis rotation between two exposures around the ventral-dorsal axis.

2. The distance measured in the image is corrected for magnification to avoid a dependency of the measurement from the focus–film and the focus–pelvis distance.

3. The influence of out-of-plane rotation and pelvis translation parallel to the film plane is reduced by the choice of the reference points under consideration of their 3D positions and –as far as possible– their robustness at pelvis motions.

The realization of the first two points is discussed in Sect. 3.1.1, where a general formulation for the bone–implant distance is worked out. In Sect. 3.1.2, the choice of the reference points is described in detail.

3.1.1 General expression for the bone–cup distance

An image coordinate system fixed to the pelvis is defined using the vector connecting two bony image structures $\mathbf{m}_1$ and $\mathbf{m}_2$ symmetrical to the medio-lateral axis. The axes of this system are given by the direction $\mathbf{e}_{ml}$ (ml for medio-lateral) of this vector and by its normed perpendicular $\mathbf{e}_{cc}$ (cc for cranio-caudal). As bone reference additional landmarks $\mathbf{m}_{3,4}$ are used. The bone–implant distance in medio-lateral- and in cranio-caudal-direction is defined as the dot product of $\mathbf{e}_{ml}$ and $\mathbf{e}_{cc}$ with the vector reaching from the bony landmarks $\mathbf{m}_3$ and $\mathbf{m}_4$ to the cup reference point $\mathbf{c}$, respectively (see Fig. 3.1). The components of the distance are corrected for magnification through division by the magnification factor g. This factor is approximated by the quotient between the film–focus distance and the z-coordinate of the cup and estimated as described in Chapter 5. Independently from the positions of the cup reference point and of the bony landmarks, the measured bone–implant distance is expressed by the formula

$$\mathbf{d} = \frac{1}{g}\begin{pmatrix}(\mathbf{c}-\mathbf{m}_3)^{\mathrm{T}}\cdot\mathbf{e}_{ml}\\(\mathbf{c}-\mathbf{m}_4)^{\mathrm{T}}\cdot\mathbf{e}_{cc}\end{pmatrix} = \frac{1}{g}\begin{pmatrix}(\mathbf{c}-\mathbf{m}_3)^{\mathrm{T}}\cdot\frac{(\mathbf{m}_2-\mathbf{m}_1)}{|\mathbf{m}_2-\mathbf{m}_1|}\\(\mathbf{c}-\mathbf{m}_4)^{\mathrm{T}}\cdot\begin{pmatrix}0 & -1\\1 & 0\end{pmatrix}\frac{(\mathbf{m}_2-\mathbf{m}_1)}{|\mathbf{m}_2-\mathbf{m}_1|}\end{pmatrix}. \tag{3.1}$$

3.1.2 Choice of the reference points

The cup reference point was chosen be the projection of the 3D center $\mathbf{C}$ of the cup's opening plane. This cup point is the one whose projection is least affected by a 3D rotation
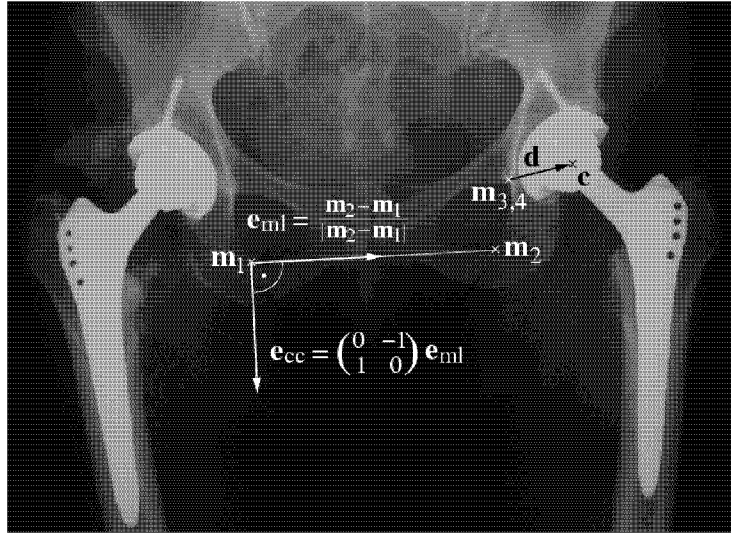
Figure 3.1: *The measured bone–cup distance in XIMIT.*

of the implant. For the optimal choice of the bony landmarks, the qualitative instructions of the previous chapter (Sect. 2.7) were specified. The dependency of the standard deviations $\sigma_{d_{ml}}$ and $\sigma_{d_{cc}}$ of the measured distance from the 3D positions $\mathbf{M}_{10,20,30,40}$ of the landmarks was investigated numerically. The standard deviations were determined theoretically according to the scheme described in Chapter 2 and by inserting varying values for the landmarks' 3D coordinates. The expressions for $\mathbf{c}$ and $\mathbf{m}_k$ as given by (2.2) and (2.3) were inserted in (3.1). The factor g in (3.1) was replaced by $\frac{f+\delta f}{C_z+\delta f} + \delta g$, where δg is the deviation of the magnification factor estimated from the expectation value.

The calculation of $\sigma_{d_{ml}}$ and $\sigma_{d_{cc}}$ requires the standard deviations σ_{v_i} of the variables representing the sources of error. During the test, they were set to the ones assumed for the method of [Dickob *et al.* 1994] and listed in Sect. 2.6.2. In order to estimate the standard deviation of δg, which had not been required before, the magnification was in this context supposed to be approximated like in the previous methods, by the quotient between the measured radius of the femoral head in the radiograph and its real radius. The error $\sigma_{\delta g}$ was set to the standard deviation of this quotient. It was attained by dividing the listed error in measuring the radius of 0.2 mm by $r = 14$ mm.

First, the distances of $\mathbf{M}_{30}$ and $\mathbf{M}_{40}$ to the 3D cup reference point were increased in all directions. While doing so, $f = 1100$ mm was assumed and the cup reference point of Tab. 2.1 was taken yielding $\mathbf{C}_0 = (98.0$ mm, -18.3 mm, 870 mm$)$. The coordinates of the landmarks defining the image system were set to $\mathbf{M}_{10} = (-C_{0_x}, C_{0_y}, C_{0_z})$ and to $\mathbf{M}_{20} = \mathbf{C}_0$. The error components $\sigma_{d_{ml}}$ and $\sigma_{d_{cc}}$ are plotted subject to the position of $\mathbf{M}_{30}$ and of $\mathbf{M}_{40}$ in the Figures 3.2a–c and 3.3a–c, respectively. The plots have their minimium if $\mathbf{M}_{30}$ and $\mathbf{M}_{40}$ are equal to $\mathbf{C}_0$. They confirm the observation of Chapter 2 that the distance in z-direction between the bony landmarks and the cup reference point mostly influences the precision. Therefore, it is very important to choose for $\mathbf{M}_{30}$ and $\mathbf{M}_{40}$ bony landmarks with

the same height above the film plane as $\mathbf{C}_0$. What can additionally be seen, is that $\sigma_{d_{\mathrm{ml}}}$ is a bit less affected by the z-distance, but depends also on the y-distance between bony landmark and cup-reference point. Whereas the standard deviation of the cranio-caudal component is completely independent from the x-coordinate of $\mathbf{M}_{40}$.

The teardrop figure is the projection of a bony area which has a mean z-distance to the cup reference point of less than 10 mm according to the normal anatomy. The lateral branch of this figure is formed by the acetabular fossa located in the medial area of the acetabulum, its caudal bow by the acetabular notch, and its medial branch by a part of the inner pelvic cortex [Kölbel and Golzo 1977, Peic 1971]. Despite the fact that pelvis motions affect the appearance of the teardrop figure, its most caudal point is chosen to be the landmark $\mathbf{M}_{30}$ as well as the landmark $\mathbf{M}_{40}$. All bony features less sensitive to the pelvic position and orientation unfortunately have a greater x-, y- and especially z-distance to $\mathbf{C}_0$. They would methodically imply higher values for $\sigma_{d_{\mathrm{ml}}}$ and $\sigma_{d_{\mathrm{cc}}}$ and hence do not provide a better alternative. If the pelvis is only slightly rotated and translated between two radiographs, the teardrop figure allows for a precision which can not be achieved with any other bony landmark. If the pelvis position and orientation is changed significantly so that the most caudal point of the teardrop figure can not be identified, the use of landmarks which still can be located precisely is also not recommendable. Their great distance to the cup would lead to a great deviation in d_{ml} and in d_{cc}. Another advantage of this figure is that its cranio-caudal distance to the cup reference point (about 10 mm) is shorter than the medio-lateral one (about 30 mm). Using the same landmark for $\mathbf{M}_{30}$ and for $\mathbf{M}_{40}$ this reduces the total error, as the y-distance was found to be relevant for $\sigma_{d_{\mathrm{cc}}}$ as well as for $\sigma_{d_{\mathrm{ml}}}$.

The findings of the previous paragraph confirm the practical and experimental experiences of several investigators who explicitly recommended the use of the teardrop figure as bone reference [Massin *et al.* 1989, Goodman *et al.* 1988, Brand *et al.* 1986]. Also the results of the validation experiments in Sect. 7.3 show that the use of this bony feature makes a precise migration assessment possible. Unfortunately, it does not provide the most universal solution. Apart from the fact that the appearance of this bony structure depends on the pelvis position and orientation, it also strongly differs from hip to hip. Sometimes no structure at all is visible. In the latter cases, the cranial edge of the foramen obturatum may be used alternatively as bony landmark for the cranio-caudal cup displacement. The optimal solution would be the implantation of an external marker (a small metal sphere). For the geometrical reasons explained above it should be positioned in the bony area forming the teardrop figure.

Having chosen the landmarks $\mathbf{M}_{30}$ (= $\mathbf{M}_{40}$), the position of the ones defining the image coordinate system were investigated. The points $\mathbf{M}_{10}$ and symmetrically $\mathbf{M}_{20}$ were varied setting $\mathbf{M}_{30}$ to the most caudal point of the teardrop figure, which was assumed to have the coordinates (64.7mm, −4.2mm, 872.3mm) taken from Tab. 2.1. As can be seen in the Figures 3.4a–c, the positions of these landmarks can be neglected as long as their x-distance to the cup does not exceed about 80 mm, that means they should not lie closer than 20 mm to the median plane. Thus, for $\mathbf{M}_{10,20}$ the most caudal image points of the foramina obturatoria were chosen (see Fig. 3.1). These are bony structures with a relatively great

a   b   c

Figure 3.2: *The error of the medio-lateral component of the measured bone–cup distance subject to the distance of the bony landmark* **M**$_{30}$ *to the cup reference point in x-y- (a), in x-z- (b), and in y-z-direction (c).*
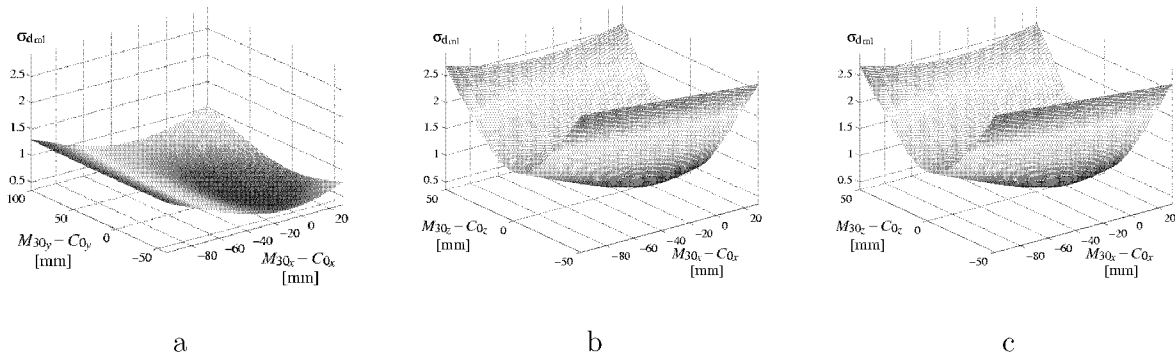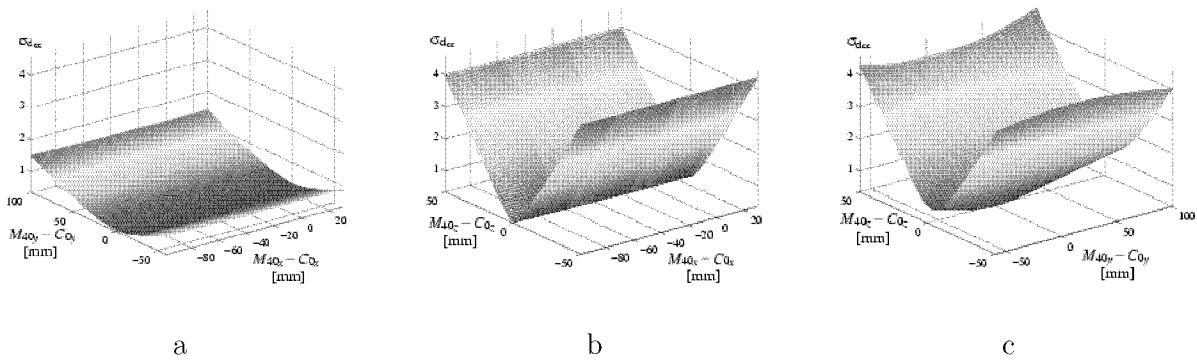

a   b   c

Figure 3.3: *The error of the cranio-caudal component of the measured bone–cup distance subject to the distance of the bony landmark* **M**$_{40}$ *to the cup reference point in x-y- (a), in x-z- (b), and in y-z-direction (c).*

a   b   c
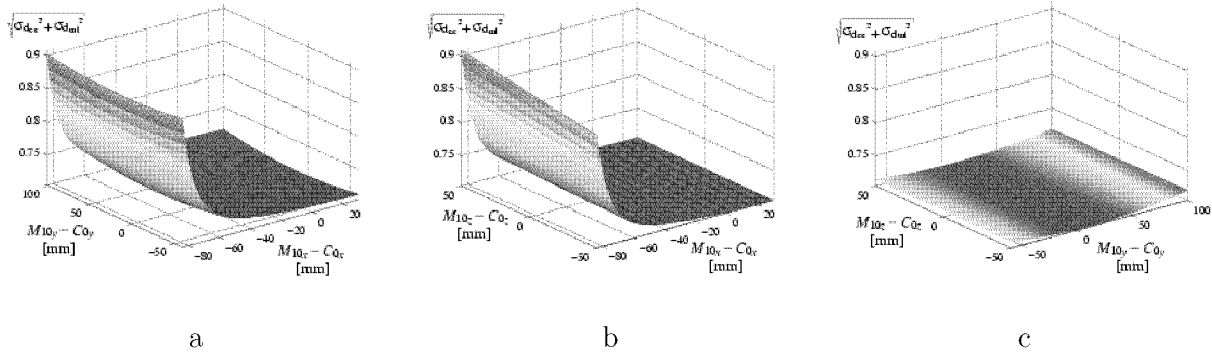
Figure 3.4: *The magnitude $\sqrt{\sigma_{d_{\mathrm{ml}}}^2 + \sigma_{d_{\mathrm{cc}}}^2}$ of the error of the measured bone–cup distance subject to the x-y- (a), the x-z- (b), and the y-z-position (c) of the bony landmarks $\mathbf{M}_{10}$ and $\mathbf{M}_{20}$. The coordinates of the first landmark are the same as the plotted ones of the latter, exept for the x-coordinate: $M_{10_x} = -M_{20_x}$.*

distance to the cup but with a stable appearance in the radiograph even at out-of-plane rotations of the pelvis. They can be located in the image reliably.

3.2 User interface for evaluating the radiographs

In Fig. 3.5, the graphical user interface is shown. Having loaded the reference x-ray image and the current comparison image, they are downsized and displayed in the upper and in the lower left window, respectively. The areas containing the cup and the bony landmarks are chosen by mouse-clicking in the left windows. They are indicated on left by coloured squares and shown enlarged on the right, where correspondingly the upper window belongs to the reference and the lower to the comparison radiograph.

The system is operated in two different modes: the "Bone Mode" (Fig. 3.5a) and the "Cup Mode" (Fig. 3.5b). In the former, the area of a bony landmark in the comparison radiograph is matched to the template, which is defined by the user in the enlarged cut of the reference image using the mouse (see upper square window in Fig. 3.5a). The user provides the initial estimate by clicking on the landmarks in the reference and in the comparison radiograph (see small points in the square windows in Fig. 3.5a). The matching algorithm can then estimate the precise position of the landmark in the latter image. This procedure is applied to all bony landmarks sequentially. The points in reference image only need to be defined once, because they must stay the same for all the comparison radiographs of the series.

In the "Cup Mode", the cup is located individually in each image. The user gives an initial estimate by fitting the projection of a 3D circle to the contours of the opening plane. With the initial parameters, the x-ray image is synthesized (see right small window in Fig. 3.5b) and a region of interest is calculated automatically (see upper square window). Clicking on "Do Anasyn" the Analysis-by-Synthesis algorithm is started. For a control of the result,

a
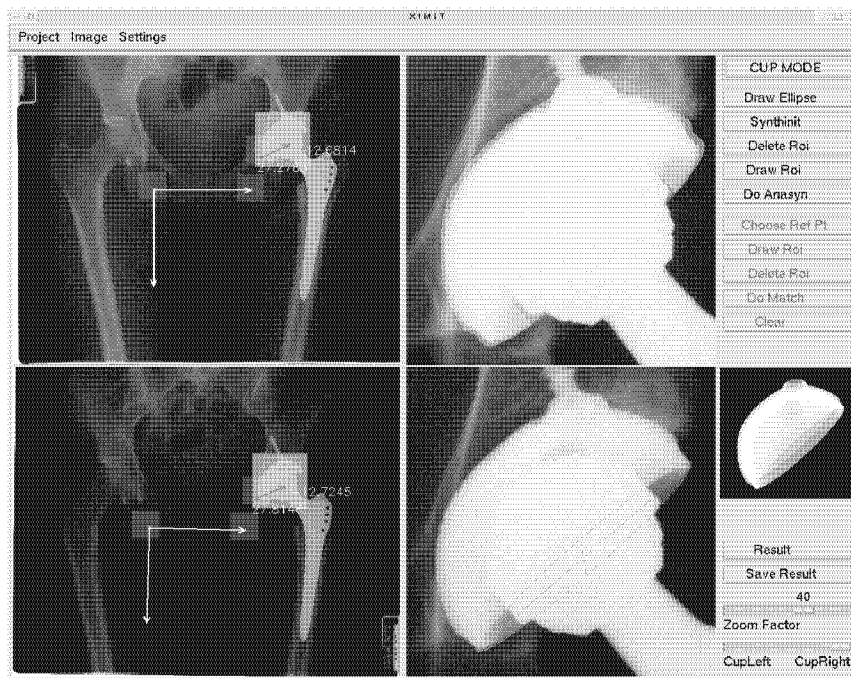
b

Figure 3.5: *The graphical user interface of XIMIT run in the "Bone Mode" (a) and in the "Cup Mode" (b) version.*

the image of the gray-value differences between original projection and the one synthesized using the final cup parameters is displayed.

Having located the required reference points the bone-cup distance is calculated and displayed on the left (Fig. 3.5b).

4

Locating the bony landmarks

The error in locating the reference points in the x-ray image is very important for the 2D migration assessment according to the general expectations as well as to the findings of the theoretical error analysis. Its influence on the measured bone–cup distance can hardly be compensated, in contrast to the other entering errors which play a minor role after the careful geometrical definition of this distance (Chapter 3). For this reason the alternative way consisting in locating the bony landmarks and the cup as precisely as possible had to be chosen. The position determination of the cup is facilitated by its known 3D shape, whereas for the bone neither specific 3D data nor generic image models are available. Therefore, the bony landmarks are located using only the x-ray image information of the individual pelvis. Bony features in the reference image are used as templates. The corresponding features in the other radiographs of the follow-up series are compared with these models by applying an existing template matching algorithm.

Template matching is a general procedure for estimating the mapping between a template, i.e. a structured area in a reference image, and a patch, i.e. the corresponding area in a search or comparison image. Here, least squares matching (LSM) is used: The mapping parameters are found through the application of the least squares formalism as described, for example, in [Mikhail 1976, Koch 1988]. The advantage of LSM is its high precision not limited by the pixel resolution. Additionally, it ideally provides the possibility to estimate the variance and the determinability of the found parameters. LSM was first proposed by [Grün 1985] for the precise localization of control points in aerial photogrammetry. It was used by [Danuser and Mazza 1996] to observe transformations in the nanometer range in microscopic images. The LSM implementation used here was actually written in order to accurately position patients in the radiotherapy treatment device by evaluating portal images, which are high energetic x-ray images [Berger and Gerig 1998, Berger 1999].

In the following sections, an outline of LSM is given. For details the reader is referred to [Berger 1999]. The underlying model and the objective function of the parameter estimation are presented in Sect. 4.1. In Sect. 4.2, the (analytical) solution of the least squares minimization problem is shortly described. The use of least squares matching for locating the bony landmarks in the pelvic radiographs is discussed in Sect. 4.3.

4.1 Model and objective function

The mapping between the gray value distribution of the template and the one of the patch is modeled by a geometric transformation in the patch's space and a global adjustment of the patch's intensity range. The model is expressed by

$$I^{\text{templ}}(\mathbf{p}_i) = \tau^{\text{lsm}} + \lambda^{\text{lsm}} \cdot I^{\text{patch}} \left(\mathbf{p}'_i(\mathbf{p}_i, \mathbf{h}) \right) \ , \tag{4.1}$$

where $I^{\text{templ}}(\mathbf{p}_i)$ is the gray value at the center $\mathbf{p}_i$ of the ith pixel ($i = 1, ..., n$) in the template, $I^{\text{patch}}(\mathbf{p}'_i(\mathbf{p}_i, \mathbf{h}))$ the one at the position $\mathbf{p}'_i$ in the patch, and $\mathbf{h}$ is the vector containing the geometric parameters. The parameters of the radiometric adjustment are indicated with λ^{lsm} and τ^{lsm}. They are chosen so that the mean and the standard deviation of the template's gray values and of the ones of the patch are the same.

In the used LSM implementation, the geometric transformation is assumed to be generally affine:

$$\mathbf{p}'_i = \left(\begin{array}{cc} m_x^{\text{lsm}} & s_x^{\text{lsm}} \\ s_y^{\text{lsm}} & m_y^{\text{lsm}} \end{array} \right) \mathbf{p}_i + \left(\begin{array}{c} t_x^{\text{lsm}} \\ t_y^{\text{lsm}} \end{array} \right)$$

The parameter vector hence is $\mathbf{h} = (m_x^{\text{lsm}}, m_y^{\text{lsm}}, s_x^{\text{lsm}}, s_y^{\text{lsm}}, t_x^{\text{lsm}}, t_y^{\text{lsm}})^{\text{T}}$, where $m_{x,y}^{\text{lsm}}$, $s_{x,y}^{\text{lsm}}$, and $t_{x,y}^{\text{lsm}}$ stand for magnification, shear, and translation, respectively. The patch's gray values at $\mathbf{p}'_i$ are not lying on a grid any more. They are estimated by bilinear interpolation. Interpreting (4.1) according to the least square formalism, the residual

$$e_i = \tau^{\text{lsm}} + \lambda^{\text{lsm}} \cdot I^{\text{patch}} \left(\mathbf{p}'_i(\mathbf{p}_i, \mathbf{h}) \right) - I^{\text{templ}}(\mathbf{p}_i) \tag{4.2}$$

of each of the n template pixels can be calculated. As both I^{templ} and I^{patch} are observations, actually two residuals enter in this expression. Accordingly, e_i is identified with the residual of a combined observation (a detailed description of this interpretation can be found in [Berger 1999, page 25]). The equations (4.2) define together with the $n \times n$ weight matrix $\mathbf{P}$ the least square objective function $\mathbf{e}^{\text{T}}\mathbf{P}\mathbf{e}$, $\mathbf{e} = (e_1, ..., e_n)^{\text{T}}$. The weight matrix is the inverse of the cofactor matrix of the combined observations. As the covariances of the gray values can hardly be estimated, it is assumed that the $I^{\text{patch}}(\mathbf{p}'_i(\mathbf{p}_i, \mathbf{h}))$ and the $I^{\text{templ}}(\mathbf{p}_i)$ are uncorrelated and have constant variances. Then, the cofactor matrix is diagonal and the weight matrix can be written as

$$\mathbf{P} = \sigma_0^2 \cdot \mathbf{I} \ ,$$

where $\mathbf{I}$ is the identity matrix. The factor σ_0^2 is the reference variance. It does not influence the parameter estimation and is set to 1 for simplicity.

Sometimes, for example in this work, it is necessary to choose a geometrical transformation with a lower degree of freedom than the general affine mapping. This is realized by formulating constraints for the parameters. The constraints are interpreted as pseudo observation equations. In case of a translation, they are

$$m_x^{\text{lsm}} = m_y^{\text{lsm}} = 1 \ , \qquad s_x^{\text{lsm}} = s_y^{\text{lsm}} = 0 \ .$$

A similarity transformation is described by

$$m_x^{\mathrm{lsm}} = m_y^{\mathrm{lsm}} \ , \qquad s_x^{\mathrm{lsm}} = -s_y^{\mathrm{lsm}} \ . \tag{4.3}$$

To obtain a congruent transformation the condition

$$m_x^{\mathrm{lsm}\,2} + s_x^{\mathrm{lsm}\,2} = 1$$

is added to the similarity constraints (4.3). The constraint observation equations give additional residuals e_m, e_s, e_c, etc. In case of the congruent transformation they are, for example,

$$
\begin{aligned}
e_m &= m_x^{\mathrm{lsm}} - m_y^{\mathrm{lsm}} \\
e_s &= s_x^{\mathrm{lsm}} + s_y^{\mathrm{lsm}} \\
e_c &= 1 - m_x^{\mathrm{lsm}\,2} - s_x^{\mathrm{lsm}\,2} \ .
\end{aligned}
$$

The constraint residuals are included in the objective function. The residual vector is enlarged to $\mathbf{e}_{\mathrm{tot}} = (e_1, ..., e_n, e_m, e_s, e_c, ...)^{\mathrm{T}}$ and the weight matrix to

$$\mathbf{P}_{\mathrm{tot}} = \begin{bmatrix} \mathbf{P} & 0 \\ 0 & \mathbf{P}_{\mathrm{con}} \end{bmatrix} \ .$$

The diagonal $r \times r$ matrix $\mathbf{P}_{\mathrm{con}}$ (r indicates the number of constraint equations) contains large weights, which define how accurate the constraints are kept. They should be about the factor 10^3 greater than σ_0 to garantuee for a high accuracy. Including the constraints, the least squares goal function is $\mathbf{e}_{\mathrm{tot}}^{\mathrm{T}}\mathbf{P}_{\mathrm{tot}}\mathbf{e}_{\mathrm{tot}}$.

4.2   Minimization

The objective function is minimized iteratively using a Gauss-Newton scheme. The variables of the minimization are the parameters of the geometric transformation. The radiometric parameters are determined independently before each iteration step. A simultaneous estimation of both parameter sets would lead to an ill-conditioned system. Local ambiguities of the mapping between reference and comparison image would arise. An edge in the image, for example, can be slightly shifted by a radiometric transformation as well as by a translation.

The observation equations are linearized to solve the minimization problem analytically. Indicating with $\mathbf{I}^{\mathrm{templ}}$ the vector of the template gray values and with $\mathbf{I}^{\mathrm{patch}}(\tilde{\mathbf{h}})$ the one of the interpolated patch gray values at the current parameter estimate $\tilde{\mathbf{h}} = (\tilde{m}_x^{\mathrm{lsm}}, \tilde{m}_y^{\mathrm{lsm}}, \tilde{s}_x^{\mathrm{lsm}}, \tilde{s}_y^{\mathrm{lsm}}, \tilde{t}_x^{\mathrm{lsm}}, \tilde{t}_y^{\mathrm{lsm}})^{\mathrm{T}}$, the linearization of (4.2) in terms of $\mathbf{h}$ yields:

$$\mathbf{e} = \tau^{\mathrm{lsm}} + \lambda^{\mathrm{lsm}} \cdot \mathbf{I}^{\mathrm{patch}}(\tilde{\mathbf{h}}) - \mathbf{I}^{\mathrm{templ}} + \mathbf{A} \cdot \Delta\mathbf{h} \tag{4.4}$$

The Jacobian matrix $\mathbf{A}$ contains the partial derivatives of (4.2) with respect to the geometric parameters, and $\Delta\mathbf{h}$ indicates the update of the parameter vector. The calculation

of the Jacobian requires the spatial derivatives of the patch. They are estimated using a finite difference approximation. As these derivatives are very sensitive towards noise, the comparison as well as the reference image, for symmetry, are Gaussian filtered before each iteration step (in this work, a sigma of 2 pixels was chosen). In [Berger 1999, page 105–108], it is shown that this noise reduction generally lowers the variances of the estimated parameters.

The linearization of the constraint equations gives the additional set

$$
\begin{aligned}
e_m &= \tilde{m}_x^{\text{lsm}} - \tilde{m}_y^{\text{lsm}} + \mathbf{A_m} \cdot \Delta \mathbf{h} \\
e_s &= \tilde{s}_x^{\text{lsm}} + \tilde{s}_y^{\text{lsm}} + \mathbf{A_s} \cdot \Delta \mathbf{h} \\
e_c &= 1 - \tilde{m}_x^{\text{lsm}2} - \tilde{s}_x^{\text{lsm}2} + \mathbf{A_c} \cdot \Delta \mathbf{h} \ .
\end{aligned}
\tag{4.5}
$$

The matrix $\mathbf{A}$ is augmented by the vectors $\mathbf{A}_m$, $\mathbf{A}_s$, $\mathbf{A}_c$,... containing the partial derivatives of the constraint equations with respect to the parameters:

$$
\mathbf{A}_{\text{tot}} = \begin{bmatrix} \mathbf{A} \\ \mathbf{A}_m \\ \mathbf{A}_s \\ \mathbf{A}_c \end{bmatrix}
$$

The linear problem defined by (4.4) and (4.5) is solved by setting the first derivative of the objective function $\mathbf{e}_{\text{tot}}^{\text{T}} \mathbf{P}_{\text{tot}} \mathbf{e}_{\text{tot}}$ to zero. Thus, the normal equation system

$$
\mathbf{A}_{\text{tot}}^{\text{T}} \mathbf{P}_{\text{tot}} \mathbf{A}_{\text{tot}} \Delta \mathbf{h} = -\mathbf{A}_{\text{tot}}^{\text{T}} \mathbf{P}_{\text{tot}} \begin{pmatrix} \tau^{\text{lsm}} + \lambda^{\text{lsm}} \cdot \mathbf{I}^{\text{patch}}(\tilde{\mathbf{h}}) - \mathbf{I}^{\text{templ}} \\ \tilde{m}_x^{\text{lsm}} - \tilde{m}_y^{\text{lsm}} \\ \tilde{s}_x^{\text{lsm}} + \tilde{s}_y^{\text{lsm}} \\ 1 - \tilde{m}_x^{\text{lsm}2} - \tilde{s}_x^{\text{lsm}2} \end{pmatrix}
$$

is obtained. This system is solved for $\Delta \mathbf{h}$ by applying the Cholesky decomposition. After each iteration step, it is recomputed using the updated set of parameters $\tilde{\mathbf{h}} + \Delta \mathbf{h}$. When $\Delta \mathbf{h}$ falls short of a specified numerical resolution, the minimization procedure is finished.

4.3   Matching the bony structures

In the reference as well as in the comparison radiograph, the user marks by mouse-clicking the approximate landmarks, which are the lateral-caudal corners of the foramina obturatoria and the most caudal point of the teardrop figure next to the implant (see small points in the Figures 4.1a–c). This defines $\mathbf{m}_{1,2,3}$ for the reference radiograph and the inital estimate of $t_{x,y}^{\text{lsm}}$, which is given by the difference of the coordinates marked in the comparison to the ones in the reference image. The other parameters are set initially to $m_{x,y}^{\text{lsm}} = 1$ and $s_{x,y}^{\text{lsm}} = 0$ in the present version of XIMIT. The initial estimate has a negligible influence on the final result compared to the definition of the template (see Sect 4.3.1), which can strongly influence the matching. Which points of the bony structures in the reference image are

a   b   c
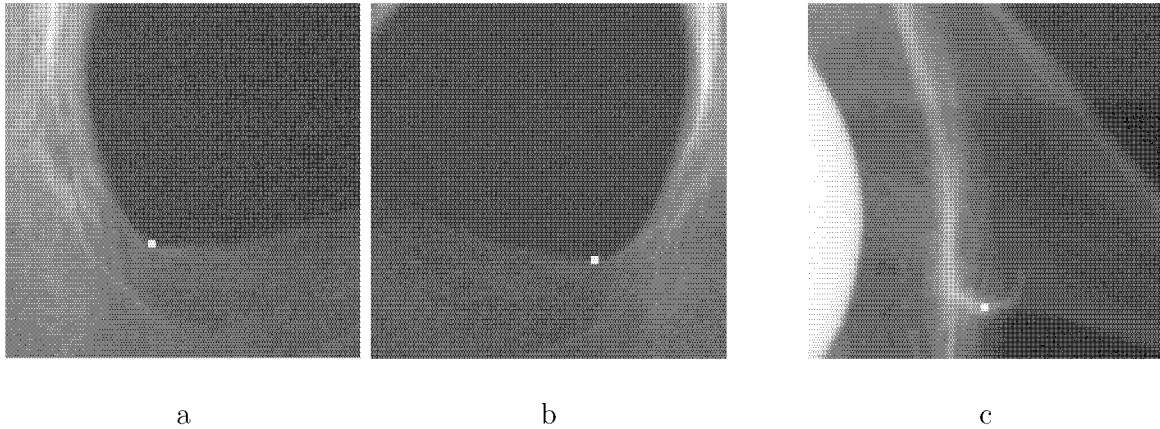
Figure 4.1: *The Figures a, b, and c show landmarks* $\mathbf{m}_1$, $\mathbf{m}_2$, *and* $\mathbf{m}_3$ *defined by the user in the reference image.*

taken as landmarks is also irrelevant. It is only important that they remain the same for the evaluation of the whole series if they are once defined. Adding the final translation $t_{x,y}^{\mathrm{lsm}}$ to these points yields the landmark coordinates in the comparison image.

Concerning the choice of the geometric parameters, the formation of the x-ray image has to be considered. The intensity distribution depends on the bony structures' attenuation coefficients superposed along the x-rays. At a rotation and at a translation of the pelvis, each ray passes a different set of structures and the image is altered. Actually, this alteration can only be modeled correctly considering the 3D shape and the local attenuation of the bone. Still, the first idea was to approximate it by an affine transformation in the patch's space. It was based on the assumption that the templates behave similarly to projected planar 3D structures. The image transformation of these planar structures at a 3D motion, which is in fact a homographic transformation, could be approximated in the pelvis radiographs by an affine mapping, because the focus–object distance is large compared to the size of the bony structures forming the templates. Unfortunately, it was found that this assumption does not hold. Neither for the teardrop figure nor for the foramina obturatoria LSM is robust at such a high degree of freedom for the mapping. Restriction by a congruent transformation was also tried, hoping to be able to model at least the rotation of the pelvis around the z-axis (in-plane rotation). However, even then the template had to be chosen very carefully to avoid a mismatch.

Finally, what was found to work best was the estimation of only the translational parameters. As the matched areas are small, a rather slight influence of the in-plane rotation on the estimated position of the landmarks can be expected. Accordingly, during the validation of XIMIT an impact of the pelvis orientation with respect to the z-axis on the matching could be observed in only one out of 49 images. Still, in an improved version of the system a change of this orientation will be compensated by pre-rotating the patch with the negative angle of the in-plane rotation. This angle can be well estimated by comparing the orientation of $\mathbf{m}_2 - \mathbf{m}_1$ in the reference to the one in the comparison radiograph (when

a   b
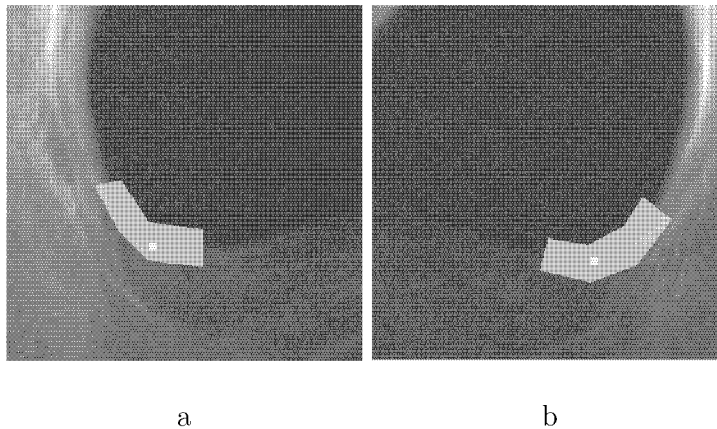
Figure 4.2: *The Figures a and b show the user defined templates of the left and of the right foramen obturatorum, respectively, used for locating $\mathbf{m}_1$ and $\mathbf{m}_2$ in the comparison image.*

matching the corners of the foramina obturatoria, the initial estimates for $\mathbf{m}_{1,2}$ in the latter image may be taken).

4.3.1 Definition of the templates

The templates are defined by the user, by marking a region of interest (ROI) with several mouse-clicks. For $\mathbf{m}_1$ and $\mathbf{m}_2$, the areas along the contours of the foramina obturatoria shown in Fig. 4.2 are chosen as templates. If the contours of the foramina obturatoria are regarded only piecewise they are structures which are quite robust at motions of the pelvis. Although often the contrast between bone and background is low in this image area, they can be matched reliably due to the inherent robustness of the method in images with low contrast (see the LSM application in [Berger 1999]).

Locating the bony landmark $\mathbf{m}_3$ is more problematic. The appearance of the teardrop figure in the image strongly depends on the position and orientation of the pelvis (see Fig. 4.3). Additionally, as can be seen in Fig. 4.4, this figure looks different in each hip, and is sometimes hardly visible. It is hence difficult to develop a general procedure in defining the template.

One rule could be found by evaluating the validation radiographs. At the beginning, the straight-forward approach was tried out, and all the structured parts of this figure were included in the template (see Fig. 4.5a). As reported in detail in Sect. 7.3.1, this often led to a mismatch. Consequently, attention was paid to the parts which look different in the reference and in the comparison radiograph. This problem was found to be especially acute for the lateral area of the teardrop figure superposed by the so-called ilio-ischial line. That bony feature is the line visible in the Figures 4.3 and 4.4, which runs in cranio-caudal direction and lies lateral to the teardrop figures. Its medio-lateral position was affected by out-of-plane rotations as well as by x-translations of the pelvis. This observation

a   b   c   d   e
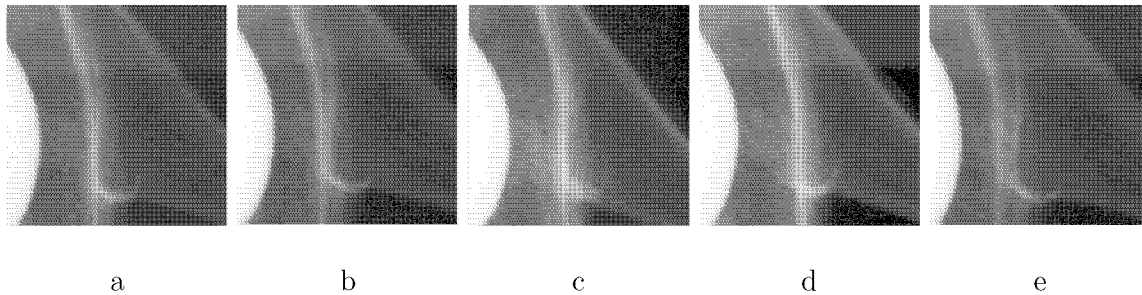
Figure 4.3: *The left teardrop figure in the validation radiographs of series 1 (see Sect 6.2).
In Fig. a, the pelvis is in its neutral position and orientation, in (b) it its shifted of 24 mm
to the right, in (c) tilted around its medio-lateral axis with an angle of 6.6°, and in (d) and
(e) it is rotated around its cranio-caudal axis with an angle of 2.2° and −3.3°, respectively.*

a   b   c   d   e
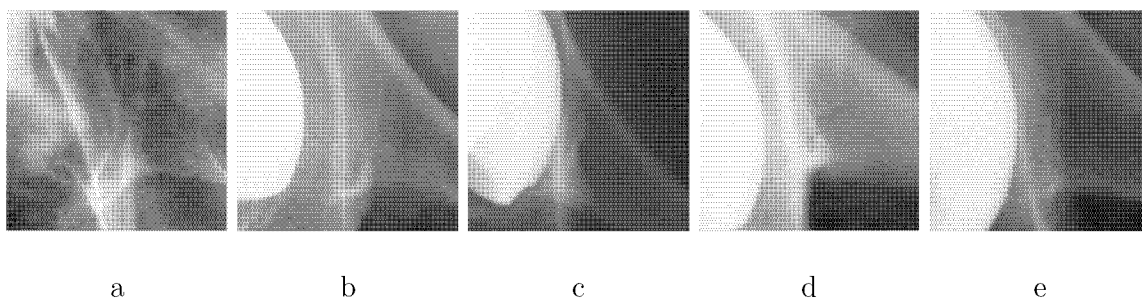
Figure 4.4: *The Figures a–e show teardrop figures in five different hips.*

a   b
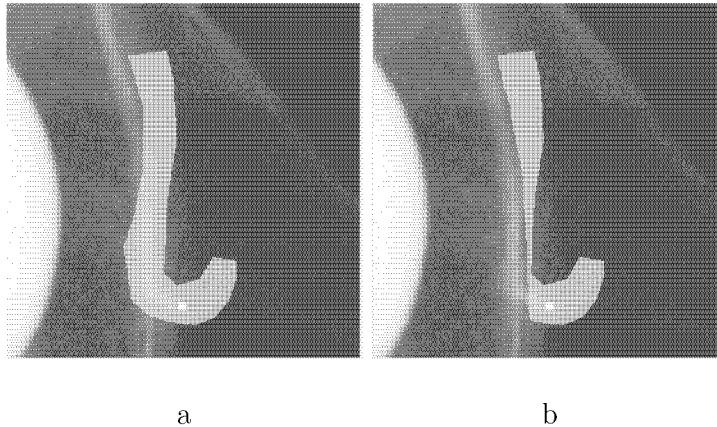
Figure 4.5: *The teardrop figure template with the ilio-ischial line included (a) and excluded (b).*
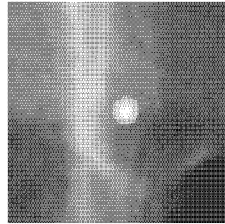
Figure 4.6: *The template of the external markers.*

corresponds to the experimental results in [Goodman *et al.* 1988], where the position of this line relative to the teardrop figure was found to be very instable.

Accordingly, the ilio-ischial line was omitted from the matching. The pixels of this line in the reference as well as in the comparison radiograph were excluded from the template. For the exclusion of the comparison image pixels, the prospective position of the patch after the minimization had to be taken into account. That was achieved by marking in the comparison image the line's area, by representing the pixel coordinates of the marked area with respect to the initial estimate of the teardrop figure point, and by cutting the pixels having these coordinates relative to m_3 from the ROI in the reference image. This template definition provided good numerical results in the experimental validation (see Sect.7.3). It could be further improved by generally considering only such pixels in the matching procedure which were marked in the reference as well as in the comparison image. Additionally, the marked area in the latter image would have to be transformed during the LSM minimization according to the current estimate of the mapping. Then, regions in the comparison image could be included or omitted before starting the parameter estimation under exact consideration of the final transformation between template and patch. Unfortunately, in this way the user dependency of the method would be increased. Moreover the situation can be made more complicated by the fact that it is not always

clear which structures belong to the ilio-ischial line and which to the teardrop figure (see Fig. 4.4c).

Nevertheless, the teardrop figure is assumed to be the only natural bone reference which allows for a sufficient precision in assessing the migration. As mentioned already in Chapter 3, a precise as well as universal method could be achieved by the implantation of an artificial marker situated in the anatomical structures forming the teardrop figure. In the experiments, the use of small tantalum balls as landmark $\mathbf{m}_3$ was tested. Using templates such as the one shown in Fig. 4.6, the balls could be matched without problems.

5

Locating the cup

Whereas for the bony structures no 3D information is available, a 3D analysis of the implant is possible using its CAD data. To precisely determine the cup reference point and the magnification, the cup's position in the x-ray system is recovered. The position as well as the orientation parameters are estimated by minimizing the gray value differences between the original x-ray projection of the cup and the one synthesized using the surface. An initial estimate of the parameters is given by the user. As stated earlier, this approach was named "Analysis-by-Synthesis".

The term Analysis-by-Synthesis was adopted from the field of computer graphics. It has been proposed as a method for generating a 3D model of an object in video sequences made by a single camera [Koch 1990, Koch 1993] or in several images acquired from different views [Busch 1989]. Based on an initial model estimate, a synthetic image is generated. The model is adapted to the object iteratively, by evaluating the gray value differences between the real image und the synthetic one updated after each step. In medical image analysis, a similar approach has been used by [Lötjönen *et al.* 1999] for the reconstruction of anatomical 3D surfaces from radiographs by comparing synthetic x-ray projections with two real images.

In the context of this work, the principle of Analysis-by-Synthesis is used for finding the position and orientation of a well defined object using one (x-ray) image, instead of recovering an object model using several projections. The concept here corresponds to the one described in [LaRose *et al.* 2000] and mentioned already in the introduction: The position and orientation parameters of a pelvic CT volume relative to the ones in an individual x-ray image are reconstructed by matching a DRR (digitally reconstructed radiograph) with the image. In [LaRose *et al.* 2000], also a way of estimating the parameters of the artificial hip socket using its CAD model is proposed. This approach is, however, not based on synthetic x-ray images, but on the analysis of the cup contour in the radiographs. Matching the contour implies, however, on the one hand its extraction and on the other the utilization of only a part of the image data. The direct comparison of pixel values implemented here is not only straight-forward, but also allows for the evaluation of all available image information. The measure for the similarity of synthetic and real data was chosen to be the sum of the squared gray value or gradient differences in each pixel.

The development of the algorithm involved several steps covering different technical fields: Locating the cup in the x-ray system requires the approximate focus–film constellation at

exposure. For an exact reconstruction of the intrinsic parameters, which was necessary for the validation, a method for calibrating the x-ray system was developed (Sect. 5.1). The x-ray image is synthesized by simulating the attenuation of the primary radiation through the cup. The attenuation depends on the lengths of the rays within in the cup surface as well as on the x-ray energy spectrum. In order to obtain a suitable representation of the surface, the CAD data needed to be converted and topological errors had to be eliminated (Sect. 5.2). The x-ray spectrum was estimated considering the attenuation of the initial photons through the objects between x-ray source and film, which are mainly the body and an anti-scatter grid (Sect. 5.3). The length of the rays within the cup are calculated by means of a scan line rendering algorithm originating from the field of computer graphics. The gray values of the synthetic image subject to the ray lengths is approximated by a quite simple expression, where also the energy dependent blackening of the x-ray film is taken into account (Sect. 5.4). The neglected scattered radiation is considered by a subsequent frequency dependent equalization of the synthetic and the original image (Sect. 5.5). The parameters of the orientation are three angles defining subsequent rotations around axes fixed to the implant (5.6). This representation facilitates the definition of the initial estimate of the cup's 3D parameters. This estimate is gained by manually fitting a projected circle to the circumference of the cup's opening plane (Sect. 5.7). The final estimate is obtained by minimizing the difference between the original and the synthetic image as described in (Sect. 5.8). From the found 3D position and orientation, the magnification factor, the cup's image reference point, and additionally its rotation between two radiographs is calculated (Sect. 5.9).

5.1   Film–focus constellation

The x-ray system was modeled by a pinhole camera geometrically defined by the distance f between focus and film plane, and the intersection $\mathbf{t} = (t_x, t_y)$ of the z-axis with this plane. For the migration measurement, the exact size of the intrinsic parameters plays a secondary role, because a deviation from their real values is automatically neutralized by an appropriate x-y- and z-translation of the cup during Analysis-by-Synthesis. The film–focus distance is assumed to have the nominal value of the x-ray unit, which varies from hospital to hospital in the range of 900 mm to 1300 mm. In the used anterior-posterior pelvis exposures, the central beam is supposed to be perpendicular to the film plane. This beam usually is directed to the film center, which is hence assumed to give the intrinsic parameter $\mathbf{t}$.

For the validation of Analysis-by-Synthesis the intrinsic parameters were precisely estimated. This was achieved by acquiring radiographs of a plastic calibration box (detailed description in Sect. 6.1.1), which contains in its bottom and in its cover uniformly distributed metal balls. For testing the calibration, radiographs of a box with altogether 18 balls were taken. For the later validation experiments, a box with 24 balls was roentgenized together with a pelvis phantom. The 3D positions of the ball centers had been measured precisely before the validation experiments. The calibration was run using the graphical
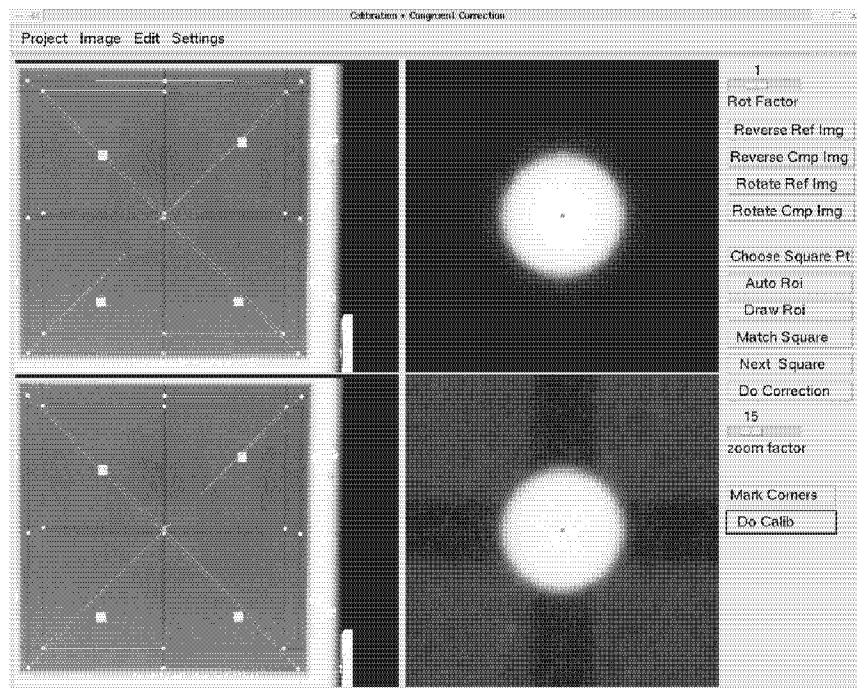
Figure 5.1: *The graphical user interface for calibrating the x-ray system. The reference and the comparison image are displayed in the upper and and in the lower left window, respectively. On the right, the synthetic sphere template (top) and the patch (bottom) warped with the transformation estimated using LSM are shown. The small points in the middle are the projected 3D sphere centers.*

user interface written IDL [Fanning 1999] and shown in Fig. 5.1. A reference and a comparison image can be loaded for an adaption of the film position and orientation, which can vary in the cassette or during the scanning. The comparison image is warped with a congruent transformation, which is estimated using markers fixed to the x-ray table, such as the four small metall plates visible in Fig. 5.1. To give an initial estimate for the image positions of the balls in the calibration box, the user marks the centers of the corner spheres with the mouse (see in Fig. 5.1). By assuming that the spheres are equally spaced the initial estimate for the inner ones is gained. Starting the calibration procedure, the exact 2D positions of the sphere centers are determined automatically by synthesizing templates and applying LSM (see Sect. 5.1.1). Subsequentially, the intrinsic parameters are estimated as described in Sect. 5.1.2.

5.1.1 Image positions of the calibration spheres

The centers of the calibration spheres are precisely located in the x-ray images by matching synthesized x-ray images of balls to their projections. The generation of synthetic templates is necessary, because only the relative transformation of the template between two images can be estimated using LSM. The matching requires a reference point, which here has to

be the projection of the 3D ball center. However, it is difficult to know in a given sphere image which point is exactly the projection of the center. Using a synthetic template of a sphere generated as described in the following two paragraphs, the 3D center and its projection are known by definition.

The 3D centers at the exposure are roughly assessed by reprojecting the initial estimates of the 2D coordinates. In doing so, f is set to its nominal value, $\mathbf{t}$ to the film center, and the calibration box is assumed to be situated parallel to the x- and y-axis of the x-ray coordinate system and to be centered with respect to the film. The box' distance to the focus is roughly estimated using f and the distance between the x-ray film and the table. These settings are assumed to be valid throughout the following part of this subsection and also serve as initial estimate for the minimization.

For each pixel in the synthesized template, an x-ray is defined reaching from the focus to the pixel center. The attenuation of a ray is approximated by calculating its length in a sphere subject to the known radius r^{sphere} and the approximate 3D center $\mathbf{S}'_m$. The index m goes from 1 to m_{max}, where m_{max} is the total number of spheres. The length $l_m^{\mathrm{sphere}}(\mathbf{p}_i)$ of the x-ray belonging to the template pixel $\mathbf{p}_i$ in the sphere m is expressed analytically by

$$l_m^{\mathrm{sphere}}(\mathbf{p}_i) = 2 \cdot \sqrt{\frac{\left((p_{i_x}-t_x)S'_{m_x} + (p_{i_y}-t_y)S'_{m_y} + fS'_{m_z}\right)^2}{(p_{i_x}-t_x)^2 + (p_{i_y}-t_y)^2 + f^2} - |\mathbf{S}'_m|^2 + r^{\mathrm{sphere}2}} \ .$$

The gray value at $\mathbf{p}_i$ is approximated by $1 - \exp\left(-\mu^{\mathrm{iron}} \cdot l_m^{\mathrm{sphere}}(\mathbf{p}_i)\right)$, where μ^{iron} is the attenuation coefficient of iron. It is $\mu^{\mathrm{iron}} = 15.4\,\mathrm{cm}^{-1}$ at the assumed mean x-ray energy of $50\,\mathrm{eV}$. The sphere's synthetic image is scaled so that its minimal and its maximal gray value correspond to the ones of the patch, which is the region of the sphere in the calibration image.

Having synthesized the template, a circular ROI situated at the sphere center is computed. For each sphere the LSM procedure introduced in Chapter 4 is run with the initial estimate $\tilde{\mathbf{h}} = (1, 1, 0, 0, 0, 0)^{\mathrm{T}}$ for the matching and the constraints $m_x^{\mathrm{lsm}} = m_y^{\mathrm{lsm}}$ and $s_x^{\mathrm{lsm}} = s_y^{\mathrm{lsm}} = 0$. Adding to the initial estimates of the 2D sphere center the resulting translations $(t_x^{\mathrm{lsm}}, t_y^{\mathrm{lsm}})$ yields the 2D coordinates $\mathbf{s}_m$.

5.1.2   Calibration

The projections of the 3D sphere centers on the film plane depend on the intrinsic as well as on the extrinsic parameters, i.e. the position $\mathbf{T}^{\mathrm{calib}} = (T_x^{\mathrm{calib}}, T_y^{\mathrm{calib}}, T_z^{\mathrm{calib}})^{\mathrm{T}}$ and the orientation $\mathbf{R}^{\mathrm{calib}}$ of the calibration box. They are given by

$$
\begin{aligned}
s_{m_x} &= f_x \cdot \frac{(\mathbf{R}^{\mathrm{calib}}\mathbf{S}_m)_x + T_x^{\mathrm{calib}}}{(\mathbf{R}^{\mathrm{calib}}\mathbf{S}_m)_z + T_z^{\mathrm{calib}}} + t_x \\
s_{m_y} &= f_y \cdot \frac{(\mathbf{R}^{\mathrm{calib}}\mathbf{S}_m)_y + T_y^{\mathrm{calib}}}{(\mathbf{R}^{\mathrm{calib}}\mathbf{S}_m)_z + T_z^{\mathrm{calib}}} + t_y \ ,
\end{aligned}
\tag{5.1}
$$

where $\mathbf{S}_m$ indicates the measured 3D coordinates of the balls. The matrix $\mathbf{R}^{\mathrm{calib}}$ describing the box' orientation is defined analogously to (2.1), but inserting the angles α^{calib}, β^{calib},
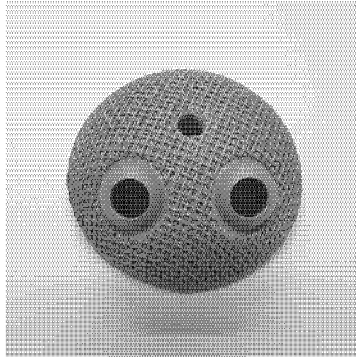
Figure 5.2: *The exterior of the cup.*

and γ^{calib} of the orientation with respect to the x-, the y-, and the z-axis, respectively. Initially, these angles are set to zero. For the film–focus distance the two parameters f_x and f_y are introduced taking into account that digitizing the x-ray image may lead to a different scaling in x- and in y-direction.

Based on the expressions (5.1), the calibration is formulated as a least squares minimization problem (see Chapter 4) with the residual equations

$$
e_{2m-1} \;=\; f_x \cdot \frac{(\mathbf{R}^{\mathrm{calib}}\mathbf{S}_m)_x + T_x^{\mathrm{calib}}}{(\mathbf{R}^{\mathrm{calib}}\mathbf{S}_m)_z + T_z^{\mathrm{calib}}} + t_x - s_{m_x}
$$

$$
e_{2m} \;=\; f_y \cdot \frac{(\mathbf{R}^{\mathrm{calib}}\mathbf{S}_m)_y + T_y^{\mathrm{calib}}}{(\mathbf{R}^{\mathrm{calib}}\mathbf{S}_m)_z + T_z^{\mathrm{calib}}} + t_y - s_{m_y} \;.
$$

Inserting the 3D and the 2D coordinates of all the calibration spheres, $2\,m_{\max}$ such equations result. They are combined into the objective function $\mathbf{e}^{\mathrm{T}}\mathbf{P}\mathbf{e} = \mathbf{e}^{\mathrm{T}}\mathbf{e}$, $\mathbf{e} = (e_1, ..., e_{2m_{\max}})^{\mathrm{T}}$ under the assumption that the weight matrix $\mathbf{P}$ is the identity matrix. The latter is minimized with respect to f_x, f_y, t_x, t_y as well as to $\mathbf{T}^{\mathrm{calib}}$, α^{calib}, β^{calib}, and γ^{calib} by applying the Gauss-Newton minimization scheme described in Sect. 4.2.

5.2   Surface data of the cup

Up to now, only one type of cup was evaluated. It consists of a titanium shell and a polyethylen liner. As the liner is not visible in the radiographs it plays no role in this work. The metal shell can again be subdivided in a full titanium core and the less dense titanium grid on the outside visible in Fig. 5.2. The surface data of the titanium parts were available in vrml format and saved in two seperate files. The problem of the original data was that the surfaces contained holes. Calculating the absorption of x-rays passing through these holes is not possible. With the following procedure, most of these holes were eliminated. In the original data, the total surface represented by triangles is split in several pieces. The vertex indices of each triangle and the vertex coordinates are listed piecewise. First, the coordinates of all pieces are merged into one list while eliminating double appearance

of one vertex. While doing so, the indices are updated. Subsequently, the edges of each triangle, i.e. its three couples of indices, are listed. The edges appearing only once in that list are extracted, as they belong to the border of a hole or to triangles sticking out of the surface. The connection between the single edges is found out, and the ones which are again connected to triangles are extracted and stored. The vertex indices of the extracted edges are added to the index list, while the rest of the single edges is neglected (in the case of the evaluated CAD data, the holes mainly consist of triangles). Finally, the added and the old triangles are stored line by line, each containing the coordinates of the three vertices. This procedure is run for both cup parts.

5.3   Spatially independent x-ray energy spectrum

The x-ray photons are detected by the screen-film system situated under the examination table. The screen transforms the high energetic x-rays into visible light, which is detected by the film. The blackening of the film depends on the number of photons hitting the screen. The number of photons per time, i.e. the intensity of a ray, is changed by the attenuation through the objects between x-ray source and screen. Thus, heterogeneous objects, like the pelvis with the implant, lead to spatially inhomogeneous x-ray intensities, which produces the image. The ray attenuation, however, not only depends on the local object properties, but also on the energy of the photons. Hence, in order to determine the attenuation through the cup, the spectrum of the radiation, which is the ray intensity subject to the energy, needs to be known.

The spectrum of the radiation leaving the x-ray tube is usually filtered by an aluminium slab. Assuming the usual tube voltage of 73 keV and an aluminium filter of 2.5 mm this initial spectrum is generated at the energies E_j ($E_j = 1$ keV, 2 keV, ..., 73 keV) using the program XOP based on a Monte-Carlo simulation [Sanchez del Rio and Dejus 2000]. It is indicated with $N^0(E_j)$ and plotted in Fig. 5.5 (dotted line) scaled to a maximum photon number of 50 per tube current [mA], and per area [mm^2].

The initial spectrum is altered mainly by the body, by the implant, and by an anti scatter grid installed between examination table and film. The interest here lies in the spatial intensity change through the cup. Therefore, the heterogeneity of the pelvic zone around the implant is neglected. The attenuation through the body and the grid is modeled by a energy dependent but spatially constant reduction of the intensity. It hardens the beams, that means the photons with high energy are transmitted more probably than the ones with low energy. Neglecting the scatter, the intensity $N(E_j)$ at the energy E_j is the product of the initial spectrum with the photon transmission probability of the hip region $B^{\text{body}}(E_j)$ and with the one of the anti scatter grid $B^{\text{anti}}(E_j)$:

$$N^{\text{const}}(E_j) = N^0(E_j) \cdot B^{\text{body}}(E_j) \cdot B^{\text{anti}}(E_j)$$

The transmission probabilities $B^{\text{body}}(E_j)$ and $B^{\text{anti}}(E_j)$ are estimated as described in the following two subsections.
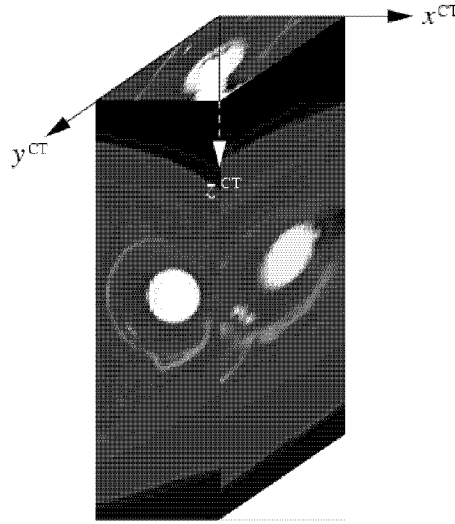
Figure 5.3: *The CT volume in the area of the acetabulum.*

5.3.1 Beam hardening through the body

The attenuation of the primary radiation through the body was estimated using a pelvis CT data set with a polyethylen cup implanted. The acetabular region was clipped from the volume yielding the cuboid illustrated in Fig. 5.3. It contains $50 \times 50 \times 228$ cubic voxels with a side length of $1.33\,\text{mm}$. Its axes x^{CT}, y^{CT}, and z^{CT} (medio-lateral, cranio-caudal, and ventral-dorsal, respectively) were defined correspondingly to the ones of the x-ray system.

The CT data are given in Hounsfield units H, which are integer values reaching from -1000 to about 3000. They can be converted into the energy dependent attenuation coefficients $\mu(H, E_j)$ by

$$\mu(H, E_j) = H \cdot \frac{\mu^{\text{H}_2\text{O}}(E_j)}{1000} + \mu^{\text{H}_2\text{O}}(E_j) \,.$$

The attenuation coefficients $\mu^{\text{H}_2\text{O}}(E_j)$ of water at the energies E_j were interpolated using the data in [National Institute of Standards and Technology 1997]. Assuming x-rays parallel to the ventral-dorsal axis of the volume data, the histogram along z^{CT} was calculated for each column x_m^{CT}, y_n^{CT}, where $m = 1, ..., 50$ and $n = 1, ..., 50$. The mean of the 50×50 histograms scaled by the voxel side length is shown in Fig. 5.4. The plot gives the average length $\bar{l}(H)$ of a ray in the material with the Hounsfield unit H. From left to right, the main peaks in this plot arise from: external material such as the mattress where the patient lies on, soft tissue, bone, and the femoral head. The attenuation by a certain material depends exponentially from the product between attenuation coefficient and ray length in the material. The overall transmission probability is estimated summing the proportions $\mu(H, E_j) \cdot \bar{l}(H)$. The
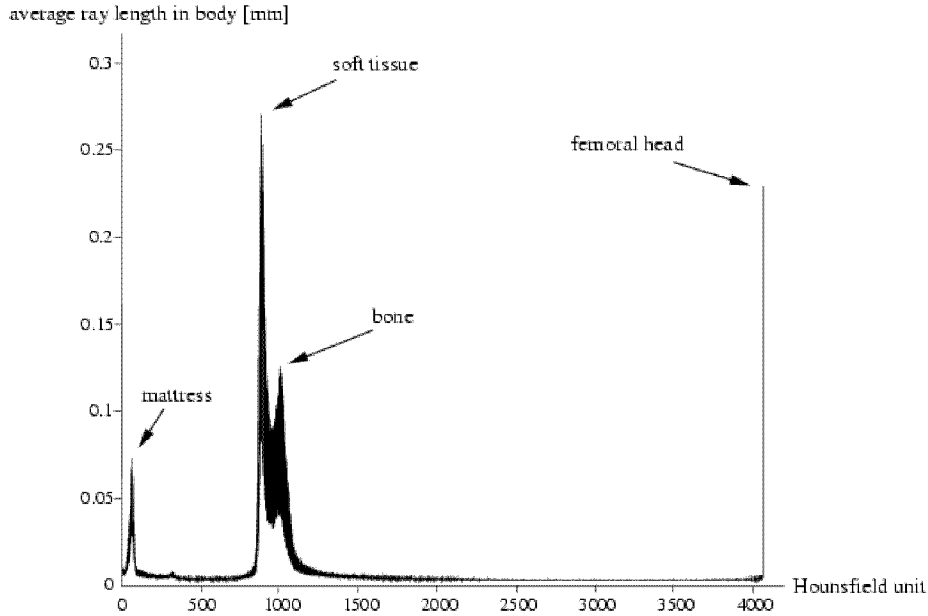
Figure 5.4: *Average histogram of the CT data in the area of the acetabulum scaled by the voxel side length.*

femoral head is excluded from this summation by neglecting Hounsfield units greater than 3000, while the first peak is included taking into consideration the attenuation through the mattress.

$$B^{\text{body}}(E_j) = \exp\left(-\sum_{H=-1000}^{3000} \mu(H, E_j) \cdot \bar{l}(H)\right)$$

The attenuation through the body and the underlay diminishes the intensity to 0.78 % of the initial one and increases the mean energy from 43.6 keV to 52.9 keV. In Fig. 5.5, the exit spectrum $N^0(E_j) \cdot B^{\text{body}}(E_j)$ scaled to a maximal photon number of 50 is plotted with a dashed-dotted line.

5.3.2   Beam hardening through the anti scatter grid

The anti scatter grid is installed between examination table and film cassette. It increases the image contrast by a reduction of the scattered radiation. The grid consists of upstanding lead strips arranged parallel to the y-axis and covered on both sides by an aluminium plate. The strips are tilted so that they all point to the approximate x-position of the focus. Scattered photons, which have angles deviating from the ones of the primary photons, are absorbed by the lead lamellas. However, also the primary radiation is attenuated by the grid. In order to avoid an inhomogenous attenuation the grid oscillates with a high velocity along the x-axis. In the following paragraph, the mean length of the x-rays in the grid is estimated. Afterwards, the attenuation of the rays passing through the grid is determined.

Assuming a focused grid, this means that the primary photons run parallel to the lamellas, a photon either hits lead or the interspace material which is aluminium. Indicating with h the height of the grid, with θ the angle between photon and z-axis, and with $\mu^{\text{lead}}(E_j)$ the attenuation coefficient of lead, in the first case the transmission probability of the primary radiation is $\exp\left(-\mu^{\text{lead}}(E_j) \cdot \frac{h}{\cos\theta}\right)$. In the latter it is $\exp\left(-\mu^{\text{alu}}(E_j) \cdot \frac{h}{\cos\theta}\right)$, where $\mu^{\text{alu}}(E_j)$ is the attenuation coefficient of aluminium. The grid used in this work has a height of $h = 2.95\,mm$. The maximal range $[\theta^-, \theta^+]$ of the polar angle for the area of the cup depends on its radius and its position. It is estimated by

$$\theta^\pm = \tan^{-1}\left((\sqrt{C_x^2 + C_y^2} \pm r)/C_z\right) \ .$$

At the average cup radius of $25\,mm$ and at the cup position $\mathbf{C} = (98.0\,mm,\ -18.3\,mm,\ 870.0\,mm)$ adopted from Chapter 3, θ reaches from $4.9\,°$ to $8.2\,°$. In this range, the lengths of the rays in the grid vary only slightly and can be assumed to have the constant value of $\frac{h}{\cos\theta} = 2.97\,mm$.

The oscillation velocity is supposed to be so high that during the exposure time the grid covers a distance of at least one strip plus interspace. A ray after the screen consists of the photons having passed through the strips and of the ones having passed through the interspace. For the first ones, the transmission probability can be assumed to be zero because of the high attenuation coefficient of lead. The latters' proportion of the radiation before the screen is estimated to be $\frac{d^{\text{inter}}}{d^{\text{inter}} + d^{\text{strip}}}$, where d^{inter} is the interspace width and d^{strip} the one of the strips. In the used grid these widths are 0.21 mm and 0.04 mm, respectively. Thus, the transmittance through the lamella part of the grid can be approximated by $\frac{0.21}{0.25} \cdot \exp\left(-\mu^{\text{alu}}(E_j) \cdot 2.97\right)$.

Apart from the lamella part, the radiation is altered by the aluminium covers having a thickness of 0.2 mm each. At this point, also the attenuation through the examination table is taken into account, which corresponds to the one of an additional 0.6 mm aluminium layer. The total transmission probability through the grid and the table hence is

$$B^{\text{anti}}(E_j) = \frac{0.21}{0.25} \exp\left(-\mu^{\text{alu}}(E_j) \cdot \ (0.4\,\text{mm} + 2.97\,\text{mm} + 0.6\,\text{mm})\right) \ . \tag{5.2}$$

It was calculated by insertion of the attenuation coefficient of aluminium, which was interpolated using the values given in [National Institute of Standards and Technology 1997]. The multiplication of (5.2) by $N^0(E_j)B^{\text{body}}(E_j)$ yielded the dashed line in Fig. 5.5. It shows the spatially independent energy spectrum of the beams having passed the body, the table, and the grid. It is again scaled so that its maximum is 50.

For the experimental validation of XIMIT, radiographs of a pelvis bone without soft tissue were acquired. This phantom was mounted on several plastic plates of an overall thickness of 4 cm. The plastic layers also attenuate the radiation, but do not compensate for the missing soft tissue. Accordingly, the spectrum must have been shifted to lower energies in the experiments. During the evaluation of the validation radiographs, it was tried to simulate the experimental conditions. However, assuming a softer radiation than the one plotted in Fig. 5.5 (dashed line), the resulting synthetic x-ray projection of the cup showed

number of photons
mA mm²
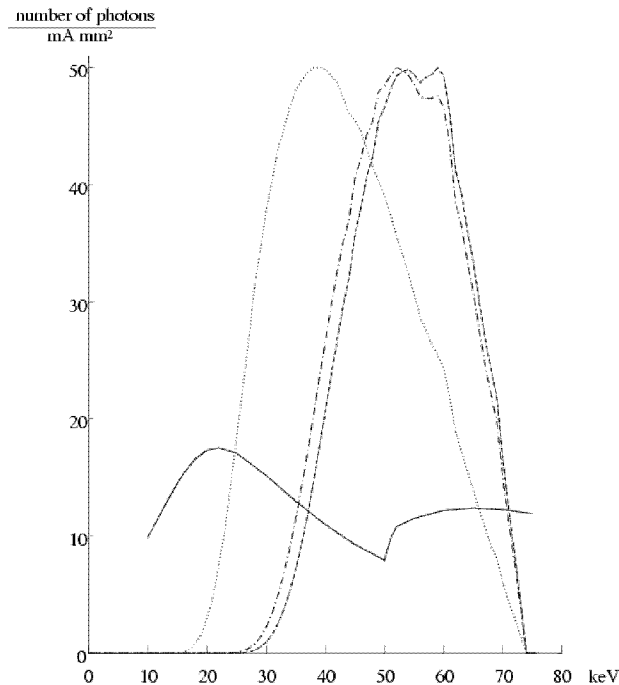
Figure 5.5: *The energy spectrum of the x-rays initially (dotted line), after the body (dashed-dotted line), and after the anti-scatter grid (dashed line). Additionally, the solid curve shows the fractions of energy [%] of the incident photons which contribute to the image information (see Sect. 5.4.2).*

less contrast than the original one in the validation radiograph. This indicates that the attenuation through the cup was overestimated, that means the energies assumed were too low. Therefore, the above spectrum reflecting clinical conditions was also taken for the validation. The origin of the unexpectedly small attenuation in the experiments may have been the film–focus distance increased from 120 cm to 140 cm. The lead strips in the anti-scatter grid are tilted with respect to a limited range of film–focus distances. If this range is exceeded, the rays are not parallel to the strips any more. They are partly attenuated by the lead strips, which causes an additional shift of the spectrum to higher energies.

5.4 Synthesizing the cup's x-ray image

The gray values of the synthesized x-ray image are determined by simulating the attenuation of the primary radiation through the cup. While doing so, the scattered radiation is neglected. To each image pixel, a ray is defined reaching from the focus to the pixel center. The attenuation depends upon the length of the ray inside the cup. This length is calculated as described in Sect. 5.4.1 by intersecting the ray with the surfaces of the two cup parts. An expression for the gray values of the synthetic image subject to the ray
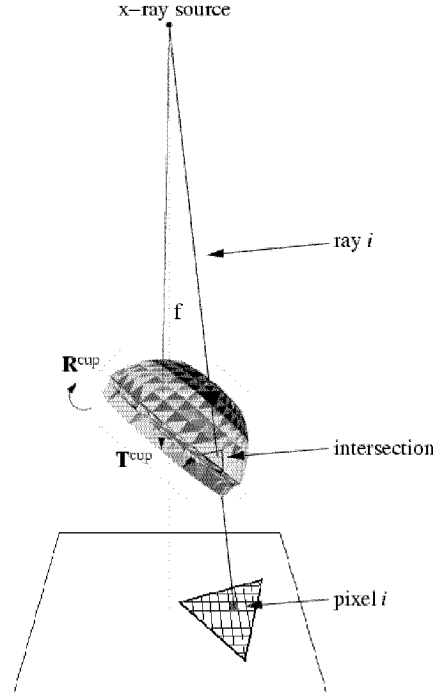
Figure 5.6: *Illustration of the scan line rendering algorithm used for calculating the intersections of the x-rays with the implant surface.*

lengths was derived as presented in Sect. 5.4.2. The derivation required the consideration of the x-ray spectrum and of the energy dependent blackening of the film.

5.4.1 Lengths of the rays inside the cup

The surfaces consist of altogether about 18,000 triangles and the image area containing the cup of about 700,000 pixels. Thus, testing the intersection of each ray with each triangle would require a great many operations. In order to faster compute the intersections, a scan line rendering algorithm was implemented. The vertices $\mathbf{V}_{k_{10,20,30}}$ of the triangle k are rotated and translated inserting the current 3D position and orientation parameters and then projected on the image. Their positions in the image $\mathbf{v}_{k_{1,2,3}}$ are calculated through

$$\mathbf{v}_{k_{1,2,3}} = f \cdot \left(\frac{\mathbf{V}_{k_{1,2,3}x}}{\mathbf{V}_{k_{1,2,3}z}}, \frac{\mathbf{V}_{k_{1,2,3}y}}{\mathbf{V}_{k_{1,2,3}z}} \right)^{\mathrm{T}} + \mathbf{t} , \qquad \mathbf{V}_{k_{1,2,3}} = \mathbf{R}^{\mathrm{cup}} \mathbf{V}_{k_{10,20,30}} + \mathbf{T}^{\mathrm{cup}} .$$

The vector $\mathbf{T}^{\mathrm{cup}} = (T_x^{\mathrm{cup}}, T_y^{\mathrm{cup}}, T_z^{\mathrm{cup}})$ indicates the current position of the cup. The matrix $\mathbf{R}^{\mathrm{cup}}$ represents its orientation, which is defined by three angles of rotation around cup fixed axes (a detailed description follows in Sect. 5.6).

The projected triangle is scanned line by line for pixel centers lying inside its area. This gives the rays which intersect the triangle in 3D. The center $\mathbf{p}_i$ of the ith pixel lying inside can be represented by the barycentric coordinates r_{ik}, l_{ik}, and s_{ik}:

$$\mathbf{p}_i = r_{ik} \cdot \mathbf{v}_{k_1} + l_{ik} \cdot \mathbf{v}_{k_2} + s_{ik} \cdot \mathbf{v}_{k_3}$$

These coordinates are defined by the areas $\mathrm{A}\left[\mathbf{v}_{k_1}\mathbf{v}_{k_2}\mathbf{v}_{k_3}\right]$ and $\mathrm{A}\left[\mathbf{p}_i\mathbf{v}_{k_m}\mathbf{v}_{k_n}\right]$ of the triangles $\mathbf{v}_{k_1}\mathbf{v}_{k_2}\mathbf{v}_{k_3}$ and $\mathbf{p}_i\mathbf{v}_{k_m}\mathbf{v}_{k_n}$ $(m, n = 1, 2, 3$ and $n \neq m)$, respectively:

$$r_{ik} = \frac{\mathrm{A}\left[\mathbf{p}_i\mathbf{v}_{k_2}\mathbf{v}_{k_3}\right]}{\mathrm{A}\left[\mathbf{v}_{k_1}\mathbf{v}_{k_2}\mathbf{v}_{k_3}\right]}, \qquad l_{ik} = \frac{\mathrm{A}\left[\mathbf{p}_i\mathbf{v}_{k_1}\mathbf{v}_{k_3}\right]}{\mathrm{A}\left[\mathbf{v}_{k_1}\mathbf{v}_{k_2}\mathbf{v}_{k_3}\right]}, \qquad s_{ik} = \frac{\mathrm{A}\left[\mathbf{p}_i\mathbf{v}_{k_1}\mathbf{v}_{k_2}\right]}{\mathrm{A}\left[\mathbf{v}_{k_1}\mathbf{v}_{k_2}\mathbf{v}_{k_3}\right]} \, .$$

The 3D intersection $\mathbf{P}_{ik}$ of the ray belonging to the pixel i with the triangle k is approximated by

$$\mathbf{P}_{ik} = r_{ik} \cdot \mathbf{V}_{k_1} + l_{ik} \cdot \mathbf{V}_{k_2} + s_{ik} \cdot \mathbf{V}_{k_3} \, .$$

Its distance to the focus is given by $|\mathbf{P}_{ik}| = \sqrt{P_{ik_x}^2 + P_{ik_y}^2 + P_{ik_z}^2}$. This distance is calculated for all the pixels inside the triangle. It is stored in a buffer having the size of the image times the maximum number of intersections with the cup surface, which is about 16.

Having scanned all triangles, the distances of the ray intersections to the focus are sorted from minimum to maximum. This yields couples of surface entry and exit points. The total length $l^{\text{full}}(\mathbf{p}_i)$ or $l^{\text{grid}}(\mathbf{p}_i)$ of the ray belonging to the pixel i inside the full or the grid part is obtained by summing the differences between the coupled points. In case the number of intersections is odd in one pixel, because the ray hit a hole in the surface, the total length is set to the one of the preceding pixel.

5.4.2   Image intensities subject to the ray lengths

In this subsection, it is described how the gray values in the synthetic image are obtained from the computed ray lengths $l^{\text{full/grid}}(\mathbf{p}_i)$. The transmission probability of the x-ray photons subject to the lengths is determined as described in the first of the following paragraphs. It alters the spatially independent x-ray spectrum of Sect. 5.3 into a spectrum depending on the position of a pixel. In the second paragraph, an expression is derived for estimating the part of the total spectral energy enhancing the image information. The film density is supposed to be linear to this portion. Based on this assumption, the model for the gray values in the x-ray image described in the third paragraph of this subsection was found. It is simplified as shown in the last paragraph in order to save computing time.

The transmission probability $B^{\text{cup}}(E_j, \mathbf{p}_i)$ of the cup is given by

$$B^{\text{cup}}(E_j, \mathbf{p}_i) = \exp\left(-\mu^{\text{full}}(E_j) \cdot l^{\text{full}}(\mathbf{p}_i) - \mu^{\text{grid}}(E_j) \cdot l^{\text{grid}}(\mathbf{p}_i)\right) \, .$$

The attenuation coefficient $\mu^{\text{full}}(E_j)$ of the full part is interpolated at the values of $E_j = 0\,\text{keV}$, $1\,\text{keV}, \dots, 73\,\text{keV}$ using the data from [National Institute of Standards and Technology 1997]. The grid part is modeled as an object with a homogenous but lower density. It is assumed

to have an attenuation coefficient of $\mu^{\text{grid}} = 0.35 \cdot \mu^{\text{full}}$ as it has a mean density of 35% of the one of the full part. Now, the local photon intensity $B^{\text{cup}}(E_j, \mathbf{p}_i) \cdot N^{\text{const}}(E_j)$ at the screen considering the attenuation by the cup, the body, the table, and the anti-scatter grid can be calculated.

In order to determine the density of the film, it also has to be taken into account that the energy of the photons also plays a role at their detection by the screen. The blackening of the film depends on the energy absorbed by the screen. In [Birch and Marshall 1979], the "useful absorbed energy" of a photon is determined for different screens. It is defined as the fraction $E_j^{\text{frac}}(E_j)$ of the photon energy E_j which enhances the image information. The fraction depends on the thickness of the screen, and on the attenuation and mass energy transfer coefficients of the screen phosphor. In this work, a rare earth ($Gd_2O_2S_2$) screen with a sensitivity of 200 was used. It is assumed to correspond to the rare earth screen Kodak MIN-R investigated by [Birch and Marshall 1979]. Taking the data of [Birch and Marshall 1979], for this screen the fractions of useful energy plotted in Fig. 5.5 (full line) resulted. Summing the fractions at all energies multiplied by the respective intensities, the total useful energy E^{tot} of the spectrum at $\mathbf{p}_i$ is

$$E^{\text{tot}}(\mathbf{p}_i) = \sum_{j=1}^{73} B^{\text{cup}}(E_j, \mathbf{p}_i) \cdot N^{\text{const}}(E_j, \mathbf{p}_i) \cdot E_j^{\text{frac}}(E_j) \tag{5.3}$$

At this point, it is assumed that the corresponding quantities of the "useless" photon energy and the scattered photons lead to a spatially constant film blackening (the effect of this radiation is considered afterwards, see Sect. 5.5). The film density is supposed to be linear to the useful energy. Neglecting the influence of the scanning, the gray value distribution of the digitized x-ray image is the inverted density distribution. Hence, the gray value $I^{\text{synth}}(\mathbf{p}_i)$ at the pixel $\mathbf{p}_i$ of the synthetic x-ray image is described by

$$I^{\text{synth}}(\mathbf{p}_i) = \tau^{\text{synth}} - \lambda^{\text{synth}} \cdot E^{\text{tot}}(\mathbf{p}_i) \,. \tag{5.4}$$

The parameters τ^{synth} and λ^{synth} depend on the x-ray tube current, on the exposure time, on the speed of the film, and on the minimal and the maximal density. They are chosen so that the mean and the standard deviation of the gray values in the synthetic image are the same as in the cup area of the original radiograph. Thus, the intensity range of the synthetic image is adapted without having to consider the above mentioned physical parameters.

With (5.4), a generic model for the image gray values subject to the x-ray intensity is obtained. However, the computation of the sum $E^{\text{tot}}(\mathbf{p}_i)$ during the minimization with respect to the 3D cup parameters is time consuming. In order to find a simpler expression, the total useful energy (5.3) was calculated directly inserting values from $0\,\text{mm}$ to $10\,\text{mm}$ once for the ray length l^{full} and once for l^{grid}. The resulting curves, which are scaled to a maximal value of 1, are plotted in Fig. 5.7. The observed relation between the lengths and the total useful energy could be well approximated by the sum of exponential terms $k_1 \cdot \exp\left(-\mu_1(l^{\text{full}} + 0.35 \cdot l^{\text{grid}})\right) + k_2 \cdot \exp\left(-\mu_2(l^{\text{full}} + 0.35 \cdot l^{\text{grid}})\right)$. The dotted lines in Fig. 5.7
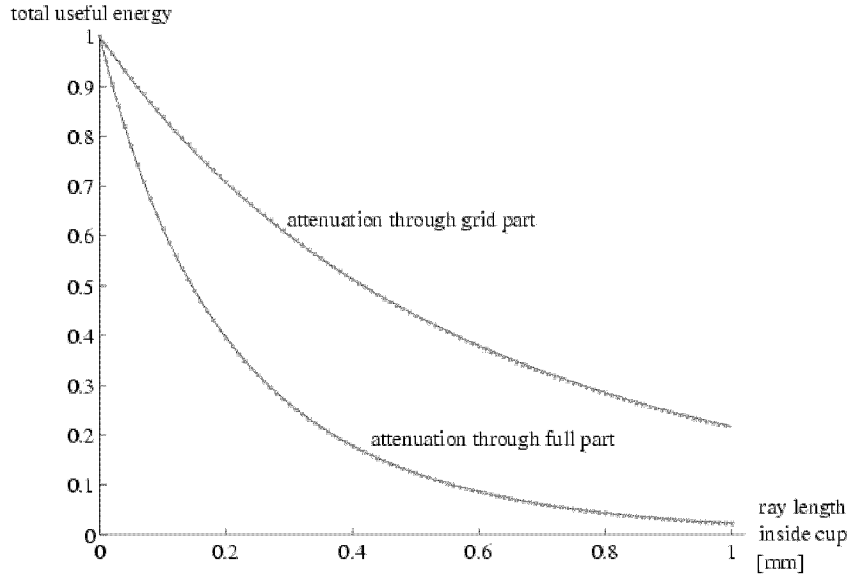
Figure 5.7: *The total useful energy of the radiation scaled to a maximal value of 1 subject to the length of the ray in the full and in the grid part of the cup (solid line). The gray dotted lines show its approximation in terms of exponential functions.*

show this approximation with the parameters $k_1 = 0.3273$, $k_2 = 0.6727$, $\mu_1 = 0.8708$, and $\mu_2 = 0.3376$ found by a least squares fit run in MATLAB [The MathWorks, Inc. 1992]. Thus, the final description of the gray values in the synthetic x-ray image subject to the lengths of the x-rays in the cup is:

$$I^{\text{synth}}(\mathbf{p}_i) = \tau^{\text{synth}} - \lambda^{\text{synth}} \cdot \sum_{n=1}^{2} k_n \cdot \exp\left(-\mu_n(l^{\text{full}}(\mathbf{p}_i) + 0.35 \cdot l^{\text{grid}}(\mathbf{p}_i))\right). \qquad (5.5)$$

Generally, the parameters k_1, k_2, μ_1, and μ_2 need to be estimated considering the x-ray energy spectrum, the attenuation coefficient of the cup, and the screen properties.

5.5   Consideration of the scatter

Comparing the synthesized image of the cup with the original one, it is remarkable that the latter is in some areas darker than it is supposed to be according to the estimated attenuation (compare Fig. 5.8a and Fig. 5.8b). This effect arises from the scatter which was neglected during the synthesis. It influences the determination of the cup's orientation. During the minimization, the cup is rotated so that an overlap in the areas where the original radiograph is darker then the synthetic one is avoided.

In order to illuminate the darkened areas a low frequency adaption is applied. First, an x-ray image of the cup is synthesized using the orientation and position parameters obtained as described in the subsequent paragraph. Then, the synthetic and the original cup image

a   b   c
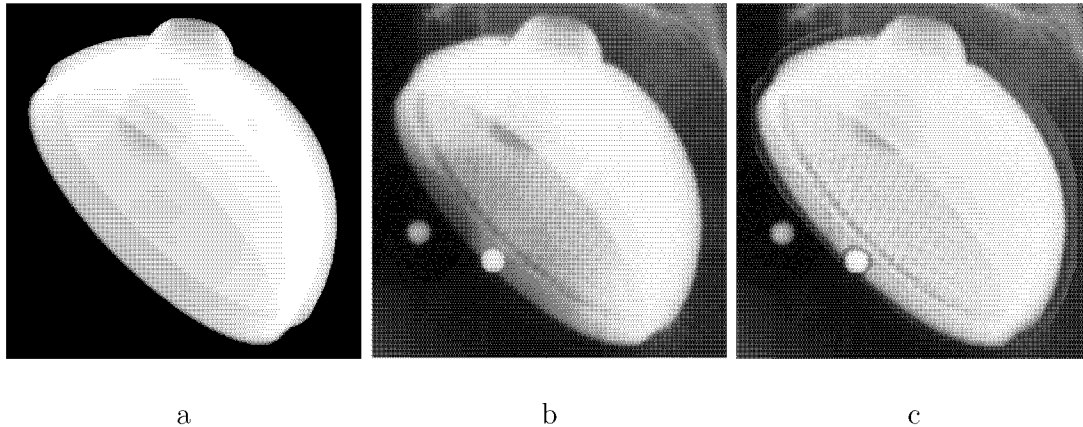
Figure 5.8: *The synthetic image of the cup (a) and the original one before (b) and after (c) the correction for scatter. The original image is a cut of one of the validation radiographs. The superposed calibration sphere was excluded from the ROI.*

are Gaussian filtered with a sigma of 10 pixels (0.85 mm). In doing so, only pixels inside in a region of interest (ROI) are included, which allows for the exclusion of the femoral head and the cup screw. The quotient between the filtered synthetic image and the filtered original one is calculated pixel-wise. Finally, the unfiltered original image is multiplied pixel by pixel by the resulting quotients.

As can be seen in Fig. 5.8c, this low frequency adaption reduces the difference between original and synthesized x-ray image. Still, it depends on the parameters used for the generation of the synthetic image. At the beginning, the use of the initially estimated orientation parameters had been assumed. The cup's image position had been roughly estimated by running Analysis-by-Synthesis, but minimizing only with respect to the position parameters. During the evaluation of the validation radiographs, however, it was found that the influence of the inital orientation on the frequency adaption can not be neglected. As reported in Chapter 7.3.2, the better solution is to estimate first the orientation and position by minimizing the difference of the gradient images (see Sect. 5.8), and then to run the correction for the scatter.

5.6   Parameterization of the cup orientation

The orientation of the cup is represented by three subsequent rotations with the angles θ, ϕ, ψ around three orthogonal axes. This parameterization simplifies the initial estimation of the cup orientation described in the next subsection. Additionally, it allows for the exclusion of rotations which are difficult to estimate from the parameter search. This is mainly the case for the orientation around the cup's polar axis. The rotational axes in the cup's neutral orientation are indicated with $\mathbf{e}_\theta^0$, $\mathbf{e}_\phi^0$, and $\mathbf{e}_\psi^0$. They are parallel to the axes of the x-ray coordinate system (see Fig. 5.9). In the neutral position, the center of the cup's
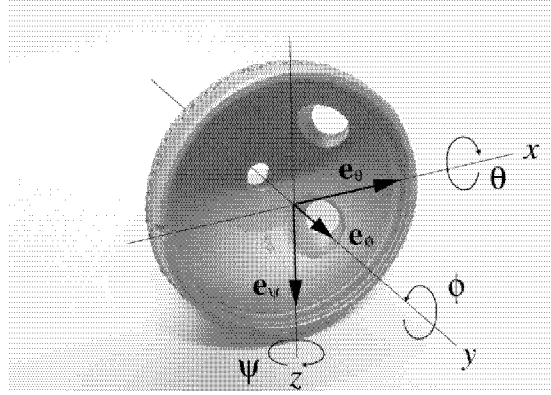
Figure 5.9: *The rotational axes of the cup*

opening plane lies at the origin of the x-ray coordinate system. Throughout the following sections and also in the next chapters, this point will be identified with the cup center. The succession of the rotations is defined as follows: First, the cup is rotated with the angle ψ around $\mathbf{e}_\psi = \mathbf{e}_\psi^0$. At the same time, $\mathbf{e}_\theta^0$ and $\mathbf{e}_\phi^0$ are rotated yielding $\mathbf{e}_\theta$ and $\mathbf{e}_\phi^{\mathrm{tmp}}$. Then, the cup is rotated with the angle θ around $\mathbf{e}_\theta$. Accordingly, the remaining vector $\mathbf{e}_\phi^{\mathrm{tmp}}$ is transformed into $\mathbf{e}_\phi$. Finally, the cup is rotated with the angle ϕ around $\mathbf{e}_\phi$. The transformations $\mathbf{e}_\theta^0 \longrightarrow \mathbf{e}_\theta$, $\mathbf{e}_\phi \longrightarrow \mathbf{e}_\phi^{\mathrm{tmp}}$, and $\mathbf{e}_\phi^{\mathrm{tmp}} \longrightarrow \mathbf{e}_\phi$ are calculated using

$$\begin{aligned}
\mathbf{e}_\theta &= \cos(\psi)\mathbf{e}_\theta^0 + \sin(\psi)\mathbf{e}_\phi^0 \\
\mathbf{e}_\phi^{\mathrm{tmp}} &= \cos(\psi)\mathbf{e}_\phi^0 + \sin(\psi)\mathbf{e}_\theta^0 \\
\mathbf{e}_\phi &= \cos(\theta)\mathbf{e}_\phi^{\mathrm{tmp}} + \sin(\theta)\mathbf{e}_\psi^0 \ .
\end{aligned}$$

The single rotations are expressed by quaternions. The quaternions $\mathbf{q}_\psi$, $\mathbf{q}_\theta$, and $\mathbf{q}_\phi$ of the first, the second, and the third rotation, respectively, have the appearance

$$\begin{aligned}
\mathbf{q}_\psi &= \left(\cos(\psi/2), \sin(\psi/2)\, e_{\psi_x}, \sin(\psi/2)\, e_{\psi_y}, \sin(\psi/2)\, e_{\psi_z} \right) \\
\mathbf{q}_\theta &= \left(\cos(\theta/2), \sin(\theta/2)\, e_{\theta_x}, \sin(\theta/2)\, e_{\theta_y}, \sin(\theta/2)\, e_{\theta_z} \right) \\
\mathbf{q}_\phi &= \left(\cos(\phi/2), \sin(\phi/2)\, e_{\phi_x}, \sin(\phi/2)\, e_{\phi_y}, \sin(\phi/2)\, e_{\phi_z} \right) \ .
\end{aligned}$$

The final orientation is expressed by the product $\mathbf{q}_{\phi\theta\psi} = \mathbf{q}_\phi \mathbf{q}_\theta \mathbf{q}_\psi$ of the three quaternions. The rules for multiplying quaternions are shown in Appendix A. From $\mathbf{q}_{\phi\theta\psi}$, the rotation matrix $\mathbf{R}^{\mathrm{cup}}$ can be calculated as described also in Appendix A.

5.7   Initial estimate of the cup parameters

As the basic form of the cup is a hemisphere, the cup's opening plane appears as an ellipse in the image. The projection of a 3D circle having the same radius r as the cup is interactively fitted to the circumference of this ellipse (see Fig. 5.10). The parameters of
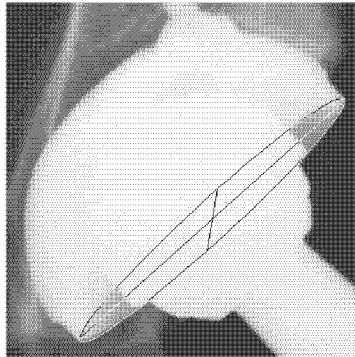
Figure 5.10: *The projection of the 3D circle fitted to the contour of the cup's opening plane. It gives the initial estimate for the 3D position and the orientation parameters ψ and θ.*

the circle virtually situated in the film-focus system give the 3D position of the cup center and the two orientation angles ψ and θ.

The 2D cup center is marked with the left mouse button and the length of the longer semiaxis a of the circumference with the middle one. These quantities define the position parameters. The z-position C_z' of the circle is calculated inserting a, the assumed film–focus distance, and the known radius r in the expression $C_z' = r\sqrt{1 + f^2/a^2}$ adopted from [Russe 1988, page24]. The x-y-position is gained by reprojecting the marked center using C_z' and the assumed values for f and $\mathbf{t}$.

The orientation of the circle is expressed by the first two of the rotations described in the previous subsection. The orientation with respect to $\mathbf{e}_\psi$ is given by the angle of the longer semiaxis with the image horizontal. For estimating θ, the length b of the shorter semiaxis of the elliptical cup circumference is determined with the right mouse button. It is inserted in $b \cdot C_z'/f = r\sin(\theta)$, which approximates the relation between b and the tilt of the cup with respect to $\mathbf{e}_\theta$. The multiplication by C_z'/f in this expression is due to the correction of b for magnification. The angle of the cup's orientation with respect to the polar axis $\mathbf{e}_\phi$ needs to be entered up to now by the user.

If the projection of the circle fits the contour of the opening plane, the cup image is synthesized using the initial estimate. The image is compared to the original radiograph by eye to roughly check the estimate.

5.8   Minimization

The minimization procedure is called passing the intrinsic parameters, the cup's surface data, the initial estimate, the original image, and a region of interest (ROI). The ROI shown in Fig. 5.11 is determined automatically based on the image of the cup synthesized using the initial estimate. It is given by the slightly enlarged image area where the gray values exceed the back ground intensity. From this area, the region of the femoral head and of the screw fixing the implant is excluded. This is necessary, because the positions of
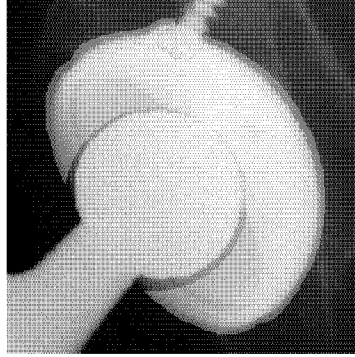
Figure 5.11: *The region of interest defining the pixels which are considered in the minimization.*

these objects with respect to the cup are variable. Up to now, the screw region has to be defined by the user marking it with the mouse. An automatic exclusion would be possible by synthesizing the projection of the screw using its CAD data.

The objective function is the sum of squared residuals as a least squares minimization has been chosen. It is represented by $\mathbf{e}^\mathrm{T}\mathbf{e}$, where $\mathbf{e} = (e_1, ..., e_n)^\mathrm{T}$ is the vector of residuals (n indicates the number of pixels inside the ROI). The residual e_i can either be the difference of the gray value or of the gradient magnitude at the ith pixel in the synthetic image to the corresponding value at this pixel in the original image. The objective function is generally minimized with respect to T_x^cup, T_y^cup, T_z^cup, θ, ϕ, and ψ. The parameters serving for the adaption of the intensity range, τ^synth and λ^synth, are updated after each minimization step. Sometimes, single rotation parameters supposed to be excluded from the search or only the translation supposed to be estimated. This can be the case, for example, if the correction for scatter is applied. Then, the minimization is run with a reduced number of variables and the excluded parameters are set to constants. The function nag_opt_lsq_no_deriv of the NAG library [Numerical Algorithms Group 2000] is used for the minimization. It is based on a combined Gauss-Newton and modified Newton algorithm [Gill *et al.* 1981]. The first derivatives with respect to the parameters are estimated numerically.

If the measure of the discrepancy between synthetic and original image is the difference in the gray values, the residuals have the appearance

$$e_i = I^\mathrm{synth}(\mathbf{p}_i, T_x^\mathrm{cup}, T_y^\mathrm{cup}, T_z^\mathrm{cup}, \theta, \phi, \psi) - I^\mathrm{orig}(\mathbf{p}_i)$$

$$= \tau^\mathrm{synth} - \lambda^\mathrm{synth} \cdot \sum_{n=1}^{2} k_n \cdot \exp\left(-\mu_n(l^\mathrm{full}(\mathbf{p}_i) + 0.35 \cdot l^\mathrm{grid}(\mathbf{p}_i))\right) - I^\mathrm{orig}(\mathbf{p}_i) \, ,$$

where $I^\mathrm{orig}(\mathbf{p}_i)$ indicates the gray value at $\mathbf{p}_i$ in the original image. In the second line of this expression, the approximation (5.5) was inserted. It depends on the position and orientation parameters via the ray lengths l^full and l^grid inside the cup.

The position parameters can be estimated reliably by the comparison of the gray values. The search for θ, ϕ, ψ, however, is affected by the darkening of some image areas caused by

the scatter. The low frequency adaption of the original image using the initial parameters compensates for the effect of the scatter. However, as already mentioned in Sect. 5.5, it implies a dependency on the initial estimate. Therefore, a difference measure independent from the effect of the scatter was tested. Instead of comparing the gray values, the differences of the gradient magnitudes in the original and in the synthetic image were minimized. These magnitudes are given by the length of the vector of the partial derivatives in each pixel. The derivatives were calculated using a finite difference approximation. The spatial derivatives are very sensitive to noise. To reduce the influence of the noise both images were Gaussian filtered with a sigma of 3 pixel (0.25 mm). As reported in Sect. 7.3.2, the comparison of the gradient images provided good results. Its only disadvantage is that it is computationally intensive.

5.9 Magnification, cup center in image, and rotation of cup

The magnification factor of the radiograph is approximated by $g = \frac{f}{T_z^{\mathrm{cup}}}$. The image position **c** of the cup center is obtained by projecting the estimated 3D cup center on the x-ray film plane:

$$\mathbf{c} = f \cdot \left(\frac{T_x^{\mathrm{cup}}}{T_z^{\mathrm{cup}}}, \frac{T_y^{\mathrm{cup}}}{T_z^{\mathrm{cup}}} \right) + \mathbf{t}$$

Additionally, the matrix $\mathbf{R}^{\mathrm{cup}}$ describing the cup orientation with respect to the axes of the x-ray coordinate system is calculated as described in Appendix A using θ, ϕ, ψ. It is used to compute the rotation $\mathbf{R}_{\mathrm{rel}}^{\mathrm{cup}}$ of the cup between two exposures. This rotation was evaluated during the validation of Analysis-by-Synthesis (see Sect. 7.3.2). It is given by $\mathbf{R}_{\mathrm{rel}}^{\mathrm{cup}} = \mathbf{R}_{\mathrm{cmp}}^{\mathrm{cup}} \mathbf{R}_{\mathrm{ref}}^{\mathrm{cup}\mathrm{T}}$, where the matrices $\mathbf{R}_{\mathrm{ref}}^{\mathrm{cup}}$ and $\mathbf{R}_{\mathrm{cmp}}^{\mathrm{cup}}$ represent the cup's orientation in the reference and in the comparison image. The angles of rotation around the axes of the x-ray coordinate system are extracted from the matrix $\mathbf{R}_{\mathrm{rel}}^{\mathrm{cup}}$ as described in Appendix B.

6

Validation experiments

Several series of radiographs were acquired using a standard x-ray system in an orthopaedic hospital. Two series of a calibration box put on the examination table were made (Sect. 6.1). This allowed for testing the calibration of the imaging system and for the assessment of the system's geometrical precision. On the basis of the experience gained through the calibration tests, experiments for testing XIMIT were performed using a specifically designed validation unit (Sect. 6.2). This unit also includes a calibration box, but is additionally equipped with a pelvis phantom and with an artificial hip socket. Again two radiographic series were made. During the acquisition, the variability of the position and orientation of the pelvis at real exposures and the migration of the cup were simulated. The parameters of the translation and rotation and of the cup displacement in the experiments served as ground truth for validating the localization of the cup in 3D and the migration measurement.

6.1   Calibration tests

At the beginning of this work, the reconstruction of the film-focus constellation at exposure was supposed to be relevant for Analysis-by-Synthesis. It was not clear how sensitive the algorithm would be towards the assumed intrinsic parameters. Thus, the calibration procedure introduced in Sect. 5.1 was tested by means of radiographs of a calibration box containing metal spheres at well defined positions. An additional reason for the calibration experiment was given by the fact that the geometrical precision of the x-ray imaging system was completely unknown. This was especially acute for the intended use of conventional x-ray films which are digitized afterwards. An insight in the error introduced by an uneven film or by the scanning could be gained by investigating the variability of the image distances between the spheres of the calibration box. Apart from conventional radiographs, there was the opportunity to test also a semi-digital system where the film is replaced by a phosphor plate. In this system, the digital image is obtained by scanning the phosphor crystals storing the x-ray energy in a specialized machine by means of a laser beam.

a   b
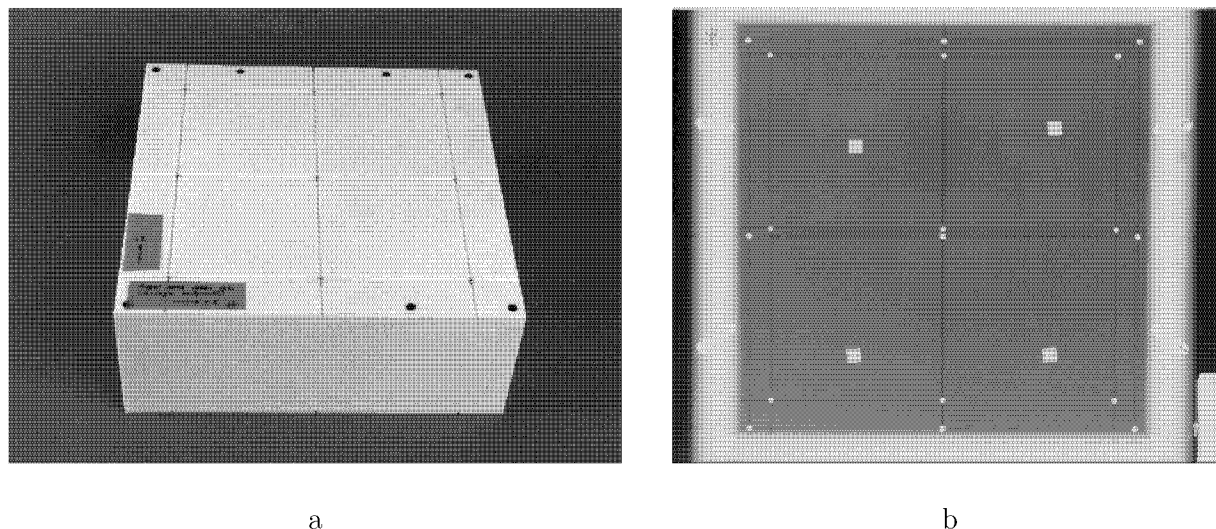
Figure 6.1: *The calibration box (a) and its x-ray image (b).*

6.1.1 Calibration box

The calibration box shown in Fig. 6.1a is a plastic cuboid, whose upper and lower face consist of plates into which 3×3 iron balls with a diameter of 4 mm had been evenly inserted. The relative 3D positions of the spheres were measured with a precision of 10μm. They are represented in the box' coordinate system defined by two balls arbitrarily chosen but lying in the same row. The horizontal and the vertical distances between the spheres are limited by their visibility on the film. The spheres' positions in the plates were chosen under consideration of the film size of 35 cm×43 cm, of the dimensions of the x-ray system, and of the precision in estimating the intrinsic parameters. The optimal box dimensions were found to be 33 cm×33 cm×13 cm, and the spheres were inserted in the plates with a distance of 4 cm from the edge.

6.1.2 X-ray images acquired of the calibration box

X-ray images of the calibration box were made using a clinical x-ray unit with a film–focus distance set to 1200 mm. The x-y-position and the orientation of the digitized x-ray image can vary because of a rotation and translation of the film in the cassette or during the scanning. To allow for the correction for this 2D transformation, four 1 cm×1 cm metal plates visible in Fig. 6.1b were fixed on the examination table.

The calibration box was first roentgenized keeping it in the same position on the examination table, while changing the film cassette after each exposure. Secondly, 10 exposures were made after lifting and putting down again the box. These procedures were done once using conventional x-ray films and once using the semi-digital system. The films were digitized using a VIDAR scanner with a pixel and a gray value resolution of 300 dpi and 12 bit, respectively. The option of scanning each line 4 times was chosen. As the final pixel gray value then is the average of four measurements of the film density, this is supposed to

reduce the noise introduced by the scanner. In case of the semi-digital system, the photon density distribution stored in the phosphor plate was scanned automatically and directly saved as a digital image with 150 dpi and 12 bit.

6.2   Validation of XIMIT

A validation unit was constructed to test the Analysis-by-Synthesis method and the migration measurement. As described in detail in Sect. 6.2.1, it contains a movable pelvis phantom with an artificial hip socket. In the radiographic series made of the unit (see Sect. 6.2.2), the most relevant error entering the clinical migration measurement, the out-of-plane rotation of the pelvis, was reproduced. Additionally, the phantom was shifted in x- and y-direction and a migration of the cup was simulated.

As the absolute position and orientation of the cup in the x-ray system could not be recovered, the parameters of the experimental phantom motion were used as ground truth for validating Analysis-by-Synthesis. The migration measurement was validated i) by investigating the variance of the measured bone–cup distance subject to the pelvis motion ii) by comparing the cup displacement measured in the validation images with the projection of the experimental 3D displacement on the x-y-plane. To obtain a reliable ground truth, the parameters of the rotation, of the translation, and of the migration in the experiments needed to be reconstructed as precisely as possible. This was achieved as explained in detail in Sect. 6.2.3, considering the position and orientation of the validation unit in the x-ray system.

6.2.1   Validation unit

The main part of the validation unit is a real bone pelvis phantom mounted together with a cup on two rotatable plates. These plates were installed on a calibration box which can be translated in medio-lateral and in cranio-caudal direction.

The pelvis phantom consists of macerated bones of a human skeleton. The three bone components, the two hip bones and the sacrum, were joined together with a silicone rubber adhesive. The phantom was installed on the top level plate A (see Fig. 6.2a). It was not fixed in its standard orientation at anterior-posterior exposures, but tilted with respect to medio-lateral as well as to the cranio-caudal axis. This allowed for a simulation of the out-of-plane rotations in both directions. The cup was attached also to plate A through a screw oriented at $11° \pm 5°$ to the horizontal and about $-48° \pm 3°$ to the medio-lateral pelvis axis. It can be moved along the screw having a pitch of 1 mm by turning a knurl.

Plate A can be tilted around an axle lying in medio-lateral direction. It is installed on plate B, which is itself rotatable around an axle in cranio-caudal direction. The tilt is caused by turning screws held by a thread which can be swivelled. They can be identified in Fig. 6.2a by their black knurls. In Fig. 6.3, the geometry of the plates relevant for the reconstruction of the tilt angles is illustrated. The length of b_0 is 8.5 mm in both plates. The one of a is 26.2 cm in plate A and 31.4 cm in plate B. The error in adjusting the angles

a   b
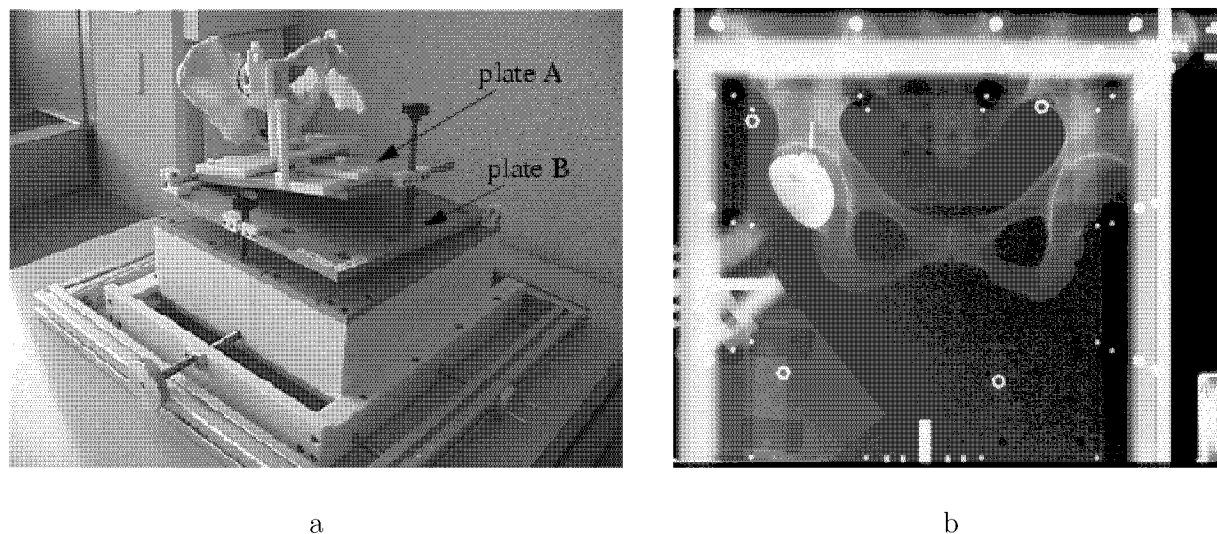
Figure 6.2: *The validation unit (a) and its x-ray image (b).*
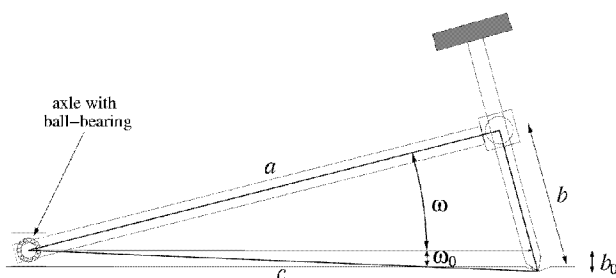
Figure 6.3: *The rotatable plates shown in the cross section.*

is small because of the small screw pitch of h=1 mm and because the axles are hold by ball-bearings minimizing their play. It was estimated to be less than $0.1\,^\circ$. At two arbitrary spots on both axles, the coordinates $\mathbf{P}_{A_1,B_1}$ and $\mathbf{P}_{A_2,B_2}$ of the axial center were measured with a precision of 10μm. This made the exact determination of the direction of the rotational axes possible.

The mountings of the ball-bearings of plate B are fixed on a calibration box having the same dimensions as the one described in Sect. 6.1.1, but bearing on its top and on its bottom 12 iron spheres instead of 9. The positions of the sphere coordinates were measured again with a precision of 10μm. All horizontal plates, both the rotatable and the fixed ones, are made of PEEK ($C_{19}H_{12}O_3$), a radiolucent polymer. The calibration box is held by a set of two frames nested into each other. It can be translated in medio-lateral and in cranio-caudal direction by turning the silver knurls visible in Fig. 6.2a.
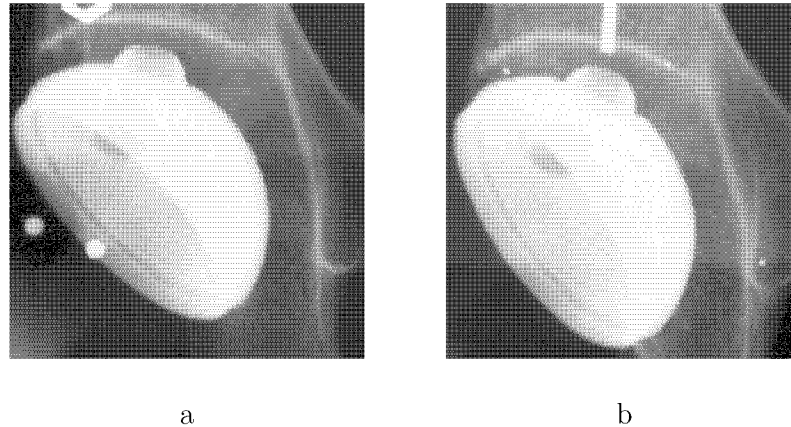
Figure 6.4: *The cup and the teardrop figure in the first image of the series 1 (a) and of the series 2 (b).*

6.2.2   X-ray images acquired of the validation unit

Two series of conventional x-ray images of the phantom were made, one with and one without 3 artificial markers, i.e. tantalum balls with a diameter of 0.8 mm implanted in the bone (see Fig. 6.4b). The balls were placed approximately at the same height above the film plane as the cup center in order to minimize the sensitivity of the marker–cup distance with respect to the pelvis translation and rotation (see Sect. 3.1.2).

Before the validation unit was brought into the x-ray system, four screw-nuts were fixed on the examination table. Their projection was used for the congruent correction for a 2D translation and rotation between two images. The x-ray source was shifted of about 15 cm upwards compared to the standard setting to compensate for the increase of the distance between table and bone caused by the calibration box. The voltage of the x-ray tube was set to 73 kV, and the dose to 7.1 mAs.

The neutral position and orientation of the pelvis in the x-ray system was chosen like the one in standard anterior-posterior pelvis radiographs. The validation unit was put on the examination table so that the phantom was situated approximately in the center of the frames and that the central beam hits the cranial-ventral end of the symphysis pubis as well as the center of the film. The plates were rotated with respect to the horizontal by turning the screw of plate A 30 times and the one of plate B 12 times to neutralize the a priori tilt of the pelvis.

First, the varying position of the pelvis was simulated by an x- and a y-translation of the phantom in approximately 1.5 cm steps in the range of about −3.0 cm to 3.0 cm. After each exposure, a new position was set by turning one of the two knurls of the frames. The amount of translation was determined subsequently by measuring the current distance between the outer or the inner frame and the box using a vernier calliper with a scale division of 0.02 mm.

Afterwards, the variable orientation was simulated keeping the phantom in its neutral position. The phantom was tilted in the range of about −6° to 6° around the medio-

lateral and in the range of about $-2\,^\circ$ to $4\,^\circ$ around the cranio-caudal axis. In the second series, also mixed rotations were chosen by tilting both the lower and the upper plate.

At the end of each series, the migration of the cup was simulated. One to three exposures were made with the cup displaced along its screw in $1\,\mathrm{mm}$ steps.

The x-ray films were scanned with a gray value and a pixel resolution of $12\,\mathrm{bit}$ and $300\,\mathrm{dpi}$, respectively. The same scanner as in the calibration experiments was used, but the option of the line averaging was switched off.

6.2.3 Ground truth

This subsection is about the reconstruction of the phantom motions and of the cup migration in the experiments. For each validation radiograph, the parameters representing the movements in the x-ray coordinate system were determined. They are tabularized at the end of this section and were the ground truth for the results in Sect. 7.3. The translational parameters in the radiographs where the phantom was only shifted were recovered as described in the first of the following paragraphs. The derivation of the ground thruth when tilting the phantom is presented subsequently. It was quite complicated, because the angles and the rotational axes had to be determined, and the resulting rotations needed to be represented in the x-ray coordinate system. Moreover, the additional pelvis translation caused by the tilting of the plates had to be considered. In the last paragraph of this subsection, it is explained how the 2D migration evoked in the experiments is recovered basing on the orientation of the cup screw relative to the calibration box.

The determination of the direction of the translation required the orientation of the validation unit in the x-ray system. The orientation $\mathbf{R}^{\mathrm{calib}}$ of the calibration box in each experimental series was estimated by running the calibration (see Sect. 5.1). Assuming that the frames of the validation unit are parallel to the horizontal axes of the box' coordinate system, the directions of the x- and of the y-translation are given by $\mathbf{R}^{\mathrm{calib}}\,(1,0,0)^{\mathrm{T}}$ and $\mathbf{R}^{\mathrm{calib}}\,(0,1,0)^{\mathrm{T}}$, respectively. This vector in each series was multiplied by the noted amounts of translation. It yielded the values of pelvis displacement listed in the first 10 rows of Tab. 6.1 and in the first 9 ones of Tab. 6.2.

The angles of rotation were determined on the basis of the triangle a, b, c in Fig 6.3. The tilt angle ω_{A} of plate A and respectively ω_{B} of plate B is given by

$$\omega_{\mathrm{A,B}} = \arccos\left(\frac{a^2 + c^2 - b^2}{2ac}\right) - \omega_0 = \arccos\left(\frac{a^2 + c^2 - b^2}{2ac}\right) - \arccos\left(\frac{a^2 + c^2 - b_0^2}{2ac}\right)\ .$$

The lengths of c and b were calculated by $c = \sqrt{a^2 + b_0^2}$ and $b = b_0 + k_{\mathrm{A,B}} \cdot h$, where $k_{\mathrm{A,B}}$ indicates the numbers of screw turns noted during the experiments of plate A or B with respect to the horizontal.

Knowing the angles and the orientation of the calibration box, the rotation $\mathbf{R}_{\mathrm{B}}\,(\Delta\omega_{\mathrm{B}})$ of plate B (the lower plate) represented in the x-ray coordinate system could be reconstructed. The direction $\mathbf{n}_{\mathrm{B}}$ of the rotational axis of plate B is given by multiplying the matrix $\mathbf{R}^{\mathrm{calib}}$ with the vector connecting the measured axial points $\mathbf{P}_{\mathrm{B}_1}$ and $\mathbf{P}_{\mathrm{B}_2}$: $\mathbf{n}_{\mathrm{B}} =$

$\mathbf{R}^{\text{calib}} \left(\mathbf{P}_{\text{B}_2} - \mathbf{P}_{\text{B}_1} \right)$. Indicating with $\Delta\omega_{\text{B}}$ the tilt angle relative to the neutral orientation, the rotation around $\mathbf{n}_{\text{B}}$ is expressed through the quaternion $\left(\cos(\Delta\omega_{\text{B}}/2), \sin(\Delta\omega_{\text{B}}/2) \cdot \mathbf{n}_{\text{B}}^{\text{T}} \right)$. The matrix $\mathbf{R}_{\text{B}} (\Delta\omega_{\text{B}})$ is calculated from this quaternion as described in Appendix A. The direction of the axis $\mathbf{n}_{\text{A}}$ of plate A depends on the orientation of plate B. It is derived by the transformation of the vector $\mathbf{R}^{\text{calib}} \left(\mathbf{P}_{\text{A}_2} - \mathbf{P}_{\text{A}_1} \right)$ connecting the axial points by the matrix $\mathbf{R}_{\text{B}} (\omega_{\text{B}})$:

$$\mathbf{n}_{\text{A}}(\omega_{\text{B}}) = \mathbf{R}_{\text{B}}(\omega_{\text{B}})\mathbf{R}^{\text{calib}} \left(\mathbf{P}_{\text{A}_2} - \mathbf{P}_{\text{A}_1} \right)$$

The relative tilt angle $\Delta\omega_{\text{B}}$ of plate B here needed to be replaced by the absolute one ω_{B}. The matrix $\mathbf{R}_{\text{A}} (\Delta\omega_{\text{A}}, \omega_{\text{B}})$ representing the rotation of plate A with the angle $\Delta\omega_{\text{A}}$ is found analogously to $\mathbf{R}_{\text{B}} (\Delta\omega_{\text{B}})$ using the quaternion $\left(\cos(\Delta\omega_{\text{A}}/2), \sin(\Delta\omega_{\text{A}}/2) \cdot \mathbf{n}_{\text{A}}(\omega_{\text{B}})^{\text{T}} \right)$.

For each of the angles $\Delta\omega_{\text{A}}$ or $\Delta\omega_{\text{B}}$ set in the experiments, the corresponding rotation matrix $\mathbf{R}_{\text{A}} (\Delta\omega_{\text{A}}, \omega_{\text{B}})$, $\mathbf{R}_{\text{B}} (\Delta\omega_{\text{B}})$, or, in case of combined rotations, $\mathbf{R}_{\text{A}} (\Delta\omega_{\text{A}}, \omega_{\text{B}}) \, \mathbf{R}_{\text{B}} (\Delta\omega_{\text{B}})$ is computed. The Euler angles describing the rotation around the axes of the x-ray system are extracted from these matrices using the algorithm described in Appendix B. The resulting angles $\Delta\alpha$, $\Delta\beta$, and $\Delta\gamma$ of rotation around the x-, the y-, and the z-axis, respectively, are enlisted in the columns 5–7 of the Tables 6.1 and 6.2.

The translation caused by tilting the plates depends on the coordinates of the phantom point which is of interest. The only point where absolute coordinates can be obtained is the cup center. Its neutral position $\mathbf{T}_0^{\text{cup}}$ could be estimated by applying Analysis-by-Synthesis in the radiographs where the phantom was not moved and the cup was not displaced. The general position $\mathbf{T}^{\text{cup}}$ is given by the transformation of $\mathbf{T}_0^{\text{cup}}$ at a rotation of plate B followed by a rotation of plate A:

$$\mathbf{T}^{\text{cup}} = \mathbf{R}_{\text{A}}(\Delta\omega_{\text{A}}, \omega_{\text{B}}) \left[\mathbf{R}_{\text{B}}(\Delta\omega_{\text{B}}) \left(\mathbf{T}_0^{\text{cup}} - \mathbf{Z}_{\text{B}} \right) + \mathbf{Z}_{\text{B}} - \mathbf{Z}_{\text{A}}(\omega_{\text{B}}) \right] + \mathbf{Z}_{\text{A}}(\omega_{\text{B}}) \qquad (6.1)$$

In this expression $\mathbf{Z}_{\text{A}}$ and $\mathbf{Z}_{\text{B}}$ are the centers of rotation at a tilt of plate A and of plate B, respectively. The transformation could mostly be simplified because in the majority of the cases only one plate was rotated. The rotational centers were set to the points $\mathbf{P}_{\text{B}_1}$ and $\mathbf{P}_{\text{A}_1}$. Representing $\mathbf{P}_{\text{B}_1}$ in the x-ray coordinate system the rotational center of the lower plate is $\mathbf{Z}_{\text{B}} = \mathbf{R}^{\text{calib}}\mathbf{P}_{\text{B}_1} + \mathbf{T}^{\text{calib}}$. Determining $\mathbf{Z}_{\text{A}}$ required the transformation of the axial point caused by the tilt of the plate B: $\mathbf{Z}_{\text{A}}(\omega_{\text{B}}) = \mathbf{R}_{\text{B}}(\omega_{\text{B}}) \left(\mathbf{R}^{\text{calib}}\mathbf{P}_{\text{A}_1} + \mathbf{T}^{\text{calib}} - \mathbf{Z}_{\text{B}} \right) + \mathbf{Z}_{\text{B}}$. The values of $\mathbf{T}^{\text{cup}} - \mathbf{T}_0^{\text{cup}}$ resulting from the insertion of the previous paragraph's rotation matrices in (6.1) are listed in the rows 11 to 22 of Tab. 6.1 and 10 to 28 of Tab. 6.2.

The amount of migration in the experimental series is given by the product between the pitch of the cup screw and the noted number of turns of its knurl. The play of the screw thread is negligible, because the knurl had been turned in the experiments only in one direction. The direction of the migration relative to the calibration box corresponds to the one of the cup screw and is $(\cos(11°)\cos(-48°), \cos(11°)\sin(-48°), \sin(11°))^{\text{T}}$. Considering the orientation of the calibration box and the tilt angles ω_{A} and ω_{B} with respect to the horizontal, this vector represented in the x-ray coordinate system is

$$\mathbf{R}_{\text{A}}(\omega_{\text{A}}, \omega_{\text{B}})\mathbf{R}_{\text{B}}(\omega_{\text{B}})\mathbf{R}^{\text{calib}} \begin{pmatrix} \cos(11°)\cos(-48°) \\ \cos(11°)\sin(-48°) \\ \sin(11°) \end{pmatrix} . \qquad (6.2)$$

In XIMIT, the migration parallel to the film plane is observed. Hence, only the x- and the y-component of the migration are important. Multiplying these components as given by (6.2) by the amounts of displacement yielded the values for the 2D migration Δd_{ml} and Δd_{cc} enlisted in the last rows of the Tables 6.1 and 6.2. In the evaluation of the validation images, the relevant quantity is the magnitude $|\Delta \mathbf{d}| = \sqrt{\Delta d_{\mathrm{ml}}^2 + \Delta d_{\mathrm{cc}}^2}$ of the 2D migration (see Sect. 7.3.3). To estimate the reliability of the ground truth, the maximal error of this magnitude computed with the values in the Tables 6.1 and 6.2 was estimated. It was found to be 3% by inserting the error bounds of 5° and 3° of the orientation of the cup screw (see Sect. 6.2.1) in the expression (6.2).

image number	ΔT_x	ΔT_y [mm]	ΔT_z	$\Delta\alpha$	$\Delta\beta$ [°]	$\Delta\gamma$	Δd_{ml}	Δd_{cc} [mm]
1	0	0	0	0	0	0	—	—
2	−12.0	0.1	0.0	0	0	0	—	—
3	0.2	0.0	0.0	0	0	0	—	—
4	12.0	0.1	0.0	0	0	0	—	—
5	24.0	−0.1	0.0	0	0	0	—	—
6	−0.2	−29.7	0.1	0	0	0	—	—
7	−0.1	−14.7	0.1	0	0	0	—	—
8	0.0	0.0	0.0	0	0	0	—	—
9	0.1	15.3	−0.1	0	0	0	—	—
10	0.2	30.0	−0.1	0	0	0	—	—
11	0.3	−9.1	−7.6	−4.4	0.0	−0.2	—	—
12	0.1	−4.5	−3.9	−2.2	0.0	−0.1	—	—
13	−0.1	4.3	4.0	2.2	0.0	0.1	—	—
14	−0.2	6.4	6.1	3.3	0.0	0.1	—	—
15	−0.4	10.5	10.4	5.5	0.0	0.2	—	—
16	−0.4	12.5	12.6	6.6	0.1	0.3	—	—
17	8.6	−0.1	−14.3	0.0	−3.3	0.0	—	—
18	5.7	−0.1	−9.6	0.0	−2.2	0.0	—	—
19	2.9	−0.1	−4.8	0.0	−1.1	0.0	—	—
20	0.2	0.0	0.0	0.0	−0.0	0.0	—	—
21	−2.4	0.0	4.9	0.0	1.1	0.0	—	—
22	−4.9	0.0	9.8	0.0	2.2	0.0	—	—
23	0.2	0.0	0.0	0.0	0.0	0.0	0.64	−0.70
24	0.2	0.0	0.0	0.0	0.0	0.0	1.29	−1.40
25	0.2	0.0	0.0	0.0	0.0	0.0	1.93	−2.11

Table 6.1: *The pelvis translation ΔT_x, ΔT_y, ΔT_z and rotation $\Delta\alpha$, $\Delta\beta$, $\Delta\gamma$ with respect to the x-, the y-, and the z-axis, respectively, as well as the 2D components Δd_{ml} and Δd_{cc} of the migration simulated in the first validation experiment.*

image number	ΔT_x	ΔT_y [mm]	ΔT_z	$\Delta\alpha$	$\Delta\beta$ [°]	$\Delta\gamma$	Δd_{ml}	Δd_{cc} [mm]
1	0	0	0	0	0	0	—	—
2	−29.6	0.0	0.1	0	0	0	—	—
3	−15.0	0.1	0.0	0	0	0	—	—
4	0.4	0.1	0.0	0	0	0	—	—
5	15.1	0.1	0.0	0	0	0	—	—
6	30.0	0.1	−0.1	0	0	0	—	—
7	0.1	−37.4	0.1	0	0	0	—	—
8	0.0	0.1	0.0	0	0	0	—	—
9	−0.1	37.3	−0.1	0	0	0	—	—
10	0.9	−15.1	−13.3	−6.6	0.0	−0.2	—	—
11	0.7	−9.8	−9.0	−4.4	0.0	−0.2	—	—
12	0.6	−4.8	−4.6	−2.2	0.0	−0.1	—	—
13	0.4	0.1	0.0	0.0	0.0	0.0	—	—
14	0.2	4.8	4.8	2.2	0.0	0.1	—	—
15	0.0	9.2	9.7	4.4	0.0	0.2	—	—
16	−0.2	13.5	14.9	6.6	0.0	0.3	—	—
17	12.2	0.1	−17.1	0.0	−4.4	0.0	—	—
18	9.1	0.1	−12.9	0.0	−3.3	0.0	—	—
19	6.1	0.1	−8.7	0.0	−2.2	0.0	—	—
20	3.2	0.1	−4.4	0.0	−1.1	0.0	—	—
21	0.4	0.1	0.0	0.0	0.0	0.0	—	—
22	−2.4	0.1	4.4	0.0	1.1	0.0	—	—
23	−5.0	0.1	8.9	0.0	2.2	0.0	—	—
24	−2.4	4.7	9.2	2.2	1.1	0.1	—	—
25	−5.0	4.7	13.7	2.2	2.2	0.1	—	—
26	−2.2	−4.8	−0.2	−2.2	1.1	−0.1	—	—
27	3.5	−4.8	−9.0	−2.2	−1.1	−0.1	—	—
28	3.5	−4.8	−9.0	−2.2	−1.1	−0.1	0.64	−0.69

Table 6.2: *The pelvis translation ΔT_x, ΔT_y, ΔT_z and rotation $\Delta\alpha$, $\Delta\beta$, $\Delta\gamma$ with respect to the x-, the y-, and the z-axis, respectively, as well as the 2D components Δd_{ml} and Δd_{cc} of the migration simulated in the second validation experiment. Determining Δd_{ml} and Δd_{cc} the orientation of the images 27 and 28 is considered.*

7

Results

7.1 Theoretical error of the measured migration

The theoretical precision in the migration measurement using XIMIT was determined according to the scheme introduced in Chapter 2. The general clinical precision was estimated as described in Sect. 7.1.1 by assuming the same parameters as in Chapter 2. The resulting standard deviations allow for a comparison of XIMIT with the previous methods analysed. Apart from that, the error found by the evaluation of the validation images was exactly predicted theoretically as described in Sect. 7.1.2. This made a cross-validation between experimental findings and theoretical considerations possible.

7.1.1 Comparison with previous methods

Like in the analysis of the previous methods, the error was estimated by applying the principle of error propagation to the analytical expression of the measured bone–cup distance $\mathbf{d}$. In the expression (3.1), the magnification factor g in (3.1) was replaced by $\frac{f+\delta f}{C_z+\delta f}+\delta g$, where δg indicates the deviation of the estimated magnification from the real one. Additionally, the expressions for $\mathbf{c}$ and $\mathbf{m}_k$ ($k=1,...,3$) as given by (2.2) and (2.3) and the parameters of the measurement were inserted in the formula for the bone–cup distance. The parameters representing the 3D coordinates of anatomical points such as the bony landmarks were set to the points measured in the Visible Human Female and listed in Tab. 2.1. The cup center was assumed to be the center of the femoral head and the film–focus distance was set to $f = 1100\,\mathrm{mm}$. According to Chapter 2, the partial derivatives of $\mathbf{d}$ with respect to the variables $\delta\alpha, \delta\beta, \delta\gamma, \delta T_x, ...$ representing the sources of error were calculated. They gave the coefficients in the following sums of error components representing the overall standard deviation of the bone–cup distance (derivatives below 10^{-5} are not listed):

$$
\begin{aligned}
\sigma_{d_{\mathrm{ml}}}^2 = \; & (0.01806\sigma_{\delta\alpha})^2 + (-0.00836\sigma_{\delta\beta})^2 + (-0.00278\sigma_{\delta\gamma})^2 + \\
& (0.00226\sigma_{\delta T_x})^2 + (-0.00020\sigma_{\delta T_z})^2 + (-0.00020\sigma_{\delta f})^2 + \\
& (0.79091\sigma_{\delta c_x})^2 + (0.10222\sigma_{\delta m_{1y}})^2 + (-0.10222\sigma_{\delta m_{2y}})^2 + \\
& (-0.79091\sigma_{\delta m_{3x}})^2 + (26.4722\sigma_{\delta g})^2
\end{aligned}
$$

$$
\begin{aligned}
\sigma^2_{d_{\mathrm{cc}}} \;=\; & (0.04433\sigma_{\delta\alpha})^2 + (-0.01749\sigma_{\delta\beta})^2 + (0.00264\sigma_{\delta T_y})^2 + \\
& (0.00001\sigma_{\delta T_z})^2 + (0.00001\sigma_{\delta f})^2 + (0.79091\sigma_{\delta c_y})^2 + \\
& (0.24247\sigma_{\delta m_{1y}})^2 + (-0.24247\sigma_{\delta m_{2y}})^2 + (-0.79091\sigma_{\delta m_{3y}})^2 + \\
& (11.16058\sigma_{\delta g})^2
\end{aligned}
$$

$$(7.1)$$

Regarding the magnitudes of the coefficients, the sources of error having a significant influence are: the pelvis rotation around the x-axis, the errors in locating the cup and the bone reference point, the error of the correction for magnification, and less importantly also the rotation around the y-axis and the variable pelvis x-y-position.

The calculation of the final error of the measured bone–cup distance required the magnitude of the entering errors represented by the $\sigma_{\delta\alpha}, \ldots$ in (7.1). The variability of the pelvis position and orientation and of the film–focus distance is independent from the measurement. The related standard deviations $\sigma_{\delta\alpha,\delta\beta,\delta\gamma}$, $\sigma_{\delta T_x,\delta T_y,\delta T_z}$, and $\sigma_{\delta f}$ were set to values listed in Sect. 2.6.2 and used in the analysis of the previous methods. The cup and the bony landmarks, however, are located in XIMIT more precisely than before. Also the magnification is estimated more reliably. Accordingly, the related standard deviations were updated and set to the ones found by evaluating the validation radiographs and presented in Sect. 7.3: $\sigma_{\delta c_{x,y}} = 0.03\,\mathrm{mm}$ and $\sigma_{\delta g} = 0.0026$ (Tab. 7.7), $\sigma_{\delta m_{1,2\,x,y}} = 0.06\,\mathrm{mm}$ (Tab. 7.4), $\sigma_{\delta m_{3\,x}} = 0.29\,\mathrm{mm}$ and $\sigma_{\delta m_{3\,y}} = 0.32\,\mathrm{mm}$ (Tab. 7.5). In case of an external marker the latters are reduced to $\sigma_{\delta m_{3\,x}} = \sigma_{\delta m_{3\,y}} = 0.05\,\mathrm{mm}$ (Tab. 7.4). Inserting these numbers in the expression (7.1), the theoretical error $(\sigma_{d_{\mathrm{ml}}}, \sigma_{d_{\mathrm{cc}}})$ of the measured bone–cup distance resulted to be $(0.26\,\mathrm{mm}, 0.32\,\mathrm{mm})$ if only natural bony landmarks are used and $(0.12\,\mathrm{mm}, 0.20\,\mathrm{mm})$ if a marker is implanted. Assuming that the implant displacement is determined by subtracting the bone–cup distances measured in two random radiographs, these results needed to be multiplied by $\sqrt{2}$ yielding the $(0.36\,\mathrm{mm}, 0.46\,\mathrm{mm})$ and $(0.18\,\mathrm{mm}, 0.29\,\mathrm{mm})$ for the error of the migration in the both cases. Comparing these errors to the ones found in the previous methods, which reach from $0.63\,\mathrm{mm}$ to $3.1\,\mathrm{mm}$ (see Sect. 2.6), a definite precision improvement using XIMIT can be stated.

For the sake of completeness, the use of a bone reference $\mathbf{m}_3$ which can be located in the image more precisely than the teardrop figure was theoretically tested. The error of the bone–cup distance was calculated again replacing the teardrop figure point by (i) the most medial and (ii) the most caudal point of the ipsilateral foramen obturatorum. The coordinates of the most medial point were also adopted from Chapter 2. The standard deviation $\sqrt{2}(\sigma_{d_{\mathrm{ml}}}, \sigma_{d_{\mathrm{cc}}})$ of the migration resulted to be $(0.67\,\mathrm{mm}, 0.86\,\mathrm{mm})$ in case (i) and $(1.22\,\mathrm{mm}, 2.17\,\mathrm{mm})$ in case (ii). Hence, the measurement error is increased significantly, even though the error in locating the bone reference was assumed to be reduced to $\sigma_{\delta m_{3\,x,y}} = 0.06\,\mathrm{mm}$ taking for both foramen points the value in Tab. 7.4.

7.1.2   Theoretical error in the validation experiments

During the acquisition of the validation radiographs, the pelvis movements having a noticeable influence on the migration measurement were simulated. The phantom was successively translated in x-direction, translated in y-direction, tilted around the medio-lateral axis, and tilted around the cranio-caudal one. In reality, these motions between two exposures occur all at the same time. Evaluating the experimental measurements, the variances of the measured bone–cup distance at the individual motions were calculated and added up to realistically estimate the overall error (see Sect. 7.3.3). This error estimation was reproduced theoretically.

To compute the variances of d_{ml} and d_{cc} at the individual motions, the images of the series were grouped according to the phantom movement. The four groups labeled with the roman numbers I–IV contain the images 2–5, 6–10, 11–16, and 17–22 in the first series and 2–6, 7–9, 10–16, 17–23 in the second. Indicating the variances within the groups with $\sigma_{d_{\mathrm{ml}}}^{\mathrm{I-IV}}$ and $\sigma_{d_{\mathrm{cc}}}^{\mathrm{I-IV}}$, the theoretical representation of the overall variance in Sect. 7.3.3 is

$$\sigma_{d_{\mathrm{ml}}}^{\mathrm{I}}{}^{2} + \sigma_{d_{\mathrm{ml}}}^{\mathrm{II}}{}^{2} + \sigma_{d_{\mathrm{ml}}}^{\mathrm{III}}{}^{2} + \sigma_{d_{\mathrm{ml}}}^{\mathrm{IV}}{}^{2} \qquad \text{and} \qquad \sigma_{d_{\mathrm{cc}}}^{\mathrm{I}}{}^{2} + \sigma_{d_{\mathrm{cc}}}^{\mathrm{II}}{}^{2} + \sigma_{d_{\mathrm{cc}}}^{\mathrm{III}}{}^{2} + \sigma_{d_{\mathrm{cc}}}^{\mathrm{IV}}{}^{2}. \tag{7.2}$$

These sums of variances were brought into the form of the expressions (7.1), which are the sums of the components of the entering errors. Each component consists of the product between the partial derivative of $\mathbf{d}$ with respect to the error variable and the standard deviation of the variable. The partial derivatives were calculated once more taking the experimental setup into account. While doing so, the anatomical points of the Visible Human Female inserted in the previous subsection were replaced by the corresponding ones in the phantom.

In the following paragraph, it is described how the formulation of (7.2) as sums of error components was derived. The overall standard deviations, which were calculated using the experimental ground truth, are reported subsequently. Afterwards, it is described how the required phantom points were determined. The resulting partial derivatives and the theoretically predicted values for $\sigma_{d_{\mathrm{ml}}}$ and $\sigma_{d_{\mathrm{cc}}}$ in the experiments are presented at the end of this subsection.

The errors entering the measurement of d_{ml} and d_{cc} in the validation radiographs were divided into the ones which remain the same in the four groups of images and the ones which depend on the pelvis motion. The error in locating the cup center and the one in estimating the magnification belong to the constant ones. Also the error in locating $\mathbf{m}_1$ and $\mathbf{m}_2$ was assumed to be constant, because the lower contours of the foramina obturatoria are relatively independent from the pelvis position and orientation. For these errors the notation $\sigma_{\delta c_{x,y}}$, $\sigma_{\delta m_{1,2\,x,y}}$, and $\sigma_{\delta g}$ was kept. The error in locating the teardrop figure and the standard deviations of the phantom position and orientation are motion dependent. For the former, the notation $\sigma_{\delta m_{3\,x}}^{\mathrm{I-IV}}$ and $\sigma_{\delta m_{3\,y}}^{\mathrm{I-IV}}$ was introduced. The latter were indicated with $\sigma_{\Delta T_{x,y,z}}^{\mathrm{I-IV}}$, $\sigma_{\Delta\alpha,\Delta\beta,\Delta\gamma}^{\mathrm{I-IV}}$. Each of them is different from zero only in 1–2 groups of images as the phantom motions had been performed one after the other (e.g., $\sigma_{\Delta\alpha,\Delta\beta,\Delta\gamma}^{\mathrm{I-II}}$ is zero).

With this notation, the variance of d_{ml} at a pelvis rotation around the medio-lateral axis (group III), for example, is

$$\sigma_{d_{\mathrm{ml}}}^{\mathrm{III}\ 2} = \left(\frac{\partial d_{\mathrm{ml}}}{\partial \delta\alpha}\sigma_{\Delta\alpha}^{\mathrm{III}}\right)^2 + \left(\frac{\partial d_{\mathrm{ml}}}{\partial \delta T_y}\sigma_{\Delta T_y}^{\mathrm{III}}\right)^2 + \left(\frac{\partial d_{\mathrm{ml}}}{\partial \delta T_z}\sigma_{\Delta T_z}^{\mathrm{III}}\right)^2 + \left(\frac{\partial d_{\mathrm{ml}}}{\partial \delta c_{x,y}}\sigma_{\delta c_{x,y}}\right)^2 + \qquad (7.3)$$
$$\left(\frac{\partial d_{\mathrm{ml}}}{\partial \delta m_{1,2\,x,y}}\sigma_{\delta m_{1,2\,x,y}}\right)^2 + \left(\frac{\partial d_{\mathrm{ml}}}{\partial \delta m_{3\,x}}\sigma_{\delta m_{3\,x}}^{\mathrm{III}}\right)^2 + \left(\frac{\partial d_{\mathrm{ml}}}{\partial \delta m_{3\,y}}\sigma_{\delta m_{3\,y}}^{\mathrm{III}}\right)^2 + \left(\frac{\partial d_{\mathrm{ml}}}{\partial \delta g}\sigma_{\delta g}\right)^2 .$$

Summing the theoretical variances of the four groups all having the form of (7.3), the following expression shown for simplicity only for the error of the medio-lateral bone–cup distance resulted:

$$\sigma_{d_{\mathrm{ml}}}^{\mathrm{I}\ 2} + \sigma_{d_{\mathrm{ml}}}^{\mathrm{II}\ 2} + \sigma_{d_{\mathrm{ml}}}^{\mathrm{III}\ 2} + \sigma_{d_{\mathrm{ml}}}^{\mathrm{IV}\ 2} =$$
$$\left(\frac{\partial d_{\mathrm{ml}}}{\partial \delta\alpha}\sigma_{\Delta\alpha}^{\mathrm{III}}\right)^2 + \left(\frac{\partial d_{\mathrm{ml}}}{\partial \delta\beta}\sigma_{\Delta\beta}^{\mathrm{IV}}\right)^2 + \left(\frac{\partial d_{\mathrm{ml}}}{\partial \delta T_x}\sqrt{\sigma_{\Delta T_x}^{\mathrm{I}\ 2} + \sigma_{\Delta T_x}^{\mathrm{IV}\ 2}}\right)^2 +$$
$$\left(\frac{\partial d_{\mathrm{ml}}}{\partial \delta T_y}\sqrt{\sigma_{\Delta T_y}^{\mathrm{II}\ 2} + \sigma_{\Delta T_y}^{\mathrm{III}\ 2}}\right)^2 + \left(\frac{\partial d_{\mathrm{ml}}}{\partial \delta T_z}\sqrt{\sigma_{\Delta T_z}^{\mathrm{III}\ 2} + \sigma_{\Delta T_z}^{\mathrm{IV}\ 2}}\right)^2 + \left(\frac{\partial d_{\mathrm{ml}}}{\partial \delta c_{x,y}}\,2\sigma_{\delta c_{x,y}}\right)^2 +$$
$$\left(\frac{\partial d_{\mathrm{ml}}}{\partial \delta m_{1,2\,x,y}}\,2\sigma_{\delta m_{1,2\,x,y}}\right)^2 + \left(\frac{\partial d_{\mathrm{ml}}}{\partial \delta m_{3x}}\sqrt{\sigma_{\delta m_{3x}}^{\mathrm{I}\ 2} + \sigma_{\delta m_{3x}}^{\mathrm{II}\ 2} + \sigma_{\delta m_{3x}}^{\mathrm{III}\ 2} + \sigma_{\delta m_{3x}}^{\mathrm{IV}\ 2}}\right)^2 +$$
$$\left(\frac{\partial d_{\mathrm{ml}}}{\partial \delta m_{3y}}\sqrt{\sigma_{\delta m_{3y}}^{\mathrm{I}\ 2} + \sigma_{\delta m_{3y}}^{\mathrm{II}\ 2} + \sigma_{\delta m_{3y}}^{\mathrm{III}\ 2} + \sigma_{\delta m_{3y}}^{\mathrm{IV}\ 2}}\right)^2 + \left(\frac{\partial d_{\mathrm{ml}}}{\partial \delta g}\,2\sigma_{\delta g}\right)^2$$

It corresponds to the expressions (7.1), but instead of the $\sigma_{\delta\alpha}, \sigma_{\delta\beta}, \ldots$ the summed standard deviations of the variables in the four groups needed to be inserted. The ones of the pelvis translation and rotation were obtained by adding the standard deviations within each group of the ΔT_x, ΔT_y, ΔT_z, $\Delta\alpha$, $\Delta\beta$ as given by the Tables 6.1 and 6.2 (motions below 0.5 mm or 0.4° were neglected). The $\sqrt{\sigma_{\Delta T_x}^{\mathrm{I}\ 2} + \sigma_{\Delta T_x}^{\mathrm{IV}\ 2}}$, $\sqrt{\sigma_{\Delta T_y}^{\mathrm{II}\ 2} + \sigma_{\Delta T_y}^{\mathrm{III}\ 2}}$, and $\sqrt{\sigma_{\Delta T_z}^{\mathrm{III}\ 2} + \sigma_{\Delta T_z}^{\mathrm{IV}\ 2}}$ were found to be, respectively, 20.3 mm, 27.2 mm, and 12.4 mm in series 1 and 23.6 mm, 37.3 mm, and 13.8 mm in series 2. The standard deviations $\sigma_{\Delta\alpha}^{\mathrm{III}}$ and $\sigma_{\Delta\beta}^{\mathrm{IV}}$ of the rotation resulted to have the respective values 3.9° and 2.0° in first series and 4.7° and 2.4° in the second. The quantity $\sqrt{\sigma_{\delta m3x,y}^{\mathrm{I}\ 2} + \sigma_{\delta m3x,y}^{\mathrm{II}\ 2} + \sigma_{\delta m3x,y}^{\mathrm{III}\ 2} + \sigma_{\delta m3x,y}^{\mathrm{IV}\ 2}}$ reflects the general error in locating the teardrop figure taking the variable pelvis position and orientation into account (see Sect. 7.3.1). The x- and the y-component of this error were found to be 0.29 mm and 0.32 mm, respectively (Tab. 7.5). For the standard deviations of the motion independent variables the values for $\sigma_{\delta c_{x,y}}$, $\sigma_{\delta m_{1,2\,x,y}}$, and $\sigma_{\delta g}$ in the previous subsection were adopted. If using a marker as bone reference point $\mathbf{m}_3$, the error of the teardrop figure was replaced by $2\sigma_{\delta m_{3\,x,y}} = 2 \cdot 0.05$, where the latter number was again adopted from Sect. 7.1.

The phantom points required for the calculation of the partial derivatives were determined by means of the radiographs of the second validation series. The phantom position and orientation was for simplicity assumed to be the same in both experiments. The slight difference between the two series had no significant effect on the error estimate. The coordinates $\mathbf{C}_0$ of the cup center were set to the mean of its neutral position $\mathbf{T}_0^{\mathrm{cup}}$ found

point of the pelvis	x[mm]	y[mm]	z[mm]
cup center $\mathbf{C}_0$	-83.9	-32.0	1035.9
point of left foraminum obturatorium ($\mathbf{M}_{10}$)	-43.6	6.2	1058.1
point of right foraminum obturatorium ($\mathbf{M}_{20}$)	56.0	8.8	1051.1
caudal point of teardrop figure ($\mathbf{M}_{30}$)	-47.5	-21.3	1036.8
rotational center $\mathbf{Z}$	145.8	-154.6	1175.6

Table 7.1: *Anatomical points in the pelvis phantom*

by applying Analysis-by-Synthesis in the radiographs $1, 4, 8, 13$, and 21. The 3D positions $\mathbf{M}_{10,20,30}$ of the teardrop figure and of the foramina obturatoria were estimated by the reprojection of their coordinates $\mathbf{m}_{1,2,3}$ in the first image:

$$
\mathbf{M}_{10,20,30} = \begin{pmatrix} m_{1,2,3\,x} \cdot M_{10,20,30_z}/f \\ m_{1,2,3\,y} \cdot M_{10,20,30_z}/f \\ M_{10,20,30_z} \end{pmatrix}
$$

For the film–focus distance, the value $(f_x + f_y)/2 = 1406\,\text{mm}$ in the second series found by calibration was taken. The z-coordinates were obtained by adding the ventral-dorsal distances between the bony landmarks and the cup center measured in the phantom using a ruler.

When determinating the ground truth, the two different centers of rotation $\mathbf{Z}_\text{A}(\omega_\text{B})$ and $\mathbf{Z}_\text{B}$ were introduced according to which one of the two plates of the validation unit had been tilted (see Sect. 6.2.3). For the theoretical error determination according to the scheme in Chapter 2, however, the coordinates of one general rotational center were required. A rotational center being valid for both of the experimental rotations was constructed by assuming that if the plates are in the horizontal, i.e. $\omega_\text{A,B} = 0$, their axes of rotation lie in the same x-y-plane and have the z-coordinate $(Z_{\text{A}_z}(0) + Z_{\text{B}_z})/2$. Then, z-coordinates of the rotational axes $\mathbf{n}_\text{A}(\omega_\text{B})$ and $\mathbf{n}_\text{B}$ of Sect. 6.2.3 are zero. The rotational centers can be shifted along $\mathbf{n}_\text{A}$ and $\mathbf{n}_\text{B}$ because only the components perpendicular to the axis play a role. They meet in the intersection point of the axes given by

$$
\begin{pmatrix} Z_{\text{B}_x} \\ Z_{\text{B}_y} \\ \frac{(Z_{\text{A}_z}(0)+Z_{\text{B}_z})}{2} \end{pmatrix} + \frac{n_{\text{A}_x}(0)\left(Z_{\text{B}_y} - Z_{\text{A}_y}(0)\right) - n_{\text{A}_y}(0)\left(Z_{\text{B}_x} - Z_{\text{A}_x}(0)\right)}{n_{\text{B}_x} n_{\text{A}_y} - n_{\text{A}_x} n_{\text{B}_y}} \begin{pmatrix} n_{\text{B}_x} \\ n_{\text{B}_y} \\ 0 \end{pmatrix} .
$$

This point could be used as general rotational center, because it is not affected by a tilt of the lower plate. Its coordinates as well as the ones of the cup center and of the bony landmarks in the phantom are listed in Tab. 7.1.

These coordinates were inserted in the analytical expression of the measured bone–cup distance and the partial derivatives of $\mathbf{d}$ with respect to the error variables were calculated once more. Although the phantom points significantly differ from the ones measured in the

	$\mathbf{m}_3$	$\sigma_{d_{\mathrm{ml}}}$	$\sigma_{d_{\mathrm{cc}}}$	[mm]
series 1	teardrop figure	0.27	0.37	
series 2	teardrop figure	0.28	0.41	
	medial marker	0.20	0.35	

Table 7.2: *The theoretical prediction of the error in measuring the bone–cup distance* $(d_{\mathrm{ml}}, d_{\mathrm{cc}})$ *found in the validation experiments and reported in Sect. 7.3.3*

.

Visible Human Female, the derivatives related to the relevant sources of error were found to be comparable to the ones in (7.1):

$$
\begin{aligned}
\sigma^2_{d_{\mathrm{ml}}} \;=\; & (-0.02136\sigma_{\delta\alpha})^2 + (0.01025\sigma_{\delta\beta})^2 + (0.00080\sigma_{\delta\gamma})^2 + \\
& (0.00089\sigma_{\delta T_x})^2 + (-0.00063\sigma_{\delta T_y})^2 + (0.00005\sigma_{\delta T_z})^2 + \\
& (0.00005\sigma_{\delta f})^2 + (0.73662\sigma_{\delta c_x})^2 + (0.01959\sigma_{\delta c_y})^2 + \\
& (-0.00195\sigma_{\delta m_{1x}})^2 + (0.07332\sigma_{\delta m_{1y}})^2 + (0.00195\sigma_{\delta m_{2x}})^2 + \\
& (-0.07332\sigma_{\delta m_{2y}})^2 + (-0.73662\sigma_{\delta m_{3x}})^2 + (-0.01959\sigma_{\delta m_{3y}})^2 + \\
& (-27.05314\sigma_{\delta g})^2 \\
\sigma^2_{d_{\mathrm{cc}}} \;=\; & (0.06422\sigma_{\delta\alpha})^2 + (0.01855\sigma_{\delta\beta})^2 + (-0.00819\sigma_{\delta\gamma})^2 + \\
& (-0.00009\sigma_{\delta T_x})^2 + (0.00331\sigma_{\delta T_y})^2 + (-0.01959\sigma_{\delta c_x})^2 + \\
& (0.73662\sigma_{\delta c_y})^2 + (0.00735\sigma_{\delta m_{1x}})^2 + (-0.27621\sigma_{\delta m_{1y}})^2 + \\
& (-0.00735\sigma_{\delta m_{2x}})^2 + (0.27621\sigma_{\delta m_{2y}})^2 + (0.01959\sigma_{\delta m_{3x}})^2 + \\
& (-0.73662\sigma_{\delta m_{3y}})^2 + (7.18155\sigma_{\delta g})^2
\end{aligned}
$$

$$(7.4)$$

In these expressions, the summed standard deviations were inserted. As the film–focus distance was not changed during the experiments and the in-plane rotation was negligible, $\sigma_{\delta f}$ and $\sigma_{\delta\gamma}$ were set to zero. The resulting overall errors of d_{ml} and d_{cc} for both series are shown in Tab. 7.2.

7.2   Results of the calibration tests

The radiographs of the two calibration series were evaluated using the graphical user interface described in Sect. 5.1. Three tests reported in the following subsections were performed. Before running the calibration procedure, the images had been warped with a congruent transformation reflecting their translation and rotation with respect to a reference image, which was chosen to be the first one of each of the series. The transformation was found using the image coordinates of the squares fixed to the x-ray table. These coordinates were determined by least squares matching (Chapter 4).

7.2.1   Reproducibility in matching the calibration spheres

In one radiograph of the conventional and in one of the semi-digital series, the calibration procedure was repeated 10 times. Each time, the initial image positions of the spheres of the calibration box were newly estimated, and the final coordinates of the sphere centers and the found intrinsic parameters were saved.

In the conventional x-ray image, the standard deviations of the x- and of the y-coordinates of the spheres resulted to lie between $10^{-5}\,\mu$m and $0.015\,\mu$m with a mean value of $0.0036\,\mu$m. Because of these small errors, also the estimated intrinsic parameters have a little variance. The standard deviations σ_{t_x} and σ_{t_y} of the film x-y-position were found to be $0.18\,\mu$m and $0.10\,\mu$m, respectively. The ones of the two components of the film–focus distance resulted to be $\sigma_{f_x} = 0.27\,\mu$m and $\sigma_{f_y} = 0.24\,\mu$m.

In the case of the semi-digital radiograph, the errors of the spheres' x-y-coordinates were increased to a range of $0.001\,\mu$m–$0.078\,\mu$m and a mean value of $0.023\,\mu$m, because of the lower pixel resolution. Correspondingly, the variances of the intrinsic parameters are also higher. The standard deviations of t_x, t_y, f_x, and f_y were found to be $0.8\,\mu$m, $0.9\,\mu$m, $1.4\,\mu$m, and $1.3\,\mu$m, respectively.

7.2.2   Geometrical precision of the imaging system

The geometrical precision was estimated by running the calibration procedure in the ten images where the calibration box was not moved and by computing the theoretically constant image distances between the spheres. The precision in x-direction (in y-direction) was assessed by calculating the standard deviation of the distance $|\mathbf{s}_k - \mathbf{s}_l|$ between the sphere k and the sphere l lying in the same horizontal (vertical) row. Analysing the distance instead of directly the coordinates excludes the influence of an inaccurate correction for the variable image orientation.

The results are listed in Tab. 7.3, where the first two colums contain the absolute mean differences $\overline{|s_{k_x} - s_{l_x}|}$ and $\overline{|s_{k_y} - s_{l_y}|}$ in the x- and the y-coordinates of the sphere couple k, l. The standard deviations $\sigma_{|\mathbf{s}_k - \mathbf{s}_l|}$ and the relative errors $\sigma_{|\mathbf{s}_k - \mathbf{s}_l|}/\overline{|\mathbf{s}_k - \mathbf{s}_l|}$ of the spheres' distances are listed for the images acquired by means of the conventional and of the semi-digital system. Concerning the former, the great variability in x-direction of $0.13\,$mm per $100\,$mm is remarkable. It may partly result from the chosen option mentioned in Sect.6.1 of scanning each line several times. In the x-ray images of the validation unit, which were scanned without setting this option, the distance of about $100\,$mm between the teardrop figures could be measured with a reproducibility of 35μm–54μm. The assumption that the great error in x-direction has its origin in the scanning is confirmed by the numbers in the columns 5–6 of Tab. 7.3. They represent the standard deviations of the sphere distances measured in the images of the same x-ray film scanned 10 times. In x-direction, a mean geometrical error of $80\,\mu$m per $100\,$mm was found, which is $8\times$ the one in y-direction. The precision in y-direction in the semi-digital radiographs corresponds to the one in the conventional x-ray images. Also there, the error in x-direction is greater, which may be a sign for an irregular transport of the phosphor plate in the scanning device.

$\overline{\|s_{k_x}-s_{l_x}\|}$ [mm]	$\overline{\|s_{k_y}-s_{l_y}\|}$ [mm]	conventional films		same film scanned 10×		semi-digital system	
		$\sigma_{\|s_k-s_l\|}$ [μm]	$\frac{\sigma_{\|s_k-s_l\|}}{\|s_k-s_l\|}$ %	$\sigma_{\|s_k-s_l\|}$ [μm]	$\frac{\sigma_{\|s_k-s_l\|}}{\|s_k-s_l\|}$ %	$\sigma_{\|s_k-s_l\|}$ [μm]	$\frac{\sigma_{\|s_k-s_l\|}}{\|s_k-s_l\|}$ %
298	0	363	0.12	227	0.08	199	0.07
299	0	358	0.12	218	0.07	133	0.04
300	1	353	0.12	217	0.07	58	0.02
265	0	363	0.14	227	0.09	156	0.06
266	0	349	0.13	212	0.08	109	0.04
267	0	338	0.13	203	0.08	47	0.02
mean value			0.13		0.08		0.04
0	299	107	0.04	44	0.02	63	0.02
1	299	73	0.03	42	0.01	91	0.03
2	299	70	0.02	20	0.01	51	0.02
0	266	66	0.03	33	0.01	55	0.02
1	266	52	0.02	34	0.01	84	0.03
2	266	47	0.02	21	0.01	36	0.01
mean value			0.03		0.01		0.02

Table 7.3: *Variance of the image distances between the calibration spheres at a constant position of the calibration box.*

The distance between teardrop figure and cup center lies at about 40 mm. According to the results shown in Tab. 7.3, its standard deviation is in the worst case 0.05 mm. Hence, despite the relatively high variability of the image distances in x-direction, the tested x-ray systems allow for measuring cup displacements in radiographs with sub-millimeter precision. The distortion of the x-ray images caused, for example, by an uneven film plane, can be neglected.

The estimation of the intrinsic parameters strongly depends on the error of the 2D coordinates. This is reflected by the results of the calibration. Using the conventional system, the standard deviations of the intrinsic parameters were found to be $\sigma_{t_x} = 2.44$ mm, $\sigma_{t_y} = 0.75$ mm, $\sigma_{f_x} = 2.42$ mm and $\sigma_{f_y} = 1.33$ mm. There were reduced to $\sigma_{t_x} = 0.75$ mm, $\sigma_{t_y} = 0.34$ mm, $\sigma_{f_x} = 0.52$ mm and $\sigma_{f_y} = 0.56$ mm, however, using the semi-digital system with the higher geometrical precision.

7.2.3 Overall error of the calibration

The precision of the calibration considering all geometrical influences in x-ray imaging was assessed using the radiographs where the calibration box had been lifted and put back on the examination table. This precision estimation is not directly relevant for the migration measurement using XIMIT, but is generally of interest if dealing with absolute positions and orientations of objects in the x-ray unit. In this work, this was the case when calculating the groundtruth in the validation experiments. The resulting standard

deviations of the intrinsic parameters were found to be $\sigma_{t_x} = 0.83\,\text{mm}$, $\sigma_{t_y} = 0.40\,\text{mm}$, $\sigma_{f_x} = 1.09\,\text{mm}$, $\sigma_{f_y} = 0.10\,\text{mm}$ for the semi-digital and $\sigma_{t_x} = 1.77\,\text{mm}$, $\sigma_{t_y} = 2.01\,\text{mm}$, $\sigma_{f_x} = 1.42\,\text{mm}$, $\sigma_{f_y} = 1.25\,\text{mm}$ for the conventional system. They are a bit greater than the ones in the preceding subsection because now also the errors of the 3D coordinates of the calibration spheres play a role.

7.3   Results of the experimental validation of XIMIT

The radiographs of the two series of the validation unit were corrected for an image translation and rotation using the calibration interface. The calibration was run in the images where all spheres were visible. The corrected images were evaluated using the user interface described in Sect. 3.2. The intrinsic paramaters were set to the estimated values $f_x = 1337.4\,\text{mm}$, $f_y = 1346.3\,\text{mm}$, $t_x = -4.9\,\text{mm}$, and $t_y = -1.7\,\text{mm}$ in the first series and $f_x = 1400.3\,\text{mm}$, $f_y = 1411.3\,\text{mm}$, $t_x = -8.0\,\text{mm}$, and $t_y = 9.5\,\text{mm}$ in the second (the differing values for f_x and f_y indicate that the pixel size at the scanning in x-direction and in y-direction is not the same). The least squares matching was tested as reported in the next subsection, by locating the bony landmarks in several images and observing the variability of the distances between them. The performance of Analysis-by-Synthesis was investigated by comparing the estimated translation and rotation of the cup between the radiographs to the ground truth (Sect. 7.3.2). The overall variance of the migration measurement was assessed as described in Sect.7.3.3, by calculating the standard deviation of the bone–cup distance $(d_{\text{ml}}, d_{\text{cc}})$ subject to the pelvis orientation and position. Additionally, the accuracy of XIMIT, i.e. the deviation of the measured migration from its expected value given by the ground truth, is determined.

7.3.1   Precision in locating the bony landmarks

The localization of the bony landmarks depends on the alteration of their projection at an orientation and position change of the pelvis. It is difficult to determine its precision because no exact ground truth is available. At a pelvis rotation or translation, the absolute image positions of the landmarks and the 2D distances between them vary unpredictably, depending on their 3D position that is only known roughly. Nevertheless, the error under optimal conditions could be estimated by determining the standard deviation of the distances between two comparable bony landmarks in the images with no phantom motion. The matching of the teardrop figure, the most delicate of the landmarks, could be investigated also at variable orientation and positions with the aid of the tantalum ball implanted in the area of this bony structure.

The points of the foramina obturatoria defining the image coordinate system, the most caudal points of the right and the left teardrop figure, and in series 2 also the center of the lateral and of the medial tantalum ball (see Fig. 6.4b) were matched using templates like the ones shown in the Figures 4.2, 4.5a, and 4.6. Only the radiographs were evaluated where the pelvis bone is at its neutral position and orientation. These are the images 1, 3, 8, 20, 23, 24,

bony landmark	error of localization ($\sigma_{\delta m_{k\,x,y}}$) [$\mu$m]	
	series 1	series 2
points of foramina obturatoria ($\mathbf{m}_{1,2}$)	61	41
caudal point of teardrop figure ($\mathbf{m}_3$)	54	35
center of tantalum ball ($\mathbf{m}_3$)	—	45

Table 7.4: *Maximal precision in locating the bony landmarks. It would be valid at a constant orientation and position of the pelvis in the x-ray system.*

and 25 of the first series and the images $1, 4, 8, 13,$ and 21 of the second. The absolute distances between the points of the three couples of landmarks were calculated to yield a quantity independent from the phantom's and the radiograph's exact position and from the image orientation possibly varying because of an inaccurate 2D correction. It is assumed that the matching error is the same for both the left and the right point of each couple as well as for the x- and the y-coordinates. Then, given the standard deviation $\sigma_{|\mathbf{m}_2 - \mathbf{m}_1|}$ of the distance between the landmarks $\mathbf{m}_1$ and $\mathbf{m}_2$, for example, the one of the individual coordinates is $\sigma_{\delta m_{1\,x}} = \sigma_{\delta m_{2\,x}} = \sigma_{\delta m_{1\,y}} = \sigma_{\delta m_{2\,y}} = \sigma_{|\mathbf{m}_2 - \mathbf{m}_1|}/\sqrt{2}$.

The results of this evaluation are shown in Tab. 7.4. The listed errors in locating the points of foramina obturatoria and the tantalum balls may have the same order of magnitude as the real ones. The matching of these landmarks is quite robust because they are only slightly altered through pelvis motions. Anyway, concerning $\mathbf{m}_1$ and $\mathbf{m}_2$ a greater error would hardly be noticeable in the migration assessment. According to the corresponding partial derivatives in (7.1) or (7.4), the coordinate of these landmarks only have a secondary effect on the measured bone–cup distance.

The position of the teardrop figure, however, is important for the migration and is more variable than the standard deviations in Tab. 7.4 would indicate. The tantalum ball implanted in the area of the bony structures forming this landmark is a good reference point for estimating the real variability. It can be located precisely and it has a similar z-position as the most caudal point of the teardrop figure, which will be the only point identified with the bone reference point $\mathbf{m}_3$ in the following paragraphs. Hence, the position of $\mathbf{m}_3$ relative to the marker should be quite unsensitive towards pelvis motions and towards the 2D correction of the image. The teardrop figure was matched trying three different templates. Template A shown in Fig. 7.1A includes the whole bony structure superposed by the ilio-ischial line. Template B (Fig. 7.1B) was defined under exclusion of this line at all pelvis positions and orientations as described in Sect. 4.3.1. In template C, the upper part of the teardrop figure was omitted (see Fig. 7.1C).

The distances in x- and in y-direction between the external marker and $\mathbf{m}_3$ in all images of the second series are plotted in Fig. 7.2. In the plots, the respective distance in the reference image is subtracted. Using template A, the matching was unreliable at pelvis rotations and even at great medio-lateral translations affecting the position of th ilio-ischial line. In the cases where the plot range is exceeded, the mismatch of the teardrop figure was obvious, and a definition of $\mathbf{m}_3$ by simple mouse clicking would have led to a better localization.
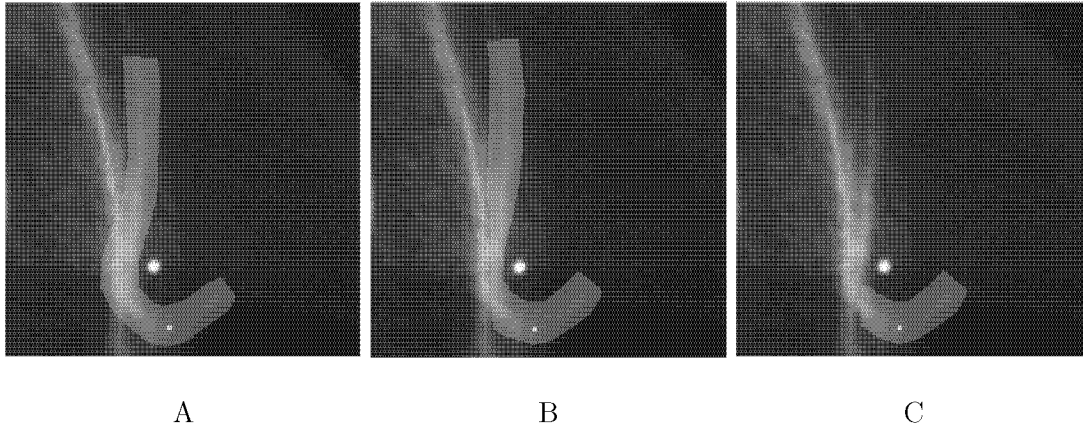
Figure 7.1: *The tested templates A, B, and C of the teardrop figure.*
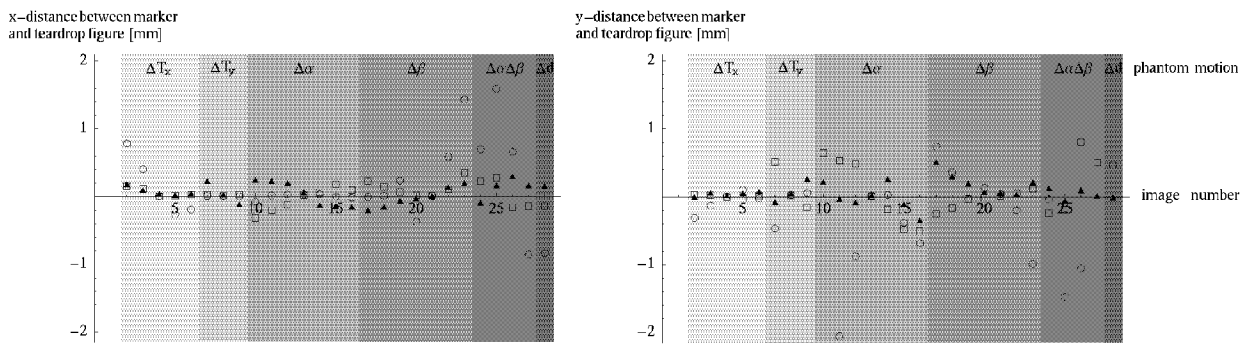

Figure 7.2: *The distance in x- and in y-direction between the center of the medial marker and the teardrop figure landmark in the images 2–28. The coordinate difference between these points in the reference image was subtracted. The spheres, the triangles, and the squares show the distances determined using template A, template B, and template C, respectively.*

Excluding the ilio-ischial line (template B) improved the localization of the bone reference point. The matching failed in none of the images, and the x-coordinate of the teardrop figure landmark was quite stable, even at great rotations of the phantom from the neutral orientation. Still, the y-distance of $\mathbf{m}_3$ to the marker heavily deviated from its reference value at the extreme orientations set at the exposures 16 and 17. Cutting also the upper part as in template C deteriorated again the matching. The y-position then was very sensitive towards a rotation around the medio-lateral axis and also towards a translation in cranio-caudal direction.

The overall variance was determined similarly to the one of the migration (see the Sections 7.1.2 and 7.3.3). The images were grouped according to the motion simulated, and within each group the standard deviation of the x- and the y-distance between external marker and teardrop figure landmark was calculated. The squares of these standard deviations were added up, and the variance in locating the marker, which is the square of the error in

template	$\sigma_{\delta m_{3\,x}}$	$\sigma_{\delta m_{3\,y}}$ [mm]
A (complete teardrop figure)	0.71	1.43
B (ilio-ischial line excluded)	0.29	0.32
C (ilio-ischial line and upper part excluded)	0.22	0.61

Table 7.5: *Precision in locating the teardrop figure if considering the influence of the variable pelvis orientation and position in the x-ray system on the figure's appearance in the radiograph.*

Tab. 7.4, was deducted from the obtained error sums. The roots of the resulting values gave the standard deviations shown in Tab. 7.5. The distances between marker and teardrop figure point at combined rotations were neglected. Including them in the error calculation would have implied a double consideration of the error at the respective rotation angles.

7.3.2   Precision of Analysis-by-Synthesis

The position and orientation of the cup in the x-ray system during the experiments was recovered by applying the Analysis-by-Synthesis method to the validation radiographs. Four different versions of this method were tested:

1. The implant's 3D parameters were estimated by minimizing the differences between the gray values in the original and the ones in the synthetic x-ray image of the cup.

2. Before the full parameter search was started, the correction for scatter was run. The low frequency range of the original image was adapted to the one of the synthetic image calculated using the initial orientation estimate (see Sect. 5.5).

3. Instead of the differences in the gray values, the ones in the gradients of original and synthetic image were minimized. This version was also applied omitting the 2D correction of the image for translation and rotation and setting the intrinsic parameters to their nominal values $t_x = t_y = 0\,\text{mm}$, and $f_x = f_y = 1350\,\text{mm}$ in series 1 and $f_x = f_y = 1400\,\text{mm}$ in series 2.

4. The low frequency range of the original image was adapted to the one of the synthetic image generated using the parameter estimate of matching the gradient images. Afterwards again the gray value differences were minimized.

In the following paragraphs, first the position and then the orientation estimation is discussed. As the real absolute parameters in the x-ray system were unknown, the translation and the rotation between two exposures was determined from the estimated parameters and compared with the ground truth reported in Sect. 6.2.3. The performance of the method was tested only taking into account the standard deviations from ground truth. The mean deviation from ground truth was assumed to be insignificant, because it depends on the absolute parameters estimated in the reference image. As they can differ from their real values within the intervalls of their standard deviation, a mean deviation from ground
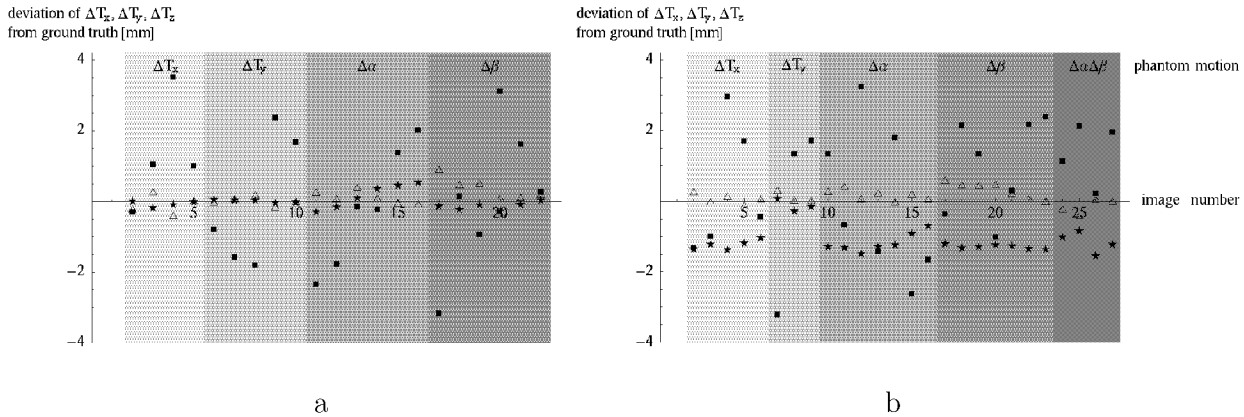
deviation of $\Delta T_x, \Delta T_y, \Delta T_z$
from ground truth [mm]

deviation of $\Delta T_x, \Delta T_y, \Delta T_z$
from ground truth [mm]

a   b

Figure 7.3: *The Figures a and b show the deviation from ground truth of the translation parameters ΔT_x (triangles), ΔT_y (stars), and ΔT_z (squares) estimated in series 1 and series 2, respectively, using the Analysis-by-Synthesis version 4.*

truth results which has no meaning for the accuracy of the method. Morerover, during the evaluation of the validation images the suspicion arose that in the experiments the neutral position and orientation of the phantom was not always exactly adjusted (see the following paragraph). This implies a possible systematical error of the ground truth of all the subsequent exposures and would lead to an additionally bias of the mean deviation.

The position estimates did not significantly differ between the versions, which, however, had a great influence on the orientation estimation. The reason for this is that changing the orientation parameters the cup center stays at the same position because of the symmetrical shape of the socket. Only the estimation of the z-coordinate could be slightly improved by the refinement of Analysis-by-Synthesis. In Fig. 7.3, the deviations from ground truth of the cup translation estimated using the Analysis-by-Synthesis version 4 are plotted. The standard deviations of these differences using all versions are shown in Tab. 7.6[1].

For several reasons great errors in estimating ΔT_x and ΔT_y resulted:

- The absolute image coordinates differ from radiograph to radiograph of up to 0.15 mm because of the limited precision of the 2D correction.

- During the experiments, unnoticed displacements of the calibration box, on which the phantom is installed, had occurred. This is indicated by a displacement of the calibration spheres in the image relative to the frame of the validation unit. It was found that in the second series, for example, where the estimated y-translation lies in most of the images about 1 mm below its nominal value (see Fig. 7.3b), the calibration box had been shifted from the neutral position of the same amount. The images 6–9, where the deviation from ground truth was found to be small, had in fact been

---

[1]The values for $\sigma_{\Delta T_x}$ and $\sigma_{\Delta T_y}$ when omitting the 2D correction of the radiographs are not meaningful. The film–focus constellation is incorrectly assumed to be constant. A shift of the film in the cassette or in the scanner, which can reach up to 1 cm, is compensated during the parameter estimation by a virtual translation of the cup. This has no influence on the measurement of images distances, but falsifies the estimation of ΔT_x and ΔT_y.

parameter search	2D correction and calibration	series 1			series 2			
		$\sigma_{\Delta T_x}$	$\sigma_{\Delta T_y}$	$\sigma_{\Delta T_z}$	$\sigma_{\Delta T_x}$	$\sigma_{\Delta T_y}$	$\sigma_{\Delta T_z}$	$[mm]$
version 1	yes	0.31	0.21	2.52	0.25	0.46	2.12	
version 2	yes	0.29	0.27	2.18	0.23	0.47	2.22	
version 3	yes	0.28	0.21	1.88	0.22	0.45	1.69	
	no	(4.49)	(1.37)	2.11	(3.96)	(2.15)	1.63	
version 4	yes	0.28	0.22	1.82	0.23	0.45	1.72	

Table 7.6: *The standard deviations $\sigma_{\Delta T_x}$, $\sigma_{\Delta T_y}$, and $\sigma_{\Delta T_z}$ from ground truth of the cup translation in x-, in y-, and in z-direction using the different Analysis-by-Synthesis versions.*

acquired at the beginning of the experiment. Hence, it is possible that after the y-translation the box had not exactly been shifted back to its neutral position.

- The ground truth in the case of tilting the phantom seems to be incorrect. This is indicated by the systematical deviation of ΔT_y in the images 11–16 of the first or of ΔT_x in the images 17–23 of the second series. The reason for this can be that the estimated absolute cup position $\mathbf{T}_0^{\text{cup}}$ in the x-ray system at the neutral orientation and position of the phantom, which was required for the determination of the ground truth, differed from the real position. The absolute coordinates depend on the assumed film–focus constellation, which can only be recovered with a precision in the millimeter range as reported in Sect. 7.2.3. The error of the z-coordinate is additionally increased, because it can principally not be estimated exactly at a great focus–object distance such as in anterior-posterior radiographs. At the same time it is the coordinate having the greatest influence on the calculation of the rotational ground truth.

Thus, the reported standard deviations do not reflect the precision of Analysis-by-Synthesis. Only the determined variance of the translation in z-direction may be meaningful, because the suspected errors of the ground truth are smaller than the expected error bounds of the z-position. Trusting the found standard deviations of $\sigma_{\Delta T_z} = 1.82\,\text{mm}$ in the first and $\sigma_{\Delta T_z} = 1.72\,\text{mm}$ in the second series, the precision in estimating the magnification factor $g = f/T_z^{\text{cup}}$ was assessed. This precision is important for the migration measurement. Using the principle of error propagation, the derivative of g with respect to the cup's z-coordinate needed to be calculated. The derivative with respect to f is zero as the film–focus distance is constant. For T_z^{cup}, the mean of the cup's z-coordinates estimated in all images where the phantom is at its neutral orientation ($\Delta T_z = 0$) was inserted. The values resulting for the standard deviation $\sigma_{\delta g} = \sigma_{\Delta T_z} \cdot f/C_z^2$ in the two series are shown in Tab. 7.7. To get a more realistic insight in the precision in locating the cup, its position relative to the most caudal point of the teardrop figure in the radiographs of the second series

parameter search	2D correction and calibration	series 1		series 2	
		$\sigma_{\delta c_{x,y}}$ [μm]	$\sigma_{\delta g}$	$\sigma_{\delta c_{x,y}}$ [μm]	$\sigma_{\delta g}$
version 1	yes	—	0.00352	30	0.00280
version 3	no	—	0.00295	24	0.00215
version 4	yes	—	0.00255	38	0.00228

Table 7.7: *The error of the cup's image coordinates ($\sigma_{\delta c_{x,y}}$) and of the magnification factor ($\sigma_{\delta g}$) if using the Analysis-by-Synthesis versions 1, 3, and 4. The former could only be estimated in the second series, because one of the tantalum balls implanted after the first experiment was taken as reference point.*

was analysed. The distance $|\mathbf{c} - \mathbf{m}_3|$ between cup and $\mathbf{m}_3$ was determined in the images of neutral position and orientation. From the variance $\sigma^2_{|\mathbf{c}-\mathbf{m}_3|}$ of this distance, the one in locating the teardrop figure point (see Tab 7.4) was subtracted. Assuming that the x- and the y-component have the same error, the standard deviation of the cup's image coordinates is $\sigma_{\delta c_{x,y}} = \sqrt{\sigma^2_{|\mathbf{c}-\mathbf{m}_3|} - \sigma^2_{\delta m_{3\,x,y}}}$. This quantity was determined using the Analysis-by-Synthesis versions 1, 3, and 4. The results also listed in Tab. 7.7 confirm that the localization of the cup performs better than predicted by the comparison with ground truth. They standard deviations in the second row show that the precision is independent from the assumed intrinsic parameters and the exact position and orientation of the film. Again, an improvement of the localization when using the refined version could not be observed.

The orientation parameters searched for in the minimization are the angles of rotation θ, ϕ, ψ around the axes $\mathbf{e}_\theta$, $\mathbf{e}_\phi$, $\mathbf{e}_\psi$ fixed to the cup and defined as described in Sect. 5.6. The errors of these angles together with difference image of original and synthetic radiograph give qualitative information about the problems of finding the right orientation of the cup. For the quantitative analysis, the rotation matrix representing the orientation in the x-ray coordinate system was calculated from θ, ϕ, ψ. The parameters of this matrix are the Euler angles. The angles of the orientation with respect to the x- and to the y-axis are both correlated with θ and ϕ, whereas the one of the orientation with respect to the z-axis mainly depends on ψ. The change of the orientation in the x-ray system is expressed by the angles $\Delta\alpha$, $\Delta\beta$, $\Delta\gamma$ of rotation around the x-, the y-, and the z-axis, respectively, between comparison and reference image. These angles determined in each radiograph were compared to the ground truth in the Tables 6.1 and 6.2. Their standard deviations from ground truth reflect the precision in estimating the rotation of the cup between two exposures.

Using the first version of Analysis-by-Synthesis, the darkening of the lower left part of the cup opening by the scatter prevented the minimization from finding the right orientation of the cup with respect to $\mathbf{e}_\theta$. This becomes clear regarding Fig. 7.4a and b and the standard deviation of the corresponding rotation angle θ in the images with no phantom rotation. This standard deviation was found to be 0.66° in the first series and 0.39° in the second. As
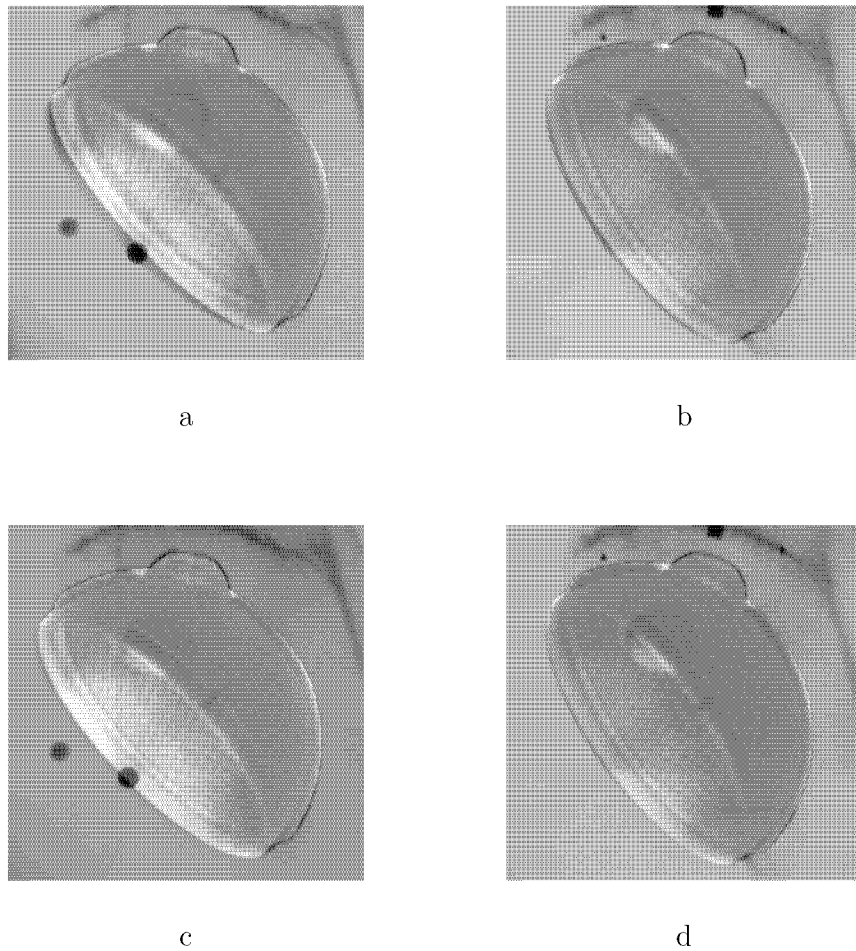
a b

c d

Figure 7.4: *The difference between the synthetic x-ray image of the cup and the original one in the reference radiographs of the first and the second series. In the Figures a and b, the cup's position and orientation parameters were estimated by comparing the gray values, in the Figures c and d by mimizing the differences in the gradient magnitudes.*

both $\Delta\alpha$ and $\Delta\beta$ depend on θ, great errors resulted for these angles, whereas the rotation with respect to the z-axis could be recovered quite precisely. These results become obvious by the deviations of $\Delta\alpha$, $\Delta\beta$, $\Delta\gamma$ from ground truth plotted in the Figures 7.5a and 7.6a and by the standard deviations of the plotted values listed in Tab. 7.8.

As expected, the low frequency correction neutralized the effect of the scatter. It reduced the standard deviation of θ in the images at neutral orientation to 0.13° in both series without a noticeable deterioration of the estimation of ϕ. Accordingly, the deviations of the Euler angles $\Delta\alpha$ and $\Delta\beta$ from ground were decreased. This is shown by the plots in the Figures 7.5b and 7.6b. The correction for the scatter, however, caused a dependency of the parameter estimation from the initial estimate, as the required synthetic image is generated using the initial orientation parameters. This was probably the reason for an increased standard deviation from ground truth of $\Delta\gamma$. The resulting standard deviations of all three rotations are again listed in Tab. 7.8.

The comparison of the gradient images blinds out the low frequency differences between original and synthetic image. Additionally, it emphasizes the geometrical information. Therefore, the edges of the cup opening bearing great gradient magnitudes could be well matched, which can be seen in the difference images (Figures 7.4c and d). Correspondigly, the standard deviation of θ in the images of neutral orientation was found to have the small values of 0.36° in the first and of 0.13° in the second series. Again, the estimation of ϕ was not affected, whereas ψ could be determined more reliably than if using version 2, probably due to the independency from the initial estimate. According to these results, the deviations of $\Delta\alpha$, $\Delta\beta$, and $\Delta\gamma$ from ground truth are much smaller as can be seen by the plots in the Figures 7.5c and 7.6c and by the standard deviations in Tab. 7.8. Omitting the 2D correction and the calibration had only a negligible influence on the orientation estimation in the first series, whereas in the other one it significantly increased the standard deviations, especially the one of $\Delta\gamma$. Reasons for that may be the larger difference between f_x and f_y and the great deviation of the real principle point from the film center indicated by the high values of $t_x = -8.0\,\text{mm}$ and $t_y = 9.5\,\text{mm}$ in series 2.

The drawback of comparing the gradient images may be the loss of information by the necessary gauss filtering with a high sigma. To use all available information and hence further increase the precision, in version 4 the gray value differences were minimized after a correction the scatter. At this time, however, the problem of the dependency from the initial estimate was overcome by calculating the required synthetic image using the parameter estimate of a gradient difference minimization run before. This solution in fact led to a slight further reduction of the deviation from ground truth of $\Delta\alpha$, $\Delta\beta$, and $\Delta\gamma$ (see the Figures 7.5d and 7.6d and Tab. 7.8). The still large errors in the first series, especially the one of $\Delta\beta$, possibly resulted from structures of the calibration box superposing the cup in the image. They are partly visible in Fig. 7.4, such as a vertical stripe and two calibration spheres.

Having overcame the problem of the scatter, the parameter which is still problematic is ϕ, because only the small screw socket gives information about the orientation with respect to the polar axis. In this work, this angle could be determined with an error of maximally 0.8° allowing for a quite precise reconstruction of the rotation of the cup in the x-ray system
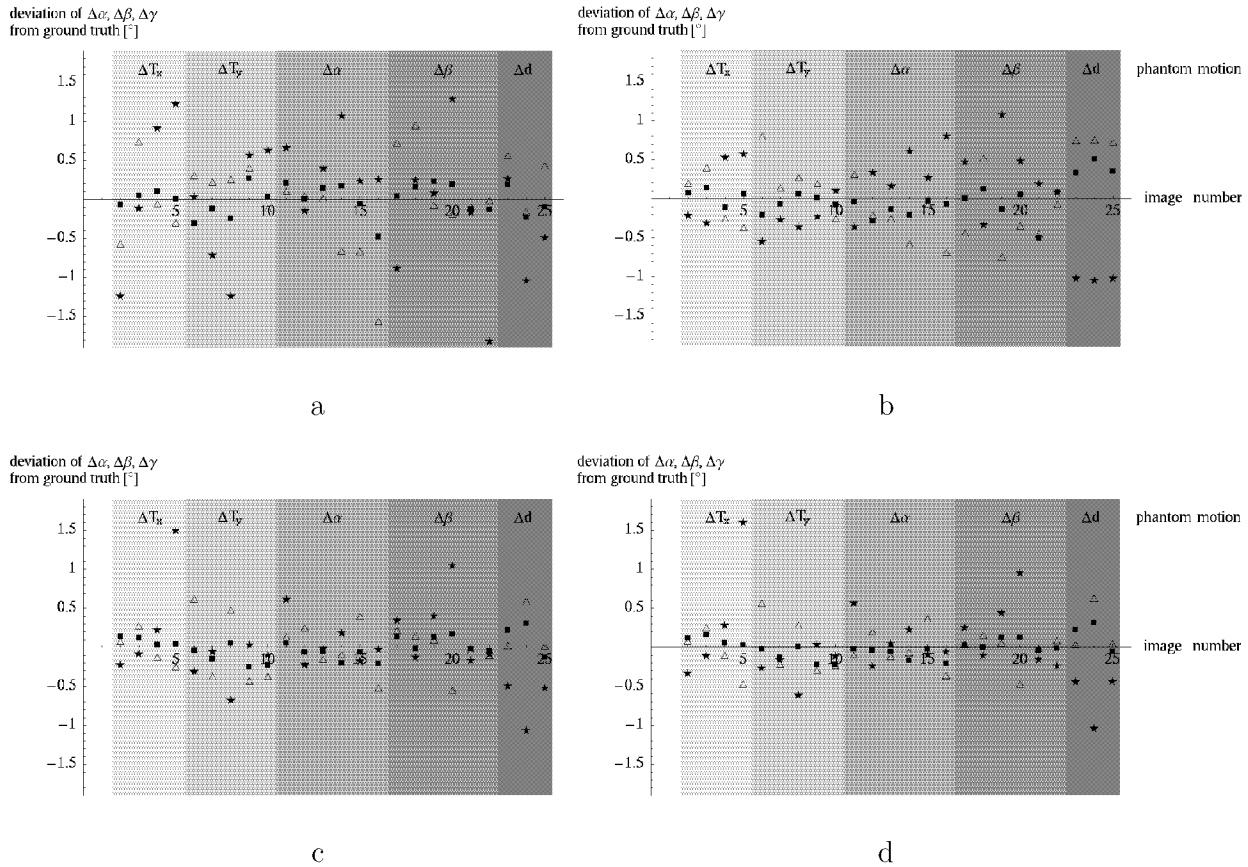
Figure 7.5: *The Figures a–d show the deviation from ground truth of $\Delta\alpha$ (triangles), $\Delta\beta$ (stars), and $\Delta\gamma$ (squares) estimated by applying the Analysis-by-Synthesis versions 1– 4, respectively, in the (calibrated) images of series 1. In favour of a better visibility of the precision improvement, the plots were centered with respect to the horizontal axis by subtracting the mean deviations from ground truth.*

between two exposures. The estimation of ϕ, however, depends on the orientation of the implant in the hip. At some orientations, the position of the socket only slightly alters at a variation of this angle, or only a small part of the socket is visible. In these cases, this parameter can only be estimated roughly. As both $\Delta\alpha$ and $\Delta\beta$ depend on ϕ, a reliable reconstruction of the cup between two exposures is then hardly possible.

7.3.3   The experimental error of the migration measurement

The standard deviation and the accuracy of the migration measured using XIMIT were assessed in the two validation series. The former was estimated using the exposures where the orientation and position of the pelvis was varied but the cup position relative to the bone remained the same. For the assessment of the latter, the measurements in the radiographs where a migration was simulated were compared to the ground truth. In both cases, the
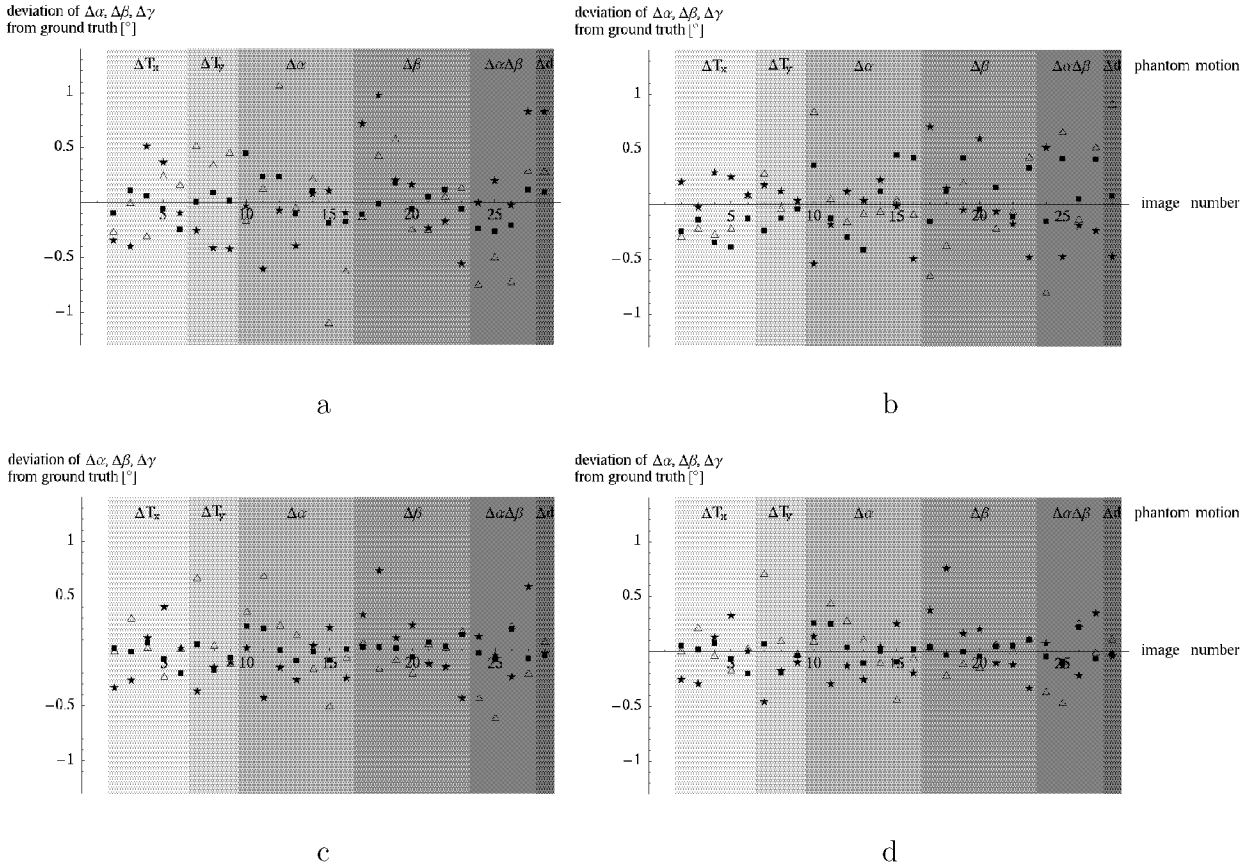
Figure 7.6: *The Figures a–d show the deviation from ground truth of $\Delta\alpha$ (triangles), $\Delta\beta$ (stars), and $\Delta\gamma$ (squares) estimated in series 2 using the Analysis-by-Synthesis versions 1– 4, respectively. Like in the previous figure, the mean deviations were subtracted.*

parameter search	2D correction and calibration	series 1			series 2			
		$\sigma_{\Delta\alpha}$	$\sigma_{\Delta\beta}$	$\sigma_{\Delta\gamma}$	$\sigma_{\Delta\alpha}$	$\sigma_{\Delta\beta}$	$\sigma_{\Delta\gamma}$	$[°]$
version 1	yes	0.54	0.83	0.19	0.47	0.46	0.17	
version 2	yes	0.48	0.58	0.21	0.39	0.32	0.28	
version 3	yes	0.33	0.53	0.15	0.30	0.30	0.11	
	no	0.37	0.56	0.19	0.31	0.41	0.33	
version 4	yes	0.28	0.53	0.14	0.25	0.27	0.12	

Table 7.8: *The standard deviations $\sigma_{\Delta\alpha}$, $\sigma_{\Delta\beta}$, and $\sigma_{\Delta\gamma}$ from ground truth of the angles of cup rotation around the x-, the y-, and the z-axis using the different Analysis-by-Synthesis versions.*

positions of the bony landmarks and of the cup were determined as precisely as possible. According to the Sections 7.3.1 and 7.3.2, this is the case if the teardrop figure is matched using the template shown in Fig. 7.1b and if the implant is located using the Analysis-by-Synthesis version 4.

This subsection is organized as follows: After the explanation of the determination of the standard deviation in the next paragraph, the outcome of measuring (d_{ml}, d_{cc}) in the two radiographic series using only natural bony landmarks is described. Then, the results for d_{ml} and d_{cc} in the second series if using (i) the lateral and (ii) the medial tantalum ball are discussed. The external marker in the middle is neglected, because it is superposed by the superior border of the acetabulum. In the last paragraph, the deviation of the measured migration from ground truth is reported.

The aim of the experiments was a controlled simulation of the clinical conditions at diagnostic anterior-posterior exposures of the pelvis to obtain a realistic estimate of the precision in measuring the bone–cup distance. The pelvis was first translated along the medio-lateral and the cranio-caudal axis and then rotated around these axes. It was moved so that the experimental variance of the respective changed position or orientation could correspond to its real magnitude. Therefore, the variance of (d_{ml}, d_{cc}) in the radiographs where the pelvis was rotated around the medio-lateral axis, for example, should reflect this movement's share in the total error of the measured cup–bone distance. The pelvis motions between two exposures were simulated in the experiments one after the other (with the exception of combined rotations in series 2). In real pelvis exposures, the motions all occur at the same time. Hence, as stated already in Sect. 7.1.2, the images were grouped according to the motions simulated, the variance of (d_{ml}, d_{cc}) was calculated in each group, and then the resulting variances were added up to estimate the overall error. According to the assumption of subsequent motions, the images of combined rotations in series 2 were disregarded . This also allows for a better comparability of the two series.

In the Figures 7.7 and 7.8, the deviations of the d_{ml} and d_{cc} measured in the comparison images of the two series from their values in the reference images are plotted. Fig. 7.8 also shows these deviations when using the medial or the lateral tantalum ball as bony landmark $\mathbf{m}_3$ instead of the teardrop figure. In the second series, the pelvis bone had been fixed in the validation unit with a slightly different orientation than in the first. As this led to a change of the teardrop figure template, the influence of translations and rotations on d_{ml} and d_{cc} differed between the two series, which is visible in the plots. Still, in both series the measured medio-lateral component shows a small variability at translations and a greater one at rotations, especially at the one around the x-axis (see Fig. 7.7a and Fig. 7.8a). This behaviour corresponds to the theoretical sensitivity towards the entering errors, which is predicted by the coefficients in the expressions (7.1) and (7.4), and to the experimental performance in matching the teardrop figure, which is visualized by the plots in Fig. 7.2. Only the jump of d_{ml} between the images 15 and 16 in the first series, where a little rotation caused a significant shift of the patch to a different image position, is unforseen. The overall standard deviation of d_{ml} is hence greater in this series than predicted, 0.41 mm instead of 0.27 mm, while the one in the other series exactly corresponds to the theoretically determined value of 0.28 mm (compare the Tables 7.2 and

7.9). The variance of the cranio-caudal component is much smaller than expected. The rotation around the medio-lateral axis, the most important source of error, should have a similar influence on this component as the one observable if the medial marker is used (see the curve with circles at the images 10–16 in Fig. 7.8b). However, in series 1 it shows no significant effect and in series 2 only a reduced inconsistent one. As reported in Sect 7.3.1, the result of matching the teardrop figure particularly depends on the orientation of the pelvis influencing the appearance of this figure in the image. The shift of the matched teardrop figure area caused by a rotation does not necessarily correspond to the rotational displacement of the projection of a 3D point. Apparently, in the images of rotation around the x-axis this shift compensated for the expected geometrical effect of the rotation on d_{cc}. The resulting precision improvement, which becomes evident in the small standard deviations of $\sigma_{d_{cc}} = 0.10$ mm and $\sigma_{d_{cc}} = 0.18$ mm listed in Tab. 7.9, unfortunately can not be generalized to other pelves on the base of the experiments. Alone in the two radiographic series of the same pelvis, the slight change in the neutral orientation caused an obvious alteration of the measurements.

The use of the lateral tantalum ball as bone reference point implicated a great dependency of the measurement on the pelvis orientation and translation. As described in Chapter 3, the sensitivity of (d_{ml}, d_{cc}) towards pelvis motions grows with increasing distance between cup center $\mathbf{C}_0$ and bone reference point. The fact that in y-direction this marker is further away from the cup center than the teardrop figure may play a role, because the cranio-caudal distance is more relevant for this sensitivity than the medio-lateral one. However, it is probable that also the z-distance between $\mathbf{m}_3$ and $\mathbf{C}_0$ is increased, even though the aim was to implant the tantalum ball at the same height above the film plane as the cup center. Only this can explain the undeniable influence of translations on d_{ml} and on d_{cc} observed in the images 2–6 and the images 7–9, respectively (see Fig. 7.8). It explains also the great effect of rotations on d_{ml} and d_{cc}. The overall standard deviations resulted to have the correspondingly high values of $\sigma_{d_{ml}} = 0.75$ mm and of $\sigma_{d_{cc}} = 1.64$ mm.

If the marker implanted in the area of the teardrop figure was used as $\mathbf{m}_3$, the bone–cup distance measured corresponded basically to the expectations. Still, it is difficult to identify the effects of the pelvis translations in the Figures 7.8a and b because of the zigzag run of the curves. The comparison of the plots with the deviation from ground truth of ΔT_z shown in Fig. 7.3b indicated that these oscillations are due to an incorrectly estimated z-position of the cup. This parameter affects the measured bone–cup distance because the correction for magnification in the expression (3.1) for $\mathbf{d}$ corresponds to a multiplication by T_z. The influence of the rotation around the x-axis can be well observed in the plot of d_{cc}, but also in the one of d_{ml}. The strong deviation of the medio-lateral component at the pelvis rotation around the y-axis does not correspond to the theoretically predicted sensitivity towards this source of error (see the coefficients in the expressions (7.1) and (7.4). It maybe arose from the matching because at some orientations also the localization of the marker was affected by the superposition of bony structures. On the other side, d_{cc} seems to be completely independent from the orientation with respect to the y-axis, which also contradicts the theoretical results. It may again be a sign of an error in the matching that here compensated the expected rotational displacement. The standard deviations of
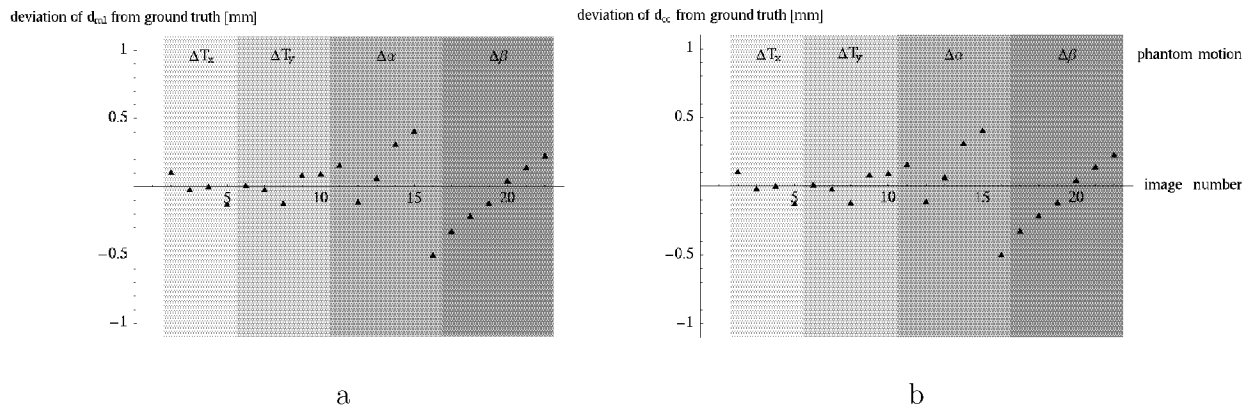
Figure 7.7: *The deviation in series 1 of the measured components d_{ml} and d_{cc} from ground truth given by their magnitudes in the reference image.*
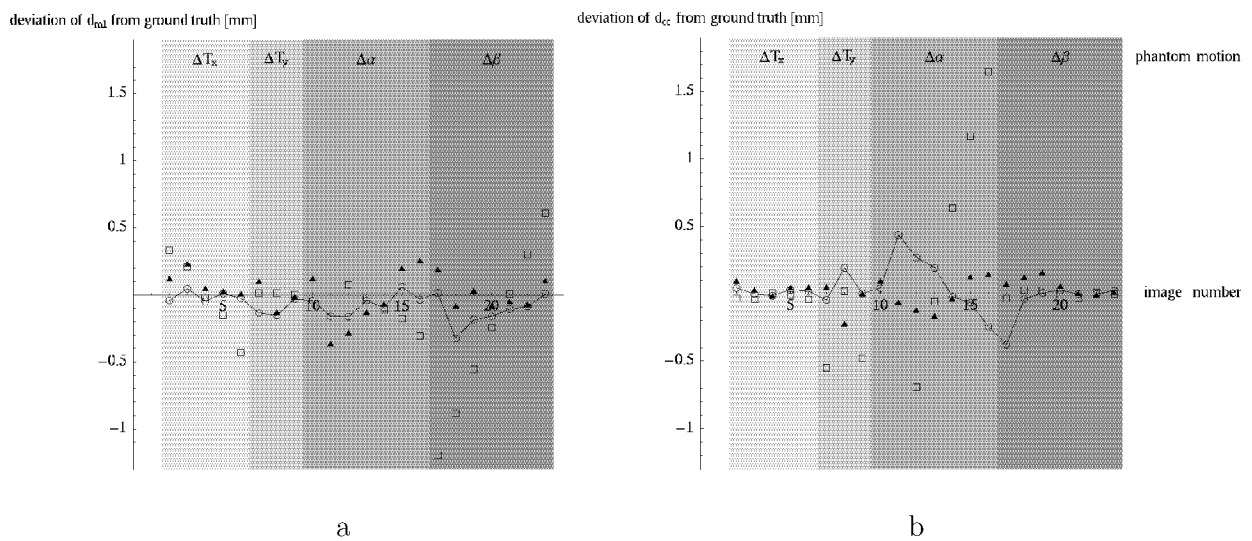

Figure 7.8: *The deviation of d_{ml} and d_{cc} from ground truth in series 2 using the teardrop figure (triangles), the lateral tantalum ball (squares), and the medial marker (circles, connected for better visibility) as bone reference. In the second case, two values are missing because in the images 10 and 11 the lateral marker was covered by the cup.*

	$\mathbf{m}_3$	$\sigma_{d_{\mathrm{ml}}}$	$\sigma_{d_{\mathrm{cc}}}$	[mm]
series 1	teardrop figure	0.41	0.10	
	teardrop figure	0.28	0.18	
series 2	lateral marker	0.75	1.64	
	medial marker	0.17	0.31	

Table 7.9: *The precision in determining the 2D distance $(d_{\mathrm{ml}}, d_{\mathrm{cc}})$ found by the validation experiments.*

d_{ml} and d_{cc} were found to be 0.17 mm and 0.31 mm, respectively. They slighlty lie below the theoretically calculated values listed in Tab 7.2. Reasons for this can be the just mentioned compensation of the geometrical deviations and an overestimation of the error in locating the cup and the marker or the one in determining the magnification factor.

The migration $\Delta\mathbf{d}$ measured in the images where the cup was displaced is shown in Tab. 7.10. For comparability, in this table also the ground truth of Sect. 6.2.3 is presented. Regarding the single components Δd_{ml} and Δd_{cc} an obvious deviation of the measurement from the ground truth has to be admitted. The reason for this is that the image coordinate system, which is defined through two symmetrical points of the foramina obturatoria marked by the user, had a different orientation than the x-ray coordinate system where the ground truth is represented in. It altered also between the two series, probably because of the mentioned orientation change of the pelvis between the experiments. This alteration can be seen in the results of Δd_{ml} and Δd_{cc} if using the teardrop figure as landmark $\mathbf{m}_3$. However, the deviations of the individual components are not significant for the accuracy, because the image coordinate system is meant to stay the same within one series of radiographs. A more meaningful quantity is the total migration $|\Delta\mathbf{d}| = \sqrt{\Delta d_{\mathrm{ml}}^2 + \Delta d_{\mathrm{cc}}^2}$ independent from the orientation with respect to the ventral-dorsal axis. The total migration could be determined very exactly (see Tab. 7.10). The small remaining error of 0.02 mm–0.04 mm in the first series may be due to an incorrectly estimated magnification factor or due to a false ground truth.

These results indicate that the cup displacement relative to the bone can be measured without systematical error. However, they are not meaningful for real measurements because the pelvis was kept in the same position and orientation. Having found that a systematical error can be excluded, the error of practical relevance is supposed to be given by the standard deviations reported in Tab. 7.9. To check if XIMIT really allows for that precision, the migration between the images 1 and 28 of the second series was measured. Between the acquisition of these radiographs the cup had been displaced and the phantom had been rotated around the medio-lateral and the cranio-caudal axis, which also had led to a pelvis translation in x-, in y-, and in z-direction (see Tab. 6.2). The ground truth of the migration was newly calculated according to the description in Sect. 6.2.3 on the basis of the orientation in image 1. Using the teardrop figure point as bone reference, an unexpectedly small deviation of the measured migration from ground truth was found (see

series	pelvis motion	$\mathbf{m}_3$	ground truth			measurement		
			Δd_{ml}	Δd_{cc} [mm]	$|\Delta\mathbf{d}|$	Δd_{ml}	Δd_{cc} [mm]	$|\Delta\mathbf{d}|$
1	no	teardrop figure	0.64 1.29 1.93	−0.70 −1.40 −2.11	0.95±0.03 1.91±0.06 2.86±0.09	0.55 1.11 1.84	−0.82 −1.58 −2.21	0.99 1.93 2.88
2	no	teardrop figure lateral marker medial marker	0.64	−0.69	0.94±0.03	0.78 0.64 0.77	−0.54 −0.65 −0.57	0.95 0.92 0.95
2	yes	teardrop figure lateral marker medial marker	0.65	−0.70	0.95±0.03	0.65 0.42 0.73	−0.75 −0.05 −0.38	0.99 0.42 0.82

Table 7.10: *The comparison of the measured migration* $(\Delta d_{\mathrm{ml}}, \Delta d_{\mathrm{cc}})$ *with the ground truth.*

Tab. 7.10). This probably has its origin in the unpredictable displacement of this point at rotations. Using the external markers, the influence of the pelvis motion can be observed in the increased deviations from ground truth. Still, for both the tantalum balls, this deviation can be assumed to lie within the respective error bounds shown in Tab. 7.9.

7.4   Evaluating real radiographic follow-up series of THR

Radiographs of clinical follow-up studies were evaluated in order to test XIMIT in real data. As the ground truth of the cup rotation and translation between two exposures and of the migration is missing, only qualitative results could be gained. Eight series containing altogether 49 images were available. However, the investigated FITEK cup had been implanted only in three pelves and in four hips (one of the patients had a THR on both sides). The localization of the bony landmarks was tested in all series, which is reported in Sect. 7.4.1. Four categories were defined to judge the matching results. Analysis-by-Synthesis and the migration assessment could only be applied in the pelves with the FITEK cup. The difference images are shown in Sect. 7.4.2 to give an impression of the performance of the method. In Sect. 7.4.3 the measured migration is reported.

7.4.1   Performance in matching the bony structures

The localization of the bony landmarks was judged according to the following scheme:

- The pelvis orientation in the reference image with respect to the other images affects the matching. It defines the comparability of the template with the corresponding

area in the comparison images. In order to achieve similar conditions in all series, the choice of the reference image was standardized. If possible, the earliest radiograph of the series was used as reference image disregarding the pelvis orientation. Only, if one of the bony landmarks could not be identified at all the subsequent x-ray image was taken. This was the case for two series, where the first radiographs were acquired intra-operatively, and for one series, where the contrast was deteriorated in some images by an operating error at the digitization.

- The templates were defined similarly to the ones in the Figures 4.2 and 4.5b. Care was taken to leave the ilio-ischial line out from both the teardrop figure template and the patch.

- In some comparison images, individual bony structures were not visible at all or they had such an abnormal appearance that no initial estimate of the landmark position could be given. These structures were classified as "not localizable". The cases, where the result of the matching was obviously wrong were classified as "mismatch". The cases, where it was difficult to judge the matching result were classified as "ambiguous". In the remaining cases, the landmark found in the comparison image seemed to correspond to the one in the reference image and the matching result was classified as "reliable".

- If the localization failed in the first trial, the choice of the ROI and the initial estimate was repeated once before the classification. In case of teardrop figures largely extended in cranial direction, the height of the template was reduced in the second trial.

The landmarks m_1 and m_2 could in general be reliably localized. Only in one image of the series where the contrast was reduced by the digitization, the foramina obturatoria were not localizable (see the Figures 7.9a and b). In four out of altogether 98 foramina obturatoria the results were classified as ambiguous, because the correspondence of the landmark found in the comparison with the one in the reference image was questionable. The reason for this was probably the superposition of the caudal edge by varying soft tissue structures (see the Figures 7.9c and d).

In five hips, m_3 was not localizable due to great out-of-plane rotations. Two examples are shown in Fig. 7.10. In the image shown on the right (Fig. 7.10 d), additionally the contrast is reduced because the exposure was made intra-operatively. A mismatch had to be reported only in the case of the two teardrop figures shown in Fig. 7.11. It occurred in the series, where the contrast was changed by the digitization. The matching is in general quite stable, because only the translation is estimated and the parameter search hence has only two degrees of freedom.   The main problem in localizing the teardrop figure was that often the performance of the matching could not be judged. The correspondence of a point of this structure between comparison and reference radiograph was not intuitively clear if a significant pelvis rotation and translation had occurred (see Fig. 7.12a and b). Furthermore, in some of the hips the identification of a certain point in both images was
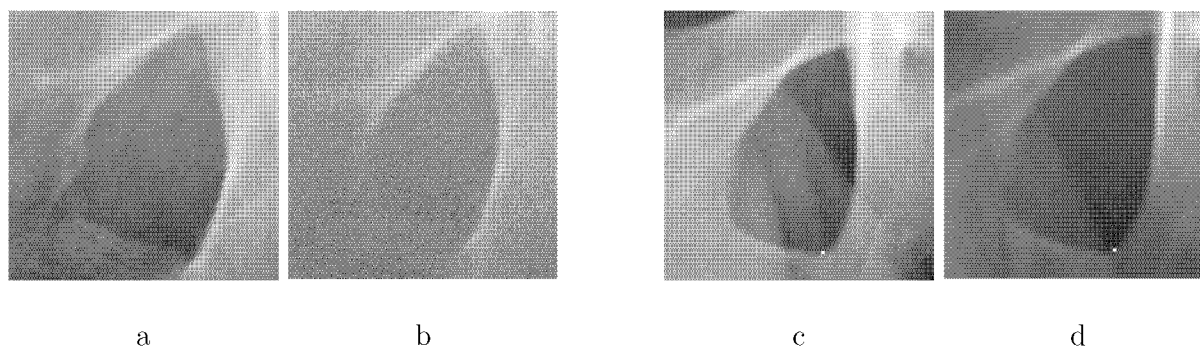
Figure 7.9: *The right foramen obturatorum in the reference and in the comparison image in the case where the landmark could not be localized (a and b) and in a case where the matching result was classified as ambiguous (c and d). The small points indicate the user defined landmark in the reference image (c) and the one estimated by the matching algorithm (d).*
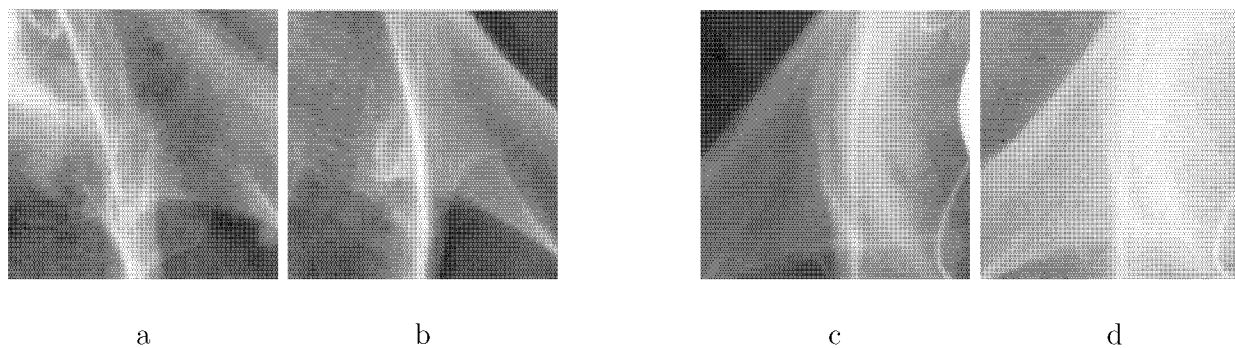

Figure 7.10: *Two teardrop figures in the reference (a and c) and in the comparison images (b and d) in cases where the landmark could not be localized at all due to great out-of-plane rotations.*
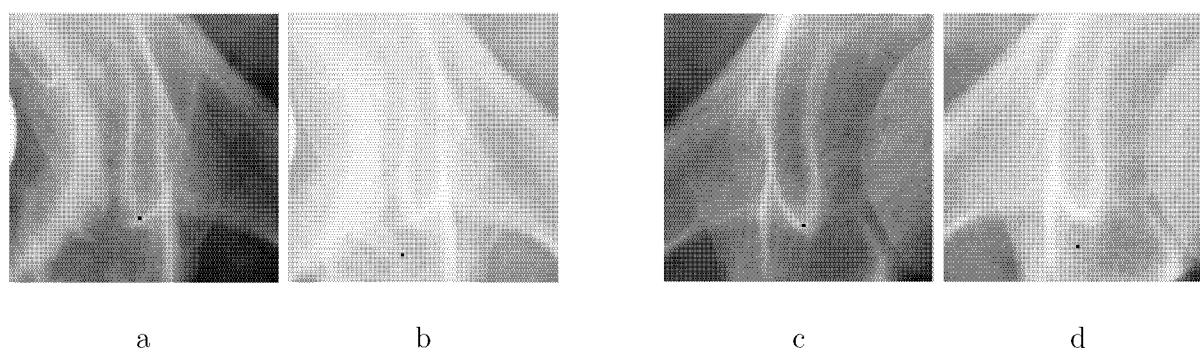

Figure 7.11: *The left (a and b) and the right (c and d) teardrop figure in the reference image and in the comparison image in the case of a mismatch. The small points indicate the user defined landmarks in the reference image (a and c) and the landmarks found by the matching algorithm (b and d).*
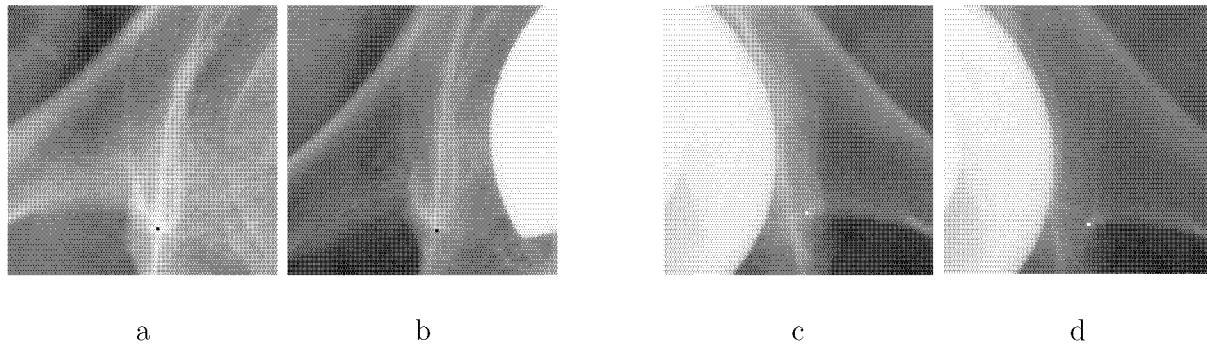
a   b   c   d

Figure 7.12: *Two teardrop figures where the matching result was classified as ambiguous. The small points indicate the user defined landmarks in the reference image (a and c) and the landmarks found by the matching algorithm (b and d).*

difficult, because the teardrop figure was hardly visible (see Fig. 7.12c and d). For these reasons, in 18 cases the matching result had to be classified as ambiguous. In the remaining 74% of the teardrop figures, m_3 could be located reliably.

7.4.2   Performance of Analysis-by-Synthesis

Two of the follow-up series with a FITEK cup included four radiographs, and one only three. The images were evaluated analogously to the ones of the validation experiments, applying three different versions of Analysis-by-Synthesis. The film–focus distance and the x-y-position of the film were assumed to have their nominal values of $f=1200\,\mathrm{mm}$ and $t_x = t_y = 0\,\mathrm{mm}$. First, the minimization of the gray value difference between the unmodified original and the synthetic image of the cup was tested. Second, the difference in the spatial gradients of the two images was minimized. Using the resulting parameters, the low frequency range of the original image was adapted to the one synthesized. A third parameter search was run comparing the gray values of the synthetic image to the ones of the original image corrected for the scatter. These three ways of estimating the 3D position and orientation of the cup correspond to the versions 1, 3, and 4 in Sect. 7.3.2. The scatter correction based on the initial parameters (version 2) was omitted because of the observed influence of the initially estimated orientation. In the following paragraphs, the difference images between the original x-ray projection in the reference radiograph of each series and the estimated synthetic one are discussed. The cup angles found by applying the best version in all images were used to roughly assess the variability of the pelvis orientation at exposure. The results of this assessment are presented at the end of this subsection.

If the gray values were evaluated without considering the scatter, the final synthetic images of the cup did not match perfectly to the original ones (see Figures 7.13a–d). Like in the evaluation of the validation radiographs, especially the orientation of the cup with respect to its axis e_θ could not be determined correctly. Only in the first series, the cup opening was only slightly darkened by the scatter and a better matching between synthetic and original image resulted (Fig. 7.13a and b).

$\mu_{\Delta\alpha}$	$\sigma_{\Delta\alpha}$	$\mu_{|\Delta\alpha|}$	$\mu_{\Delta\beta}$	$\sigma_{\Delta\beta}$	$\mu_{|\Delta\beta|}$	$\mu_{\Delta\gamma}$	$\sigma_{\Delta\gamma}$	$\mu_{|\Delta\gamma|}$	$[°]$
-1.5	2.8	2.6	-1.0	3.2	2.1	-2.5	2.2	2.7	

Table 7.11: *The mean $\mu_{\Delta\alpha,\Delta\beta,\Delta\gamma}$, the standard deviation $\sigma_{\Delta\alpha,\Delta\beta,\Delta\gamma}$, and the absolute mean $\mu_{|\Delta\alpha|,|\Delta\beta|,|\Delta\gamma|}$ of the angles of cup rotation in the x-ray system between the reference and the comparison radiographs.*

As the Figures 7.13e–h show, the minimization of the gradient image difference improved the estimation of the angle θ. However, a deterioration of the found orientation of the cup with respect to its polar axis $\mathbf{e}_\phi$ could be observed in the second and in the third series (see Figures 7.13g and h). The reason for this was possibly the reduction of the image resolution by the Gaussian filtering, which is necessary if comparing spatial gradients. The estimation of ϕ is generally problematic as the upper screw socket of the cup is the only structure which gives information about this angle. It was especially difficult in the second series (see the third column in Fig. 7.13), because there only a small part of this socket is visible.

Using version 4, the effect of the scatter is eliminated as well as the resolution is retained. Thus, it provided the best results in case of all evaluated radiographs. The good performance is demonstrated by the difference images shown in the Figures 7.13i–l.

Based on the estimated angles in all images, the rotation of the cup in the x-ray system at the later exposures from its orientation at the earliest exposure was reconstructed. The mean, the standard deviation, and the absolute mean of the angles $\Delta\alpha$, $\Delta\beta$, and $\Delta\gamma$ of the cup rotation around the x-, the y-, and the z-axis of the x-ray coordinate system were calculated. Neglecting the rotation of the implant within the bone and the uncertainty in determining the cup's polar angle, these quantities give an insight about the variability of the pelvic orientation at exposure. The resulting values shown in Tab. 7.11 indicate that the orientation is relatively stable. The standard deviation of $\Delta\alpha$ is significantly smaller then the one of the pelvis rotation around the medio-lateral axis assumed in the scope of the theoretical error analysis (see Sect. 2.6.2). The great value of $\sigma_{\Delta\beta}$ origins from the earliest radiograph of the second series, which was acquired intra-operatively. Omitting this radiograph and taking the next one as reference image would yield the much smaller of $1.8°$. The standard deviation of $\Delta\gamma$ approximately corresponds to the intuitively estimated amount of pelvic in-plane rotation in Sect. 2.6.2. The deviations of the mean values $\mu_{\Delta\alpha}$, $\mu_{\Delta\beta}$, $\mu_{\Delta\gamma}$ from zero may be partly due to a non-standard pelvis orientation in the first radiographs because of pain.

7.4.3 Measured migration

For the determination of the migration, the cup position was estimated using the most reliable Analysis-by-Synthesis version. The bony landmarks were located as described in Sect. 7.4.1. The medio-lateral and the cranio-caudal migration determined in the three evaluated series are plotted below subject to the exposure dates.
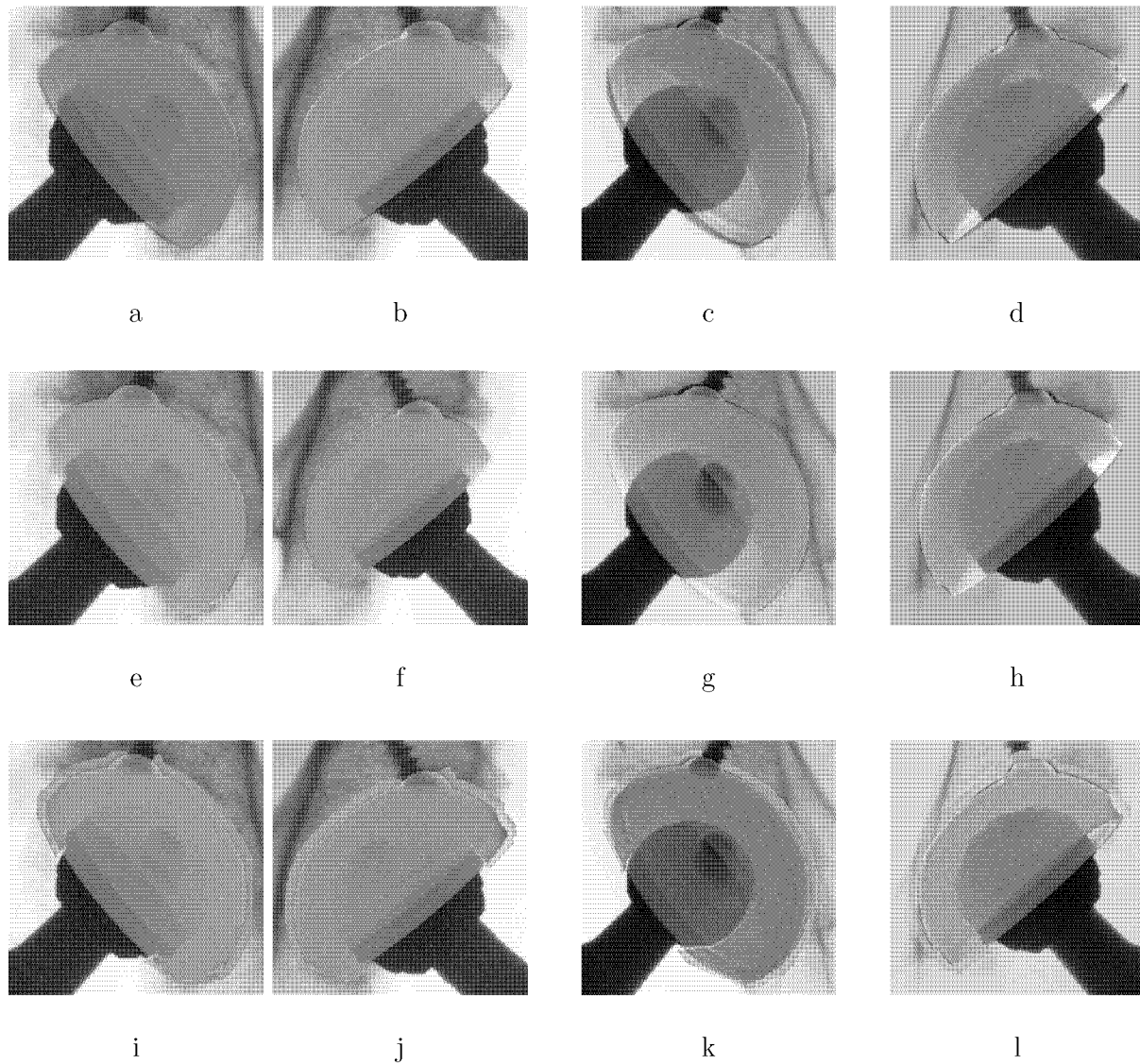
Figure 7.13: *The difference images between the original x-ray projection and the synthetic one generated using the final parameter estimate. The Figures in the two left columns show the cups in the reference image of the series 1, where both hip joints were replaced. In the columns on the right the implants in the other two series can be seen. In the first row (Figures a–d), the difference images which resulted by directly comparing the gray values are shown. The images in the second row (Figures e–h) were obtained by comparing the gradients, and the ones in the third row (Figures i–l) by applying the Analysis-by-Synthesis version 4.*
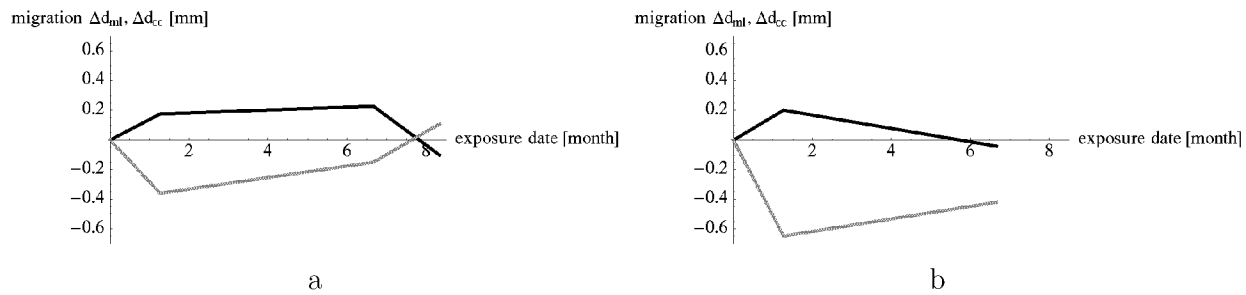
Figure 7.14: *The migration measured in the series with the THR on both sides. Fig. a shows the migration of the left and Fig. b of the right cup. The latter could not be located in the last radiograph, because a dislocation had occurred. The black line indicates the medio-lateral, and the gray line the cranio-caudal component of the migration.*
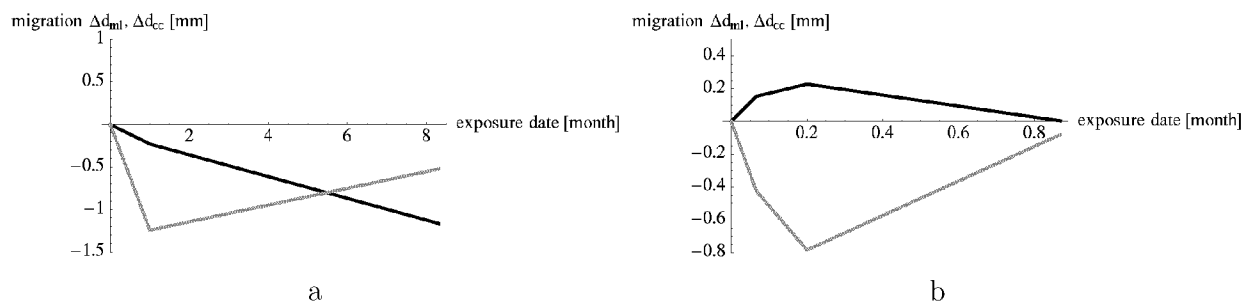

Figure 7.15: *The migration measured in the other two series. Again, the black line indicates the medio-lateral, and the gray line the cranio-caudal cup displacement. Fig. a shows the measurements in a series, where the ipsilateral teardrop figure was hardly visible. This bony structure could also not be reliably localized in the third radiograph of the series of Fig. b.*

In the series with the two implants, both teardrop figures could be reliably located. The migration $(\Delta d_{\mathrm{ml}}, \Delta d_{\mathrm{cc}})$ measured for the left cup is plotted in Fig. 7.14a. It lies within the error bounds, which were estimated in Sect. 7.1 to be 0.36 mm and 0.46 mm for Δd_{ml} and Δd_{cc}, respectively. Hence, it can be assumed that the cup had remained at the same position in the bone. The results for the right cup are shown in Fig. 7.14b. In the second radiograph, a migration was measured which exceeds the standard deviations. A significant pelvis rotation could neither be observed with the naked eye nor by means of the estimated cup orientation. Thus, a cranial displacement of the right artificial hip socket is probable. This was confirmed by the measurement in the subsequent radiograph. In the last image of this series, the cup on the right could not be located because of a dislocation of the femoral head.

The results of the second series plotted in Fig. 7.15a are not very meaningful. It is the series with the indistinct teardrop figure shown in the Figures 7.12c and d. In none of the radiographs, $\mathbf{m}_3$ could be localized reliably. Additionally, the earliest image shows the

pelvis in a non-standard orientation due to the intra-operative acquisition of the radiograph. This is also indicated by the estimated great rotation of the cup between the first and the second image of 3.0°, −5.0°, and 3.3° around the x-, the y-, and the z-axis, respectively. The determined change of the bone–cup distance between the second and the third radiograph may be due to a real migration or due to a shift of the teardrop figure point, which is visible in the Figures 7.12c and d.

The great cranial migration in the third series (Fig. 7.15b) was also observed in a radiograph, where the matching of the teardrop figure was classified as ambiguous. In this case, the problem was rather a great translation than the variable orientation of the pelvis. In the third image, a shift of the cup of 57 mm in cranial direction was estimated by Analysis-by-Synthesis. In the other images of this series, the bony landmarks were judged to be located reliably. There, the found migration lies within the error bounds. A real displacement of the cup is hence not indicated.

8

Conclusions

The subject of this thesis was the measurement of the distance between a hip implant and the bony counterpart using the relatively cheap and widespread technique of planar x-ray radiography. The focus was set on assessing the cup displacement of artificial hip sockets within the bone using standard anterior-posterior pelvis radiographs. The main concern was the achievement of high precision. The problem was analysed geometrically by working out a scheme for the theoretical error estimation of the previous approaches for cup migration measurement. Based on this analysis, a system was designed that was termed XIMIT: x-ray evaluation using Implant Models and Image Templates. The system makes the precise measurement of the cup migration in medio-lateral and in cranio-caudal direction possible. It includes a template matching algorithm allowing for subpixel precision in order to exactly determine the image position of the necessary bony landmarks. For locating the implant, a generic method for recovering the 3D orientation and position of a well-defined object in a single x-ray image was developed. The system was validated using radiographs of a real bone pelvis phantom. During the acquisition of these radiographs the main entering errors at clinical x-ray exposures were simulated.

The scheme for the theoretical error analysis provided a reliable basis for the development of XIMIT. The theoretically predicted standard deviation only differed of 40μm from its experimental value using a small tantalum ball as bone reference for the cup position. The scheme gives information about the error which has to be expected as well as about the optimal position of the bone reference points. It can be used for designing methods for migration assessment using x-ray images acquired from directions different from the anterior-posterior one or using radiographs of knee or shoulder implants. It is especially useful in cases where markers need to be implanted because of lacking image structures, such as in lateral pelvis radiographs. Through the cross-validation between theoretical and experimental results, it was discovered that the theoretical error estimation shows remarkable limits in those cases where only natural bony landmarks are used. This is due to the unpredictable appearance of bony structures in the image subject to the pelvis orientation and position in the x-ray system. In the experiments, a standard deviation of the cranio-caudal migration lying up to 0.27 mm below the theoretically determined value was found using the teardrop figure as bone reference.

The unpredicable appearance of bony structures was found to affect the performance of the template matching algorithm. Applying template matching, the landmarks are located by

estimating the mapping of the radiographic structures between two images. The algorithm provided the possibility of modelling the mapping by various 2D transformations with up to six parameters. However, it only worked robustly if the estimated transformation was restricted to a translation. Modelling the alteration of the structures due to a rotation of the pelvis between two exposures was not possible. Still, in most cases the positions of the bony landmarks could be precisely determined considering only the translation. In particular good results were obtained for the localization of the landmarks defining the image system. These were chosen to be the most caudal-lateral points of the foramina obturatoria. The standard deviation in determining their image coordinates resulted to be 60μm keeping the pelvis phantom in the same position and orientation. As the contours of the foramina obturatoria provide robust image structures and do not vary significantly from pelvis to pelvis, a general error of this order of magnitude is realistic. Also the standard deviation of 50μm found for the coordinates of the external markers does reflect the precision in the general case. The markers could be located exactly despite their small diameter of 0.8 mm because of the high effectivity of the matching algorithm in evaluating the image information. The localization of the teadrop figure, however, is problematic. This figure is the only natural bone reference close enough to the cup for guaranteeing a geometrical precision of XIMIT in the sub-millimeter range. Unfortunately, its appearance in the image is quite sensitive towards out-of-plane rotations and differs from pelvis to pelvis. In the validation experiments, the error in determining the image position of this bony structure at a varying pelvis orientation and position was investigated. A standard deviation of 0.29 mm and of 0.32 mm for the x- and the y-coordinate, respectively, was found. These values are valid in the pelvis used for the validation. However, within the clinical series evaluated, there were pelves where the teardrop figures were more distinct, but also single hips where they were hardly visible. This showed a variability of this figure in clinical conditions, which can not be reproduced by a phantom experimental set up. An additional problem is the definition of the template. The template for matching the foramina obturatoria and the external marker can easily be standardized by restricting the choice of the region of interest marked by the user. In the case of the teardrop figure, due to its its varying shape, a standardization is difficult.

For the implant these problems are irrelevant because its 3D shape is known. Using the principle of Analysis-by-Synthesis, the cup's transformation due to a pelvis orientation and position could be well modeled and a precise localization was achieved. The standard deviation of the 2D coordinates was found to lie between 10μm and 30μm. The developed method additionally allows a precise reconstruction of the cup rotation between two exposures. A standard deviation of the rotational angles from ground truth of at maximum $0.6°$ could be achieved in the validation experiments. The Analysis-by-Synthesis approach is based on the minimization of the difference between the original x-ray projection of the cup and a synthesized one. The synthetic image is generated only considering the primary radiation. The scatter is taken into account by adapting the low frequency range of the original image. Different ways of comparing the original and the synthetic image were tested in the validation radiographs and in real clinical x-ray images. The difference between the images can be minimized either by evaluating their gray values under inclusion

or exclusion of the correction for the scatter, or by evaluating their spatial gradients in each pixel. Which version of Analysis-by-Synthesis should be applied depends on the cup parameters which are of interest, and on the exposure conditions of the individual radiograph. A reliable reconstruction of the rotation required the minimization of the gradient differences. Concerning the position of the cup, the version which was applied resulted to play no role. With the aid of the different minimization options, the developed method can be easily adapted for the use in other implants, such as the femoral head, or knee and shoulder prostheses. In general, it can be extended to any kind of well-defined object in radiographs. Its only drawback is the computing time required for the synthesis of the x-ray image. A full parameter search by the comparison of gray values took about three minutes using a SUN workstation with a 440 MHz processor. Comparison of the gradient images increased the computing time to about 10 minutes. As the main concern of this work was high precision, the optimization of the time performance of the implemented programs was partly overlooked up to the present. With the current implementation, the minimization can be slightly accelerated. However, the optimization is limited because of the high number of pixels and of cup surface triangles. A significant acceleration probably requires the reduction of the resolution of the image or of the surface representation. The speed up of computing resources must be also taken into consideration, when the implementation will be practically used.

The overall error of the migration measurement using XIMIT was determined theoretically and experimentally. The general standard deviation was estimated theoretically assuming the same variability of the orientation and position of the pelvis as in the analysis of the previous methods. It resulted to lie below 0.5 mm for both the measured migration components under the assumption that only natural bony landmarks are used. A second theoretical standard deviation was calculated in order to obtain an exact prediction of the error in the validation experiments. This made the cross-validation of the theoretical and the experimental error estimation possible. The resulting values were slightly greater than the general standard deviation, which confirms that the clinically entering errors were not underestimated in the experiments. The experimental precision was estimated by determining the variance of the measured bone–cup distance at a varying position and orientation of the validation phantom. Using the teardrop figure as bone reference, a standard deviation for the medio-lateral and the cranio-caudal distance of at maximum 0.41 mm and 0.18 mm, respectively, was found. Using the implanted tantalum ball as reference, these values resulted to be 0.17 mm and 0.31 mm. As mentioned above, the latter numbers well correspond to their theoretical prediction. The accuracy was estimated by simulating a migration in the experiments keeping the pelvis at the same orientation and position. The measured amount of cup displacement only differed of at maximum 40μm from the ground truth. This means that a systematical error in the migration measurement using XIMIT can be excluded.

The developed system provided promising results and is ready for clinical testing. This further stage requires a more user friendly interface to allow for a routine evaluation. User dependency could be a critical point. Some operations, such as the choice of the regions of interest, should be standardized at the operative level. In order to achieve an optimal

performance the system should not be used in a black-box fashion. Assuming no artificial bony marker is implanted, the user should be trained to pay particular attention in the localization of the bone reference. A training data set is given by the radiographs of the experimental validation of XIMIT. Still, the final conclusion of this work is that a measurement of the cup displacement with sub-millimeter precision using standard radiographs is possible. The conditions of this precision are a distinct bony structure used as reference and a positioning of the patient on the x-ray table so that an extreme orientation of her or his pelvis is avoided.

A

Rotation matrix from the angles θ, ϕ, ψ

If a rotation is defined by an angle and a rotation axis, it can be represented as a quaternion, which is a particular four dimensional number. In the following, the relation of the three subsequent cup rotations, which are described by a such a number, to a rotation matrix is described. The properties of quaternions which are relevant in this context are introduced. For a more detailed description of quaternions it is referred to [Watt and Watt 1992].

A quaternion $\mathbf{q}$ is a complex number with three imaginary units $\mathbf{i}$, $\mathbf{j}$, $\mathbf{k}$, instead of one as in the usual complex numbers:

$$\mathbf{q} = s + u_i \mathbf{i} + u_j \mathbf{j} + u_k \mathbf{k}$$

The $u_{i,j,k}$ indicate the magnitude of the imaginary units, which have the properties

$$\mathbf{i}^2 = \mathbf{j}^2 = \mathbf{k}^2 = 1, \quad \mathbf{ij} = \mathbf{k}, \quad \mathbf{ji} = -\mathbf{k}. \tag{A.1}$$

The latter two rules are valid with the cyclic permutation $\mathbf{i} \longrightarrow \mathbf{j} \longrightarrow \mathbf{k} \longrightarrow \mathbf{i}$. The condensed notation for a quaternions is $\mathbf{q} = (s, \mathbf{u})$, where s is a scalar and $\mathbf{u}$ stands for $u_i \mathbf{i} + u_j \mathbf{j} + u_k \mathbf{k}$. Considering the rules (A.1), the multiplication of two quaternions $\mathbf{q}_1 = (s_1, \mathbf{u}_1)$ and $\mathbf{q}_2 = (s_2, \mathbf{u}_2)$ yields

$$\begin{aligned} \mathbf{q}_{12} &= (s_1 + u_{1_i}\mathbf{i} + u_{1_j}\mathbf{j} + u_{1_k}\mathbf{k})(s_2 + u_{2_i}\mathbf{i} + u_{2_j}\mathbf{j} + u_{2_k}\mathbf{k}) \\ &= s_1 s_2 + s_1 \mathbf{u}_2 + s_2 \mathbf{u}_1 - u_{1_i} u_{2_i} - u_{1_j} u_{2_j} - u_{1_k} u_{2_k} + \\ & \quad \mathbf{i}(u_{1_j} u_{2_k} - u_{2_j} u_{1_k}) + \mathbf{j}(u_{1_k} u_{2_i} - u_{2_i} u_{1_k}) + \mathbf{k}(u_{1_i} u_{2_j} - u_{2_i} u_{1_j}) \end{aligned}$$

Interpreting the $\mathbf{u}_{1,2}$ as coordinate vectors and using the condensed notation, the above product can be written as

$$\mathbf{q}_{12} = (s_1 s_2 - \mathbf{u}_1 \cdot \mathbf{u}_2, s_1 \mathbf{u}_2 + s_2 \mathbf{u}_1 + \mathbf{u}_1 \times \mathbf{u}_2).$$

A rotation around an axis $\mathbf{e}_\omega$ with an angle ω transforms a vector $\mathbf{r}$ into $\mathbf{r}'$ according to

$$\mathbf{r}' = \cos(\omega)\mathbf{r} + (1 - \cos(\omega))\mathbf{e}_\omega(\mathbf{e}_\omega \cdot \mathbf{r}) + \sin(\omega)\mathbf{e}_\omega \times \mathbf{r}.$$

This rotation can be described within the quaternion formalism. The vector $\mathbf{r}$ is formulated as the quaternion $\mathbf{q_r} = (0, \mathbf{r})$. The rotation of $\mathbf{q_r}$ is expressed by the product

$$\mathbf{q_{r'}} = \mathbf{q}_\omega \mathbf{q_r} \mathbf{q}_\omega^{-1} .$$

The quaternion $\mathbf{q}_\omega = \left(cos(\frac{\omega}{2}), sin(\frac{\omega}{2})\mathbf{e}_\omega\right)$ and its conjugate $\bar{\mathbf{q}}_\omega = \mathbf{q}_\omega^{-1} = \left(cos(\frac{\omega}{2}), -sin(\frac{\omega}{2})\mathbf{e}_\omega\right)$ contain the rotation parameters.

Subsequent rotations are described by multiplying quaternions. The orientation of the cup, which is defined by three rotations with the angles ψ, θ, and ϕ around $\mathbf{e}_\psi$, $\mathbf{e}_\theta$, and $\mathbf{e}_\phi$, is described by the quaternion

$$\mathbf{q}_{\phi\theta\psi} = \mathbf{q}_\phi \, \mathbf{q}_\theta \, \mathbf{q}_\psi .$$

Thus, a vertex $\mathbf{V}_0$ of a triangle belonging to the cup surface is transformed into $\mathbf{V}$ according to

$$\mathbf{qv} = \mathbf{q}_{\phi\theta\psi} \, \mathbf{qv}_0 \, \mathbf{q}_{\phi\theta\psi}^{-1} .$$

In this work, both the representation of a rotation by a quaternion and the one by a rotation matrix $\mathbf{R}$ are used. The latter is required if the Euler angles, the angles of rotation around the axes of the x-ray coordinate system, are of interest. Given a quaternion $\mathbf{q} = (s, \mathbf{u}) = (s, u_x, u_y, u_z)$, it can be switched to the matrix representation using the formula

$$\mathbf{R} = \begin{pmatrix} 1 - 2u_y^2 - 2u_z^2 & 2u_x u_y - 2su_z & 2u_x u_z + 2su_y \\ 2u_x u_y - 2su_z & 1 - 2u_x^2 - 2u_z^2 & 2u_y u_z - 2su_x \\ 2u_x u_z - 2su_y & 2u_y u_z + 2su_x & 1 - 2u_x^2 - 2u_y^2 \end{pmatrix} . \tag{A.2}$$

B

Euler angles from the rotation matrix

The Euler angles α, β, and γ describe the orientation with respect to the x-, the y-, and the z-axis, respectively, of the x-ray coordinate system. They are implicitly defined by a rotation matrix. The rotation matrix $\mathbf{R}$ which is calculated according to (A.2) is represented by Euler angles as follows:

$$\mathbf{R} = \begin{pmatrix} \cos\beta\cos\gamma & \sin\alpha\sin\beta\cos\gamma - \cos\alpha\sin\gamma & \cos\alpha\sin\beta\cos\gamma + \sin\alpha\sin\gamma \\ \cos\beta\sin\gamma & \sin\alpha\sin\beta\sin\gamma + \cos\alpha\cos\gamma & \cos\alpha\sin\beta\sin\gamma - \sin\alpha\cos\gamma \\ -\sin\beta & \sin\alpha\cos\beta & \cos\alpha\cos\beta \end{pmatrix}$$

For a general extraction of the angles α, β, and γ from such a matrix, two cases need to be distinguished. In the first singular one, the element R_{31} is 1 or -1. Then, β is $-\pi/2$ or $\pi/2$, respectively, and γ is assumed to be zero. The angle α can be obtained, e.g., using the conditions $\alpha = \arcsin(-R_{31}R_{12})$ and $\alpha = \arccos(-R_{31}R_{13})$.

In the normal case, two values for β are possible:

$$\beta_1 = -\arcsin(R_{31}) \qquad \beta_2 = \pi + \arcsin(R_{31})$$

Four possible values for α can be computed using the element R_{32}, β_1, and β_2:

$$\alpha_1 = \arcsin(\tfrac{R_{32}}{\cos\beta_1}) \qquad \alpha_2 = \pi - \arcsin(\tfrac{R_{32}}{\cos\beta_1})$$
$$\alpha_3 = \arcsin(\tfrac{R_{32}}{\cos\beta_2}) \qquad \alpha_4 = \pi - \arcsin(\tfrac{R_{32}}{\cos\beta_2})$$

For γ, also four values result inserting β_1 and β_2 in R_{21}:

$$\gamma_1 = \arcsin(\tfrac{R_{21}}{\cos\beta_1}) \qquad \gamma_2 = \pi - \arcsin(\tfrac{R_{21}}{\cos\beta_1})$$
$$\gamma_3 = \arcsin(\tfrac{R_{21}}{\cos\beta_2}) \qquad \gamma_4 = \pi - \arcsin(\tfrac{R_{21}}{\cos\beta_2})$$

From the resulting 8 possible Euler angle triplets, the ones which do not fulfill the conditions given by the other six matrix elements are excluded.

The remaining triplets are valid solutions. If two sets of Euler angles describe the same rotation, at least one of the angles differs of $> \pi/2$ between the sets. The valid solutions can hence be distinguished by means of the magnitudes of α, β, γ. As in this work the matrix $\mathbf{R}$ describes the relatively small rotation of the pelvis, the angles looked for certainly do not exceed $90°$. Thus, of the valid solutions the one with the smallest value of $|\alpha| + |\beta| + |\gamma|$ is taken.

Bibliography

[Berger and Gerig 1998] M. Berger and G. Gerig. Motion measurements in low-contrast imagery. In *Proc. of MICCAI*, pages 832–841, 1998.

[Berger 1999] M. Berger. *Deformable Area-based Template Matching with Application to low contrast imagery.* PhD thesis, Department of Electrical Engineering, ETH Zürich, 1999.

[Birch and Marshall 1979] R. Birch and M. Marshall. Catalogue of spectral data for diagnostic x-rays. Technical Report SRS 30, The Hospital Physicists' Association, 1979.

[Brand *et al.* 1986] R.A. Brand, D.R. Pedersen, and S.A. Yoder. How definition of "loosening"affects the incidence of loose total hip reconstructions. *Clin Orthop*, 210:185–191, 1986.

[Bruijn *et al.* 1995] J.D. Bruijn, J.L. Seelen, R.M. Feenstra, B.E. Hansen, and F.P. Bernoski. Failure of the mecring screw-ring acetabular component in toyal hip arthroplasty. *J Bone Joint Surgery*, 77-A(5):760–765, 1995.

[Busch 1989] H. Busch. Automatic modeling of rigid 3-d objects using an analysis by synthesis system. In *Proceedings of the SPIE Conference on Visual Communication and Image Processing IV*, volume 1199, 1989.

[Cianci *et al.* 1995] R. Cianci, F. Baruffaldi, F. Fabbri, S. Affatato, A. Toni, and A. Giunti. A computerized system for radiographical evaluation in total hip arthroplasty. *Computer Methods and Programs in Biomedicine*, 46:233–243, 1995.

[Collet *et al.* 1985] C. Collet, G. Grosdidier, H. Coudane, and J. Borrely. Anatomical basis for study of acetabular migration of prostethic cup used in arthroplasty of the hip: a new technique for measurement of migration. *Anat Clin*, 7:171–174, 1985.

[Danuser and Mazza 1996] G. Danuser and E. Mazza. Observing deformations of 20 nanometer with a low numerical aperture light microscope. In *Proceeding of the EOS Symposium on Lasers, Optics and Vision for Productivity in Manufacturing II*, volume 2782, 1996.

[DeLee and Charnley 1976] J.G. DeLee and J. Charnley. Radiological demarcation of cemented sockets in Total Hip Replacement. *Clin Orthop*, 121:20–32, 1976.

[Dickob *et al.* 1994] M. Dickob, J. Bleher, and W. Puhl. Standardisierte Pfannen-wanderungsanalyse in der Hüftendoprothetik mittels digitaler Bildverarbeitung. *Un-fallchirurg*, 97:92–97, 1994.

[Fanning 1999] D.W. Fanning. *IDL Programming Techniques*. Funning Software Consult-ing, 1999.

[Gill *et al.* 1981] P.E. Gill, W. Murray, and M.H. Wright. *Practical Optimization*. Aca-demic Press, London, 1981.

[Goodman *et al.* 1988] S.B. Goodman, S.J. Adler, D.P. Fyhrie, and D.J. Schurman. The acetabular teardrop and its relevance to acetabular migration. *Clin Orthop*, 236:199–204, 1988.

[Grün 1985] A Grün. Adaptive least squares correlation: A powerful image matching technique. *South African Journal of Photogrammetry, Remote Sensing & Cartography*, 14(3):175–187, 1985.

[Hardinge *et al.* 1991] K. Hardinge, M.L. Porter, P.R Jones, D.W.L. Hukins, and C.J. Taylor. Measurement of hip prostheses using image analysis. *J Bone Joint Surg (Br)*, 73-B(5):724–728, 1991.

[Hubbard 1969] M.J.S. Hubbard. The measurement of progression in protrusio acetabuli. *Am. J. Roentgenol.*, 106:506–508, 1969.

[Ilchmann *et al.* 1992a] T. Ilchmann, H. Franzen, B. Mjöberg, and H. Wingstrad. Mea-surement accuracy in acetabular cup migration. A comparison of four radiologic methods versus roentgen stereophogrammetric analysis. *J Arthoplasty*, 7:121–127, 1992.

[Ilchmann *et al.* 1992b] T. Ilchmann, M.A.R. Freeman, and B. Mjöberg. Accuracy of the Nunn method in measuring acetabular cup migration. *Upsala J Med Sci*, 97:67–68, 1992.

[Ilchmann *et al.* 1997] T. Ilchmann, U. Kesteris, and H. Wingstrand. Effect of pelvic tilt on migration and wear measurements after total hip arthroplasty. 4th paper in the thesis: Radiographic assessment of cup migration and wear after hip replacement, Ilchmann, T., Department of Orthopedics, Lund University Hospital, Sweden and BG Trauma Center University of Tübingen, Germany, 1997.

[Johnston *et al.* 1990] R.C. Johnston, R.H. Fitzgerald, W.H. Harris, R. Poss, M.E. Müller, and C.B. Sledge. Clinical and radiographic evaluation of total hip replacement. *J Bone Joint Surg Am*, 72(2):161–168, 1990.

[Jones *et al.* 1989] P.R. Jones, C.J. Taylor, Hukins D.W.L., M.L. Porter, and K. Hardinge. Prosthetic hip failure: retrospective radiograph image analysis of the acetabular cup. *J Biomed Eng*, 11(5):253–257, 1989.

[Kärrholm *et al.* 1997] J. Kärrholm, P. Herberts, P. Hultmark, H. Malchau, B. Nivbrant, and J. Thanner. Radiostereometry of Hip Prostheses: Review of Methodology and Clinical Results. *Clin Orthop*, November(344):94–110, 1997.

[Koch 1988] K.R. Koch. *Parameter Estimation and Hypothesis Testing in Linear Models*. Springer-Verlag, 1988.

[Koch 1990] R. Koch. Automatic modelling of natural scenes for generating synthetic movies. In *Proceedings of the European Computer Graphics Conference Eurograph*, 1990.

[Koch 1993] R. Koch. Dynamic 3-D Scene Analysis through Synthesis Feedback Control. *IEEE Transactions on Pattern Analysis and Machine Intelligence*, 15(6), 1993.

[Kölbel and Golzo 1977] R. Kölbel and H. Golzo. Die Köhlersche Tränenfigur: Untersuchungen zur Beziehung von Röntgenbild und anatomischen Substrat. *Fortschr Röntgenstr*, 127(4):326–333, 1977.

[Krismer *et al.* 1995] M. Krismer, R. Bauer, J. Tschupik, and P. Mayrhofer. EBRA: a method to measure migration of acetabular components. *J Biomechanics*, 28:1225–1236, 1995.

[Krismer *et al.* 1996a] M. Krismer, B. Stöckl, M. Fischer, R. Bauer, and P. Mayrhofer. The prediction of late aseptic failure of hips sockets by early migration. In *Proc. 2nd EBRA Meeting, Insbruck, Austria*, september 1996.

[Krismer *et al.* 1996b] M. Krismer, B. Stöckl, M. Fischer, R. Bauer, P. Mayrhofer, and M. Ogon. Early migration predicts late aseptic failure of hip sockets. *J Bone Joint Surg*, 78-B426, 1996.

[LaRose *et al.* 2000] D. LaRose, L. Cassenti, B. Jamaraz, J. Moody, T. Kanade, and A. DiGioia. Post-operative measurement of acetabular cup position using x-ray/ct registration. In *Medical Image Computing and Computer-Assisted Intervention*, 2000.

[Longuet-Higgins 1981] H.C. Longuet-Higgins. A computer algorithm for reconstructing a scene from two projections. *Nature*, 293, september 1981.

[Lötjönen *et al.* 1999] J. Lötjönen, I.E. Magnin, L. Reinhardt, J. Nenonen, and T. Katila. Automatic reconstruction of 3d geometry using projections and a geometric prior model. In *Medical Image Computing and Computer-Assisted Intervention*, 1999.

[Malchau *et al.* 1995] H. Malchau, J. Kärrholm, Y.X. Wang, and P. Herberts. Accuracy of migration analysis in hip arthroplasty. *Acta Orthop Scand*, 66(5):418–424, 1995.

[Manaster 1996] B.J. Manaster. Total hip arthroplasty: radiographic evaluation. *Radiographics*, 16:645–660, 1996.

[Massin *et al.* 1989] P. Massin, L. Schmidt, and C.A. Engh. Evaluation of cementless acetabular component migration. an experimental study. *J Arthroplasty*, 4(3):245–251, 1989.

[Mikhail 1976] E.M. Mikhail. *Observations and Least Squares*. Harper & Row, 1976.

[Mjöberg *et al.* 1985] B. Mjöberg, J. Brismar, L.I. Hansson, H. Petterson, G. Selvik, and R. Önnerfält. Definition of endoprosthetic loosening: Comparison of arthrography, scintigraphy and roentgen stereophotogrammetry in prosthetic hips. *Acta Orthop Scand*, 56:469–473, 1985.

[Mjöberg *et al.* 1986] B. Mjöberg, G. Selvik, L.I. Hansson, R. Rosenqvist, and R. Önnerfält. Mechanical loosening of total hip prostheses: A radiographic and roentgen stereophotogrammetric study. *J Bone Joint Surg*, 68-B:646–652, 1986.

[National Institute of Standards and Technology 1997] National Institute of Standards and Technology. *XCOM: Photon Cross Sections Database*. http://physics.nist.gov/PhysRefData/Xcom/Text/XCOM.html, 1997.

[National Library of Medicine 2001] National Library of Medicine. *The Visible Woman Project*. http://www.nlm.nih.gov/research/visible/visible_human.html, 2001.

[Nilsson and Kärrholm 1996] K.G. Nilsson and J. Kärrholm. RSA in the assessment of aseptic loosening. *J Bone Joint Surg [Br]*, 78-B(1):1–2, 1996.

[Numerical Algorithms Group 2000] Numerical Algorithms Group. *Numerical Libraries: C Library*. http://www.nag.co.uk:80/numeric/CL/CLdescription.asp, 2000.

[Nunn *et al.* 1989] D. Nunn, M.A.R. Freeman, P.F. Hill, and S.J.W. Evans. The measurement of migration of the acetabular component of hip prosthesis. *J Bone Joint Surg [Br]*, 71:629–631, 1989.

[Peic 1971] Stj. Peic. Die Köhlersche Tränenfigur und ihre Bedeutung in der Röntgendiagnostik. *Fortschr Röntgenstr*, 114(3):305–316, 1971.

[Redhead *et al.* 1997] A.L. Redhead, A.C.W. Kotcheff, C.J. Taylor, M.L. Porter, and D.W.L. Hukins. An automated method for assessing routine radiographs of patients with total hip replacement. *Journal of Engineering in Medicine, Proceedings of the Institution of Mechanical Engineers Part H*, 211(H2), 1997.

[Redhead 1997] A. L. Redhead. *Computerized Image Analysis of Total Hip Replacement Radiographs*. PhD thesis, Department of Medical Biophysics, University of Manchester, 1997.

[Russe 1988] W. Russe. *Röntgenphotogrammetrie der künstlichen Hüftgelenkspfanne*. Huber, Bern, 1988.

[Sanchez del Rio and Dejus 2000] M. Sanchez del Rio and R.J. Dejus. *X-ray Oriented Programs.* http://www.esrf.fr/computing/scientific/xop/, 2000.

[Selvik 1974] G. Selvik. *A roentgen stereophotogrammetric method for the study of the kinematics of the skeletal system.* PhD thesis, University of Lund, 1974.

[Selvik 1990] G. Selvik. Roentgen Stereophotogrammetric Analysis. *Acta Radiologica,* 31:113–126, 1990.

[Snorrason and Kärrholm 1990] F. Snorrason and J. Kärrholm. Primary migration of fully-threaded acetabular prostheses. *J Bone Joint Surg,* 72-B(4):647–652, 1990.

[Stöckl et al. 1999] B. Stöckl, M. Sandow, M. Krismer, R. Biedermann, C. Wimmer, and B. Frischhut. Migration of the duraloc cup at two years. *J Bone Joint Surg,* 81-B(1):51–53, 1999.

[Sutherland and Bresina 1992] C.J. Sutherland and S.J. Bresina. Measurement of acetabular component migration using two-dimensional radiography. *J Arthroplasty,* 7(Suppl):377–379, 1992.

[Sutherland et al. 1982] C.J. Sutherland, A.H. Wilde, L.S. Borden, and K.E. Marks. A Ten-Year Follow-up of One Hundred Consecutive Müller Curved-Stem Total Hip-Replacement Arthroplasties. *J Bone Joint Surg,* 64-A(7):970–982, 1982.

[Székely et al. 1998] G. Székely, M. Bajka, J. Hug, M. Manestar, P. Groscurth, and U. Haller. Anatomical model generation for laparoscopic surgery simulation. In *Second Visible Human Project Conference,* pages 45–46, 1998.

[The MathWorks, Inc. 1992] The MathWorks, Inc. *MATLAB User's Guide.* 1992.

[Watt and Watt 1992] A. Watt and M. Watt. *Advanced Animation and Rendering Techniques; Theory and Practice.* ACM Press, New York, New York, 1992.

[Wetherell et al. 1989] R.G. Wetherell, A.A. Amis, and F.W. Heatley. Measurement of acetabular erosion. the effect of pelvic rotation on common landmarks. *J Bone Joint Surg,* 71B(3):447–451, 1989.

[Wolfram 1996] Stephen Wolfram. *The Mathematica book.* Cambridge University Press, Reading, Massachusetts, 1996.

Curriculum Vitae

Kathrin Burckhardt

Communications Technology Laboratory
Computer Vision Group
ETH-Zentrum
Gloriastr. 35
CH-8092 Zürich, Switzerland

Tel.: +41-1-6326670
Fax: +41-1-6321199
e–mail: tribur@vision.ee.ethz.ch

private:

Aemtlerstr. 78
CH-8003 Zürich, Switzerland

Tel.: +41-1-4625350

Personal Data

Date of Birth:	August 13, 1969
Place of Birth:	Munich, Germany
Nationality:	German
Marital State:	Single

Education

Oct 1995	Diploma in Physics at the Ludwig-Maximilians-Universität (LMU), Munich
Aug 1994–Aug 1995	Diploma thesis at the Physiological Institute of the LMU on "Volume Determination of Cells in Amphibian Skin by means of Morphometry"
1992–1995	Studies of physics at the LMU
1991–1992	Studies of physics at the Freie Universität Berlin
1988–1991	Studies of physics at the LMU
June 1988	"Abitur" at the Augustinus Gymnasium in Weiden